Doctoral Dissertation
Doctoral Program in Material Science and Technology (XXX Cycle)

Bio-oriented Micro- and Nano-Structures Based on stimuli-responsive polymers

By

Federica Pirani

******

Supervisors:
Prof. Emiliano Descrovi
Prof. Candido Fabrizio Pirri

Doctoral Examination Committee:
Dr. Thierry Grosjean, FEMTO-ST Institute / University of Franche-Comte
Dr. Maurizio Ventre, Università di Napoli Federico II

Politecnico di Torino
2018

Declaration

I hereby declare that, the contents and organization of this dissertation constitute my own original work and does not compromise in any way the rights of third parties, including those relating to the security of personal data.

Federica Pirani

2018

* This dissertation is presented in partial fulfillment of the requirements for **Ph.D. degree** in the Graduate School of Politecnico di Torino (ScuDo).

To my lovely parents, Giorgio & Franca,

To my sweet sister Barbara,

To my half.

Abstract

Nowadays, the ability to pattern surfaces on the micro- and nano- scale is the basis for a wide range of research fields. Over last few decades, a certain number of processing technologies offer the possibility to fabricate complex 2D and 3D polymeric designs which are mostly static in nature since they cannot be physically modified once fabricated. The aim of the present thesis is to overcome such a limitation, exploiting stimuli-responsive materials (Chapter I). We allow to engineer polymeric architectures adding interesting functionalities, by providing an active manipulation of pre-structured systems, which could be helpfully in a wide variety of applications, such as biosensing and cell conditioning.

In the first part of the present dissertation (Chapter II), a thermos-sensitive material is employed. We investigate the thermo-responsive behavior of Poly(N-isopropylacrylamide) (pNIPAAm)-based crosslinkable hydrogel as active binding matrix in optical biosensors. In this study, we propose an extension of surface plasmon resonance (SPR) and optical waveguide mode (OWS) spectroscopy, for *in situ* observation of nano-patterned hydrogel film that are allowed to swell and collapse by varying the external temperature of the aqueous environment. Weak refractive index contrast of hydrogel structures arranged in periodic pattern, is generally associated with intrinsically low diffraction efficiency. In order to enhance the intensity of diffracted light, the surface is probed by resonantly excited optical waveguide modes, taking advantage of the fact that the hydrogel can serve as optical waveguide (HOW) enabling the excitation of additional modes besides surface plasmons. Thus, we provide a hydrogel optical waveguide-enhanced diffraction measurements, taking advantage of strong electromagnetic field intensity enhancements that amplifies the weak diffracted light intensity.

The main part of the thesis is focused in the study of azopolymer-containing materials, a specific class of light-responsive materials. Upon photon absorption, azobenzene undergo reversible *trans-cis* photoisomerization, which induces a substantial geometrical change of its molecular structure, that can be translated into

larger-scale movements of the material below the glass transition temperature (Tg) of the polymer.

In Chapter III, by exploiting the light-induced mass migration phenomenon, we demonstrate that an azopolymeric film patterned by soft imprinting technique, can be anisotropically deformed and consequent restored in its initial shape via single irradiation just by controlling the polarization state of the incident laser beam. We also propose that the light-driven morphological manipulation can induce anisotropic wettability changes. Lastly, a polarization driven birefringence effect on flat and structured surfaces is discussed.

Chapter IV focuses in the design of novel azopolymeric systems, where the optical response is provided by azobenzene molecules, which doped two different host materials. The photo-responsive behavior and potential applications of azo compounds incorporated into either a soft elastomeric and in rigid matrix is discussed. Azo-embedded poly(dimethylsiloxane) (PDMS) is studied as tunable optical lens and an azo-doped photocurable commercial polymeric resin is developed to study the photo-mechanical transduction of a 3D suspended membrane fabricated by two photon lithography technique.

In Chapter V, we propose a light-deformable azopolymeric micro-pillars patterned substrate as a biocompatible and "smart" platform for dynamic material-cell observation in 2D environment, modified by a holographic optical conditioning. The aim is to observe by time-lapse acquisitions, how an *in situ* deformation of a pre-patterned structure can influence cell functions and fate.

Finally, in Chapter VI, general remarks of the present work are discussed, and directions for future perspective are summarized.

List of Publications

I. F. Pirani, N. Sharma, A. Moreno-Cencerrado, S. Fossati, C. Petri, E. Descrovi, J.L. Toca-Herrera, U. Jonas, J. Dostalek. 'Optical Waveguide-Enhanced Diffraction for Observation of Responsive Hydrogel Nanostructures', Macromol. Chem. Phys. 218, 1600400. (2017).

II. F. Pirani, A. Angelini, F. Frascella, R. Rizzo, S. Ricciardi, E. Descrovi. 'Light-Driven Reversible Shaping of Individual Azopolymeric Micro-Pillars, Sci. Rep. 6, 31702 (2016).

III. F. Pirani, A. Angelini, S. Ricciardi, F. Frascella, E. Descrovi, 'Laser-induced anisotropic wettability on azopolymeric micro-structures', App. Phys. Lett. 110, 101603 (2017).

IV. A. Angelini, F. Pirani, F. Frascella, S. Ricciardi, E. Descrovi,' Light-driven liquid microlenses', Proc. SPIE 10106, Integrated Optics: Devices, Materials, and Technologies XXI, 1010612, doi:10.1117/12.2250988 (2017).

V. M. Miola, S. Ferraris, F. Pirani et al. 'Reductant-free synthesis of magnetoplasmonic iron oxide-gold nanoparticles, Ceramics International 43(17), doi: 10.1016/j.ceramint.2017.08.063 (2017).

VI. F. Pirani, A. Angelini, F. Frascella, and E. Descrovi, 'Reversible shaping of micro-wells by polarized light irradiation'. International Journal of Polymer Science, International Journal of Polymer Science, Article ID 6812619, doi:10.1155/2017/68126192017 (2017).

VII. A. Angelini, F. Pirani, F. Frascella, E. Descrovi, "Reconfigurable elastomeric graded-index optical elements controlled by light", Light: Science and Applications 7, DOI: 10.1038/s41377-018-0005-1, (2018).

Conference Talks

I. F. Pirani, A. Angelini, F. Frascella, R. Rizzo, S. Ricciardi, E. Descrovi. 'Light-driven reversible shaping of 2D polymeric lattices', Conference on Lasers and Electro-Optics, CLEO 2016.

II. F. Pirani, A. Angelini, S. Ricciardi, F. Frascella, R. Rizzo, F. Ferrarese Lupi, N. De Leo, L. Boarino, E. Descrovi, 'Tunable hydrophobicity assisted by light-responsive surface micro-structures', Proc. SPIE 10092, Laser-based Micro- and Nanoprocessing XI, 100920A, doi: 10.1117/12.2251008 (2017).

Author's Contribution

The author has played a relevant role in all aspects of the research work summarized in this thesis, mainly regarding the study of the materials. However, due to the complexity of the thesis project, during her PhD the author has worked within a multidisciplinary team and she collaborated with different local and international research groups. In dealing with thermo-responsive hydrogel structures (@AIT, Vienna), the author has prepared, characterized the samples and performed the optical measurements dr. N. Sharma has built the experimental setups, A. M. Cencerrado has performed the Atomic Force Microscopy analysis and S. Fossati worked on the simulations.

In dealing with azo-doped acrylic suspended 3D membranes, (@ KAUST, Thuwal), the two photon polymerization process has been developed in cooperation with dr. V. P. Rajamanickam and S. Licheri. The interferometric setup used for light-induced phase measurements has been developed by dr. A. Angelini.

The development of light-responsive platform has been performed in collaboration with the Candiolo Cancer Center (IRCCS). In particular, cell seeding and culturing has been performed by dr. S. Ricciardi and dr. A. Puliafito. The author has worked in the preparation of the samples and performed the optical conditioning experiments. The implementation of the program developed in the LabVIEW software has been carried out in collaboration with V. Chermokova. Cell tracking has been performed by dr. A. Puliafito.

Contents

List of Figures

1

Introduction

1.1 Background and Motivation

Materials science is required to construct a basis for modern, sustainable technology, and using functional materials from micro- to nano- scale is a noteworthy tool in achieving sustainable, efficient and elegant solutions to meet the constantly growing demand. The awareness that there are small things in the world, which are not visible to the naked eye, spreads the development of the natural sciences towards the micro-world, in order to enable a better understanding of the world and the processes therein. Therefore, the development of new materials and the ability to pattern surfaces on a micro- and nano- length scale represent certain milestones in the modern research fields [1].

Patterning is of paramount importance in many areas of modern science and technology, with applications ranging from the production of integrated circuits, information storage devices, miniaturized sensors, microfluidics devices, display units to the fabrication of microelectromechanical systems (MEMS), photonics crystals, micro-optical components, even in biomedicine and biological fields. The nanotechnology literature differentiates between two basic approaches of fabrication, *Top-down* and *Bottom-up* [2]. The *Top-down* approach is a subtractive process in which material is removed to produce features of a controlled shape and size. This approach is based on a lithographic philosophy, which is in contrast to the other approach, where atomic or molecular units are used to assemble molecular structures, ranging from atomic dimensions up to supramolecular structures in the nanometer range. This *Bottom-up* approach is mainly influenced by chemical principles. The challenge of modern nanotechnology is the realization of syntheses by the *Top-down* and *Bottom-up* approaches. This task is not driven entirely by the

absolute structure dimensions, because today macro- and supramolecules extending up to hundreds of nanometers or even micrometers can already be synthesized or isolated from biological systems. So the overlap of both approaches is not a problem. Both techniques provide specific capabilities that can be implemented by the other. The lithographic techniques (*Top-down*) offer the connection between structure and technical environment. In front of that, lithography is one of the most common process of patterning, which involves a flow of information that typical begins with the design of a pattern in the form of a dataset and ends at a patterned array of features on the surface of a substrate. In general, lithography technique is most suitable for generating one-dimensional (1D) or 2D patterns. These techniques are added to the unconventional nanofabrication areas of scanning probe lithography (SPL) [3], edge lithography [4], molding [5], embossing [6], and self-assembly [7]. Conventional techniques for nanofabrication are commercially available and widely implemented in manufacturing. They are expensive and largely restricted to planar fabrication in semiconductor materials. Such techniques expose substrates to corrosive etchants, high-energy radiation, and relatively high temperatures. To fabricate 3D architectures, one has to rely in layer-by-layer approach but an emerging alternative which provides attractive and versatile for generating 3D structures is laser-assisted fabrication using photocurable resins [1]. In these techniques, the fabrication of the structure occurs by the photopolymerization of the resist in the vicinity of the laser beam, generating a voxel, which is a 3D volume element of solidified resist. Typically, the patterning procedure is performed by point-by-point scanning a focused laser according to a pre-programmed pattern design in the form of a voxel matrix.

Nowadays, the most part of patterning techniques provides structures which are static and passive, they cannot be modified once fabricated. The growing need of having tunable structures, modifiable after their fabrication, has fostered the studying and designing of novel materials that have one or more properties that can be significantly changed in a controlled fashion by an externally applied field value such as stress, temperature, light, pH and electric or magnetic fields [8].

Micro and nanotechnologies essentially rely on the development of static tiny devices whose intrinsic properties are fixed by their fabrication processes. Modifying these properties dynamically after device fabrication remains an extraordinary challenge, and represents nowadays high scientific and economic perspectives. The development of deformable materials under external control represents an appealing opportunity. Although it represents an important new

degree of freedom in the manipulation by means of external stimuli, it stretches the actual limits of material science, and thus remains extraordinarily challenging. The present thesis contributes to this subject.

Therefore, with the recent development of material science, many new, high-quality and cost-efficient materials have come into use in various field of engineering. In the last ten decades, the materials became multifunctional and required the optimization of different characterization and properties. With the last evolution, the concept has been driving towards composite materials and recently, the next evolutionary step is being contemplated with the concept of “smart” materials. Smart materials are new generation materials surpassing the conventional structural and functional materials [9]. These materials possess adaptive capabilities to external stimuli, such as loads or environment, with inherent intelligence. Smart materials are defined as materials, which possess the ability to change their physical properties in a specific manner in response to specific stimulus input [10]. The associated changeable chemical and physical properties could be shape, stiffness, viscosity, damping and surface wettability. Takagi (1990) explained it as intelligent materials that respond to environmental changes at the most optimum conditions and reveal their own functions according to the environment [11]. Many important new applications for stimuli-responsive polymers lie in the field of nano- and micro-fabrication, where stimuli-responsive polymers are being established as important manipulation tools. Some techniques have been developed to selectively position organic molecules and then to obtain well-defined patterned substrates at the micrometer or submicrometer scale. There are several methods for patterning of stimuli-responsive polymers, including photolithography, electron beam lithography, scanning probe writing, and printing techniques (microcontact printing, ink-jet printing). These characteristics provide numerous possible applications for these materials and structures in our day to day life, including aerospace, manufacturing, civil infrastructure systems, electronics, biomechanics and environment [12]. By changing their properties, smart materials can be used in sensing (optical sensors, biosensors, chemical sensors) and actuation applications, to detect faults and cracks and therefore useful as a diagnostic tool, and even in biomedicine and tissue engineering.

So, "smart" polymers or stimuli-responsive polymer materials are polymers, that are able to reversibly respond to small changes in their physical and/or chemical environment (stimuli) through a large property change (response). Usually, they are classified according to the external stimuli to which they respond, such as temperature, pH, light, ultrasound, magnetic field, and ionic strength [8].

The present dissertation explores a connected set of topics related to the investigation of smart materials. In this dissertation we focused in the processing and patterning of thermo-responsive and light-responsive polymers [13], their integration in highly innovative ultra-compact architectures, the monitoring of their reconfigurable properties in real-time, and the achievement of new functionalities out of their tunable morphological and optical responses.

1.2 Temperature-responsive polymers

Temperature-responsive polymers are one of the most exploited class among stimulus responsive polymers. This is mainly because of their high applicability in a broad range of applications, such as in nanotechnology [8], catalysis [14], surface modifications, chemistry [15], and biomedical field [16]. Thermo-responsive materials exhibit a thermally induced, reversible phase separation at a characteristic temperature known as the critical solution temperature (CST). They are soluble in a solvent at low temperatures but become insoluble as the temperature rises above the critical solution temperature (CST). [17] Among these materials, there are two main types of polymers which exhibit opposite behavior, as described in the phase diagrams depicted in Figure 1.1. The first possess an upper critical solution temperature (UCST) meanings a uniform solution above it (isotropic state) and a phase separation (anisotropic state) below this threshold point, constituted by the solvent and the precipitated polymer. The second presents a monophase below the critical point and two distinct phases above a temperature defined as the low critical solution temperature (LCST). This means that below the LCST and above UCST, a single phase exists for all compositions. Thus, for example, a polymer solution below the LCST is a clear, homogeneous solution while a polymer solution above the LCST appears cloudy (leading to LCST also being referred to as cloud point) [18]. This swelled-to-coiled transition, and vice versa, is regulated by an enthalpy-entropy equilibrium. Below the CST the hydrogen bonding term, related to enthalpy, dominates with solvated polymer chains thanks to water molecule hydration. This phenomenon occurs because it is energetically more favorable. [16]

In particular, considering the free energy of the system using the Gibbs equation:

$$\Delta G = \Delta H - T\Delta S$$

(G: Gibbs free energy, H: enthalpy and S: entropy)

when the temperature increases above the threshold point, hydrogen bonding ends to be stable and water becomes a bad solvent for the polymer. Accordingly, the hydrophobic interactions, due to the entropy of the system, are the responsible for polymer coiling and phase separation [19].

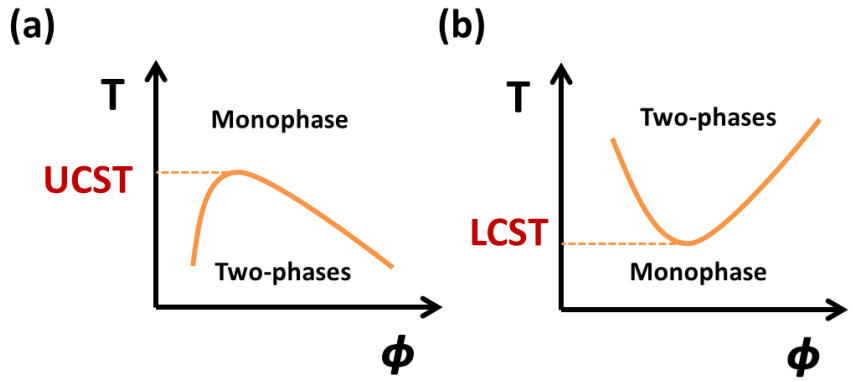

Figure 1.1: Schematic illustration of phase diagrams for a polymer in solution, where the temeperature (T) is plotted against the polymer volume fraction (Φ). (a) upper critical solution (UCST), (b) lower critical solution temperature (LCST) behavior.

The LCST transition in water, driven by entropy, is dependent on the hydrophilic-hydrophobic balance of the polymer end-groups, chain length, pH and salt concentration. For instance, longer polymer chains lead a lower transition temperature because of the increased amount of polymer-polymer interactions [20]. One of the first reported and most studied thermo-responsive polymer in aqueous solution which exhibits LCST behavior, is poly(N-isopropylacrylamide) (pNIPAAm) [21]. pNIPAAm has a LCST of around 32°C, a very useful temperature for biomedical applications since it is close to the body temperature [22]. It consists of hydrophilic parts, that undergo hydrogen bonding with the bulk water to keep the polymer soluble, and hydrophobic side chains that are mostly shielded from the surrounding water. Modifications of the polymer such as copolymerization or post polymerization modifications can be used to tune the transition temperature by adjusting the hydrophilic/hydrophobic balance of the polymer [23]. Due to the fact that this polymer has been the base of the first experimental part of this work, a separate subsection (Chapter 2.2) will be dedicated to it in the next pages. Other well-known LCST polymers including poly(N,N-diethylacrylamide) (PDEAAm) [24] with an LCST over the range of 25 to 32 °C, poly(N-vinlycaprolactam) (PVCL) [25], with an LCST between 25 and 35 °C

poly[2-(dimethylamino)ethyl methacrylate] (PDMAEMA) with an LCST of around 50 °C [26], poly(2-oxazoline)s (POx) [27], and poly(oligo(ethyleneglycol)methylether methacrylate)s (POEGMAs) [28], have also been widely studied and have found various applications as "smart" materials. Polymer solutions that exhibit UCST behavior are driven by strong enthalpic inter chain interactions. Examples include polybetaines [29], poly(methacrylamide) (PMAm) [30], poly(allylurea) (PU) [31], poly(2-dimethyl(methacryloxyethyl)ammoniumpropane sulfonate) (PDMAPS-MA) [32], and poly(N-acryloylglycinamide) (PNAGA) [33].

A third class of thermoresponsive polymer solutions exhibit both LCST and UCST behavior. This comprises partially protonated PDMAEMA + K3[Co(CN)6] [34], poly(ethylene oxide) (PEO) [35], poly(vinylmethylether) (PVME) [36] and poly(2-hydroxyethylmethacrylate) (PHEMA) [37].

1.3 Light-responsive polymers

Light-sensitive materials are the second type of stimuli-responsive materials investigated. The use of light as a trigger is particularly attractive since its characteristics can be remotely and accurately controlled, quickly switched and easily focused into specific area [38] .

In these materials the photosensitive element is a photochromic molecule which undergo on a reversible transformation between two isomeric forms induced by the absorption of light at appropriate wavelength, resulting in a change in absorption spectra. The mechanisms include pericyclic reactions, *cis–trans* isomerizations, dissociation processes, intramolecular hydrogen transfers or group transfers, and electron transfers (oxidation– reduction). In addition to a color change, these transformations are accompanied by changes in the physical and chemical properties of the species involved, such as alterations to in the dipole moment, refractive index and geometrical structure [39]. Importantly, these dynamic transformations can generate changes in the optical, chemical, electrical and bulk properties of the system that incorporates them. Photochromic molecules therefore play a crucial role within photo-responsive polymeric systems, being able to capture an optical signal and then convert this, via their isomerization, to a useful property change. According to the subdivision of Kinoshita [40], typical photo-reactive guests in polymers are azobenzene, triphenylmethane and spiropyran groups, which have been entrapped, cross-linked, and introduced as a side chain or part of the main

chain in polymer matrices. The typical behaviors depicted in Figure 1.2, can be described briefly as follows: ultraviolet (UV) and visible irradiation of an azobenzene stimulates the reversible conversion of the planar *trans* isomer to the bent *cis* isomeric form via the isomerization of a –N=N– bond; UV irradiation of a spiropyran or spirooxazine initiates an electrocyclic ring opening reaction of a spiro form which results in the formation of an open, planar merocyanine form with an extended conjugated system able to absorb strongly in the visible region; for diarylethenes and fulgides, UV irradiation results in the closing of the six-membered ring within its core which results in the formation of thermally irreversible colored isomers. The photochromic inter-conversion between isomeric forms is often referred to as switching [9].

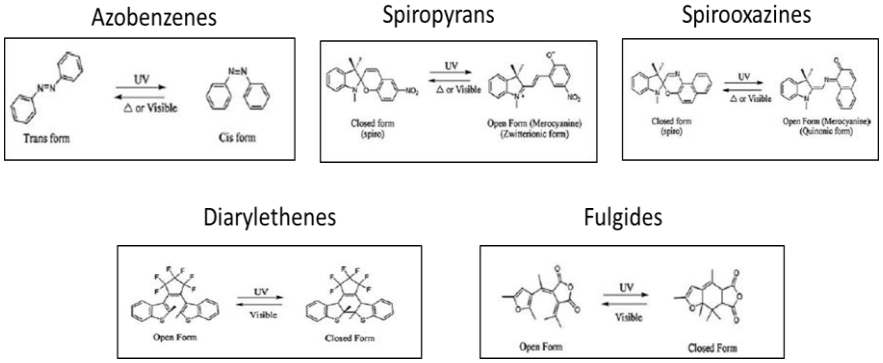

Figure 1.2: Families of photochromic compounds commonly used in polymeric systems.

Herein, we concentrate on azobenzene containing polymers (azopolymers), representing a materials platform that combines the ease processing and high quality of polymers with the photocontrol provided by azobenzene units [41]. The main part of the present dissertation is focused around this class of potential responsive materials.

2

Thermosensitive hydrogel binding matrix - based biosensor

Polymers are attractive candidates for smart materials because they may contain different domains or moieties. The affinity of these domains towards environment is altered under different conditions. This results in conformational change, e.g. from globule-to-coil or helix-to-random coil, which is associated with phase transition, as describe in details before. However, many potential applications of smart materials are in aqueous medium. Polymers can form extended three dimensional crosslinked structures known as hydrogel. In this work we present in detail an all-optical monitoring system in order to study in real-time the morphological evolution of a thin layer of hydrogel with temperature in a water environment. We show the importance and efficiency of crosslinkable hydrogel nanostructures as active binding matrix in optical biosensor applications. Surface-attached hydrogel films allow a direct detection of target analytes without the need of additional labels, but just relying on the measurement of molecular binding-induced refractive index changes by surface plasmon resonance (SPR) and optical waveguide (OW) spectroscopy.

A hydrogel consists of a polymer matrix containing a large amount of water, even reaching values of 99% by weight [42]. The polymer matrix is composed of a very large number of long molecular chains, also called backbones, which are made up small molecular units called monomers and comonomers. The molecular chains are held together by interconnections between these chains, called crosslinkers. The crossliknker is defined as the molecular entity at which three or more chains can join to form crosslink point and turn the polymer into a network [43]. Figure 2.1 provides a visual representation of a hydrogel matrix.

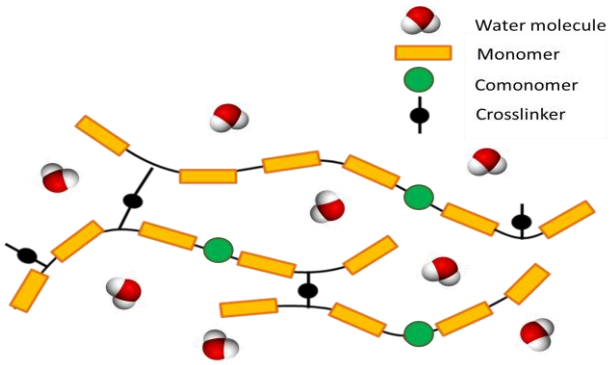

Figure 2.1: Sketch of the components of a hydrogel matrix in an aqueous medium.

Two different methods can be employed to create the crosslinking. In the "*in situ crosslinking"* method the crosslink is created during the synthesis of the polymer chains by introducing the crosslinker molecules [44]. Alternatively, in "*post-synthetic crosslinking*", the crosslink points may be generated in a second step after formation of the polymer chains [45].

A common group of monomer, used in the synthesis of temperature-sensitive hydrogels, are N-alkyl acrylamides. The well-known monomer from this group is N-isopropylacrylamide (NIPAAm), which has sidechains inclined to interact with water by hydrogen bonds. This causes a hydrogel made from this monomer, called a poly-NIPAAm hydrogel, to attract water molecules and swell at room temperature. The backbones of the polymer, the long chains of C–C bonds to which the sidechains are attached, are hydrophobic and prone to reduce their surface area exposed to the highly polar water molecules. Normally when the hydrogen bonds between the sidegroups and the water are present, the aggregation of the backbones is prevented because the hydrogen bond interactions with the water molecules are stronger than the backbone interactions. When the hydrogen bonds are broken, due to increasing thermal agitation, the aggregation process takes place. This results in the shrinkage of the thermosensitive hydrogel with increasing temperature [46].

pNIPAAm hydrogel, as described in the Introduction, exhibits a lower critical solution temperature (LCST) of 32°C. Below this temperature, pNIPAAm shows a highly open, water-swollen structure, while above the LCST it collapses with a release of water, which leads to an increase in its density and variation of the refractive index [47].

Hydrogel materials exhibits a great number of specific properties highly attractive for a variety of applications including tissue engineering [48], drug release [49], actuator [50] and sensing [51]. These properties embrace the aqueous swelling medium as the basis of biocompatibility, non-fouling behavior, and being not cell toxic, while providing high optical quality and transparency. In this perspective, hydrogel are mainly employed in optical biosensors applications [51].

So, a stable attachment of hydrogel layer onto a solid substrate is a crucial aspect in a sensor fabrication. To this aim, two fundamental strategies can be adopted: (a) deposition of the polymer layer followed by subsequent crosslinking; or (b) crosslinking during deposition or growth of the polymer network. In this work we adopted the first method, in which the classical technique of spin coating [52] is used to deposit a precursor polymer onto the solid substrates from solution, followed by crosslinking and surface attachment.

Another relevant characteristic of surface-attached hydrogel films is the swelling of the dry layer upon contact with water to an equilibrium film thickness. The swelling ratio corresponds to the relative change of the film thickness, and the time evolution of the swelling process. It is closely related to the hydrophilicity of the polymer and the crosslinking density. For instance, a higher crosslink density leads to a lower swelling ratio [53]. The crosslinking density can be varied by modifying the ratio of crosslinking units to polymer backbone units during polymer- and network formation or by the extent of the crosslinking reaction performed after the film formation. The state of the polymer when the crosslinks are introduced is another important aspect of the crosslinking process. The difference between dry crosslinking (in photocrosslinking of a neat polymer film) and wet crosslinking (in crosslinking polymerization in water) becomes evident when the polymer layer is attached to a substrate surface. The latter case of crosslinking under equilibrium conditions does not lead to strain when the swollen network is anchored to the substrate, while the situation is different for the dry polymer being crosslinked and surface-attached before swelling. The anchoring restricts movement and swelling at the hydrogel-substrate interface, allowing a network expansion in a highly anisotropic one direction, away from the surface [45][54]. A consequence of this surface confinement in hydrogel layers is a reduced swelling compared to the unrestricted 3D hydrogel by a factor of around 5 to 10 [55]. The swelling kinetics is a further characteristic property of hydrogel films that strongly depends on structural parameters, such as chemical composition of the polymer backbone and morphological structure of the hydrogel material.

A number of method such as ellipsometry [56], surface plasmon resonance (SPR) [57], optical waveguide mode spectroscopy (OWS) [58], atomic force microscopy (AFM) [59], spectroscopy of leaky dielectric waveguides [60] and integrated optical Mach-Zehnder interferometer [61] are employed for observation of hydrogel film and to measure the thickness of hydrogel film and the variations in refractive index. These methods allow the determination of the swelling ratio between the swollen and the dry or collapsed film thickness, and often also provide information about the swelling kinetics.

The present chapter is focused in the study of a pNIPAAm-based crosslinkable hydrogel nanostructure employed as active binding matrix in optical biosensors based on optical waveguide-enhanced diffraction measurements. This approach is an extension of surface plasmon resonance (SPR) and hydrogel optical waveguide (HOW) mode spectroscopy for *in situ* observation of tethered thin hydrogel film that are allowed to swell and collapse in the direction perpendicular to the surface. The main experimental findings of the present study have been previously published in Macromolecular Chemistry and Physics. 218, 1600400. (2017), ***Publication I***.

2.1 Hydrogel Patterning

The ability to pattern surfaces on the micro- and nanoscale is the basis for a wide range of research and applications spanning microelectronics, photonic structures, microfluidics, surface science and sensing. Over last few decade lithography has been one of the main methods to pattern the hydrogel. It's a cost-effective, high-throughput technique that is suitable for large-area surface patterning with good alignment, controlled topography and a broad range of features. The resolution of patterns varies from micrometers to sub-100 nanometers [62].

Biosensors based on structured 'smart' hydrogel have attracted considerable attention in the last years. Hydrogel structures tethered to a solid substrate has been fabricated by a range of techniques including photolithography, e-beam lithography [62], nanoimprint lithography (NIL) [63], laser interference lithography (LIL) [64] [65] and beam pen lithography [66]. Among these, NIL represents an attractive method for its possibility to scaling up and high-throughput [67]. Since its first introduction, (NIL) is viewed as an alternative nanopatterning technique to

traditional photolithography, allowing micrometer-scale and subhundred-nanometer resolution as well as 3D structure fabrication [68]. The basic NIL process involves a physical deformation of a thin layer of polymer deposited on a substrate by using a mold, followed by a pattern transfer involving the complete removal of the residual polymer in the recessed areas of the pattern. Traditionally the materials used are based on thermoplastic or crosslinkable polymers that can deform, effectively fill, and rigidify in the mold gaps and features. However, NIL presents a uniquely facilitating route for generating patterned functional surfaces. It offers not only the ability to create functional micro- or nano- structures of arbitrary pattern, but the process can be fairly simple and can be accomplished in fewer processing steps, which makes it very attractive in industrial applications.

In the present work, the structuring process is assisted by ultraviolet based NIL (UV-NIL) [69], where the hydrogel with photo-crosslinking agent behaves as photoresist curable by UV-light. The imprint process is shown in Figure 2.2. Basically, a master template is typically produced by e-beam lithography to yield a nanometer-scale relief pattern on a high quality silicon wafer or other suitable substrate.

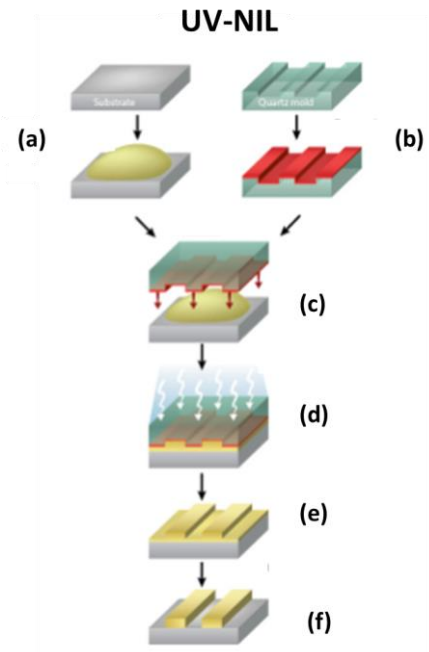

Figure 2.2: UV-NIL process. (a) spin-casting of the photopolymer on a clean substrate; (b) clean and treated imprint mold; (c) alignment and contact of the mold to the substrate; (d) exposure to UV light; (e) detach of the mold; (f) etching of the residual layer.

A daughter imprint soft mold (typically an elastomeric stamp, mostly prepared from polydimethylsiloxane (PDMS)) is then cast from the master template creating an exact negative replica of the original pattern. The soft imprint mold is then used to imprint the resin material. All subsequent UV-NIL is then carried out with the imprint mold; effectively preserving the expensive master template and prolonging its integrity.

2.2 Sensing based on SPR and HOW Spectroscopy

In this study, the sensor is implemented by using a Surface plasmon resonance (SPR) optical setup in which a poly(N-isoproprylacrylamide) (PNIPAAm) nanopatterned hydrogel film is attached on a metallic surface. The hydrogel binding matrix with nanometer thickness can serve as an optical waveguide. Based on the measurement of binding-induced refractive index changes, a hydrogel optical waveguide spectroscopy (HOWS) is reported for a label-free sensor. This biosensor compared to regular SPR biosensor with thiol self-assembled monolayer (SAM), provides an order of magnitude improved resolution in the refractive index measurements owing to its low damping and large swelling ratio, respectively [70].

An optical sensor is a sensing device which, by optical means, converts the quantity being measured (measurand) to another quantity (output) which is typically encoded into one of the characteristics of a light wave. In SPR sensors, surface plasmons are characterized by a (complex) propagation constant and a distribution of their electromagnetic field [71]. The propagation is a solution of an appropriate eigenvalue equation and depends on the refractive index profile of the waveguide and angular frequency of surface plasmon. If the refractive index profile of the waveguide is perturbed, the constant propagation of the surface plasmon changes. The relationship between the change in the propagation constant of a surface plasmon and a perturbation can be analyzed using the perturbation theory [72]. In SPR sensors, a surface plasmon is excited at the interface between a metal film and a dielectric medium (superstrate), and it is characterized by changes in the refractive index of which are to be measured. A change in the refractive index of the superstrate produces a change in the propagation constant of the surface plasmon. This change alters the coupling condition between a light wave and the surface plasmon, which can be observed as a change in one of the characteristics of the optical wave interacting with the surface plasmon [73]. Figure 2.3a illustrates

the surface plasmon propagation along the x-axis parallel to the interface, assuming that the metal occupies the region z<0. (Cartesian coordinate z perpendicular to the metal/dielectric interface).

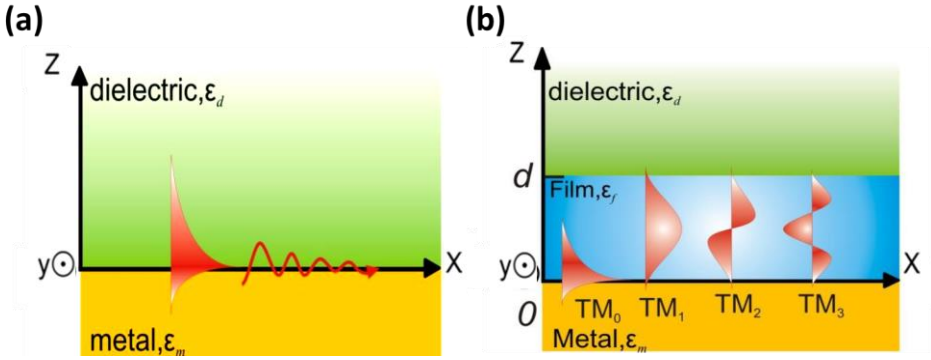

Figure 2.3: Schematic presentation of a (a) surface plasmon at the interface between a metal and a dielectric. (b) optical waveguide modes on a structure with metal (ε_m), film (thickness d, ε_f), and dielectric (ε_d).

If a thin dielectric film is attached on a metal surface (ε_m) and its permittivity ε_f is larger than that of adjacent top dielectric medium (ε_d), additional guided optical waves can be observed as shown in Figure 2.3b. In this configuration the layer is used as an optical waveguide. If the layer attached to a metal is a hydrogel matrix it can support guided light waves if its refractive index and the thickness are sufficiently large. This phenomenon is called hydrogel optical waveguide (HOW).

The surface plasmons (SP) and hydrogel optical waveguide (HOW) can be excited on a same substrate. For this purpose, two types of couplers can be used – *prism coupler* [74], *grating coupler* [75,76] relying on the diffraction of light on periodic modulated metallic surfaces and *waveguide coupling* [77].

In this work, the prism coupler is adopted and the optical excitation of SP is achieved by means of the attenuated total reflection method (ATR) in a Kretschmann configuration. The Kretschmann geometry consists in an optical beam propagating through the prism with the permittivity ε_p, which is made incident under an angle of incidence θ on a thin metal layer at the prism base, Figure 2.4a. Upon the incidence, the optical wave totally reflects and its evanescent field penetrates through the thin metal layer. At the interface between the metal and outer dielectric with lower refractive index ($\varepsilon_d<\varepsilon_p$), surface plasmon can be excited as the momentum of the incident optical wave is higher than the one of an optical wave

propagating in the outer dielectric [78]. In ATR method with Kretschmann configuration, the strength of the coupling between an optical wave and surface plasmon wave can be controlled by varying the thickness of the metal layer [79]. The excitation of SP manifests itself as a narrow absorption dip in the wavelength or angular spectrum of reflectivity, see Figure 2.4b.

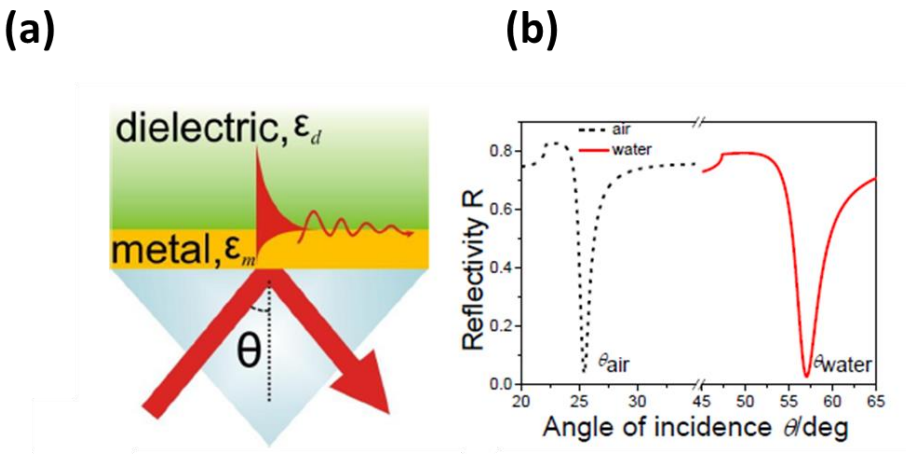

Figure 2.4: Attenuated total reflection method with the Kretschmann configuration for the excitation of surface plasmons, and (b) typical example of angular reflectivity spectrum R(θ).

The angular spectrum of reflectivity and field distribution can be calculated based on Fresnel equations and transfer matrix formalism described in literatures [64, 65].

As said before, the excitation of SP and hydrogel optical waveguide (HOW) can be performed at the same time and in the same substrate, as showed in Figure 2.5a. The evanescent field of a laser beam that is internally reflected at the sensor surface penetrates through the metal layer and can couple to surface plasmon (SP) and hydrogel waveguide (HW) modes propagating along the outer metal interface [80]. As Figure 2.5b shows, the excitation of SP and HW modes is manifested as two distinct dips in the angular reflectivity spectrum R(θ).

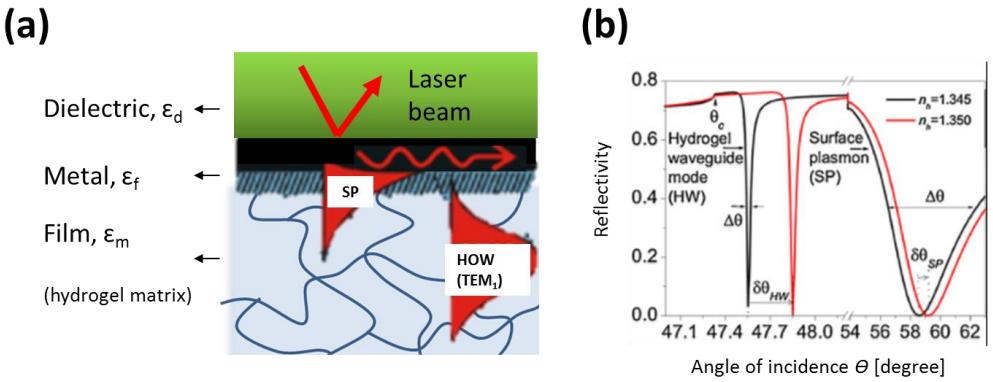

Figure 2.5: (a) SP and HOW (TEM_1) excited by ATR method with the Kretschmann configuration typical example of angular reflectivity spectrum R(θ); (b) Angular reflectivity spectra of HOW and SP on an Au surface with a pNIPAAm-based hydrogel layer.

These dips are located at angles θ for which the propagation constant of the mode β matches the component of the reflected laser beam propagation constant that is parallel to the interface:

$$k_0\, n_p\, \sin\theta\ = Re\,\{\beta\}$$

where $k_0 = 2\pi/\lambda$ is the light propagation constant in vacuum and n_p the refractive index of the glass prism coupler. The propagation constant β of SP and HW can be determined from the dispersion relation:

$$\tan kd_h\ = \frac{\gamma_b n_h^2/kn_m^2 + \gamma_m n_h^2/kn_m^2}{1-(\gamma_b n_h^2/kn_b^2)(\gamma_m n_h^2/kn_m^2)}$$

in which n_m is the refractive index of the metal, n_b is the refractive of the analyzed dielectric medium (air or buffer), n_h the refractive index of the hydrogel layer and $k^2 = (k_o^2 n_h^2 - \beta^2), \gamma_m^2 = (\beta^2 - k_0^2 n_m^2)$ and $\gamma_b^2 = (\beta^2 - k_0^2 n_b^2)$ are the transverse propagation constants in the hydrogel film, the metal and the analyzed medium, respectively. Further, the resonance coupling angle for HOW mode is noted as θ_{HOW} and the one for surface plasmons as θ_{SP}. Both coupling angles increase when increasing the refracting index of the dielectric adjacent to the gold surface n_h. In the time resolved experiments, the angle of incidence θ was set to the location with highest slope $\partial R/\partial\theta$ at the edge of the HOW or SP reflectivity dip below the

resonant angles θ_{HW} and $\theta_{SPR,}$ respectively. A shift in the resonant dips due to the refractive index variations δn_h is measured from induced changes in the reflected intensity δR [58].

Spectroscopy of surface plasmon and hydrogel waveguide waves provides a powerful technique for *in situ* observation of hydrogel films [81]. It allows real-time monitoring of changes in their characteristics such as thickness d_h and refractive index n_h that are associated with variations in optical properties. In order to determine these parameters, the angular reflectivity spectrum $R(\theta)$ exhibiting SP and HW resonance dips is fitted by using a 'box model' based on a transfer matrix-based model.

In this model, the dependence of the refractive index perpendicular to the surface $n(x)$ is assumed to be the following function of the distance from the surface:

$$n(x) = n_d + (n_h - n_b)\, H\, (d_h - x)$$

(n_b is the refractive index of the dielectric medium; n_h is the refractive index of hydrogel and d_h the thickness of the hydrogel)

where x is the axis perpendicular to the sensor surface (x=0 is the position at the interface between the metal and hydrogel) and H is the Heaviside step function. A constant refractive index of the hydrogel n_h perpendicular to the surface is assumed, from which the mass density Γ can be calculated as:

$$\Gamma = (n_h - n_b)\, d_h \frac{\vartheta c}{\vartheta n_h}$$

where the coefficient $\partial n_h/\partial c \sim 0.2$ mm^3 mg^{-1} relates changes in the refractive index and concentration of organic materials in the hydrogel (e.g., polymer or proteins). From effective medium theory follows that polymer volume fraction f of a swollen hydrogel is equal to:

$$f = \frac{(n_h^2 - n_d^2)(n_{h-dry}^2 + 2n_d^2)}{(n_h^2 + 2n_d^2)(n_{h-dry}^2 - n_d^2)}$$

where $n_{h\text{-}dry}$ is the refractive index of hydrogel in dry state.

2.3 Optical waveguide-enhanced diffraction measurements

The *in situ* observation of thin micro-structured hydrogel is reported in many works [66], in which only surface plasmon-enhanced diffraction measurements are performed. As described in the previous subsections, this technique allowed for reference-compensated observations of swelling and collapsing hydrogel layers that occurred predominantly normally to the surface (1D) [82]. Our studies provide an extension of this approach and it reports on the optical observation of hydrogel nanostructures that can swell and collapse in 3D. Weak refractive index contrast of hydrogel structures arranged in periodic pattern and swollen in water is generally associated with intrinsically low diffraction efficiency. In order to enhance the intensity of diffracted light, the surface was probed by resonantly excited optical waveguide modes, taking advantage of the fact that the hydrogel can serve as optical waveguide (HOW) enabling the excitation of additional modes besides surface plasmons.

It is based on optical waveguide-enhanced diffraction measurement that in conjunction with appropriate model allows for quantitative investigating of swelling and collapsing of small hydrogel structures that otherwise provide small optical contrast. By using an implemented optical model, the measured changes in diffraction efficiency are translated to the swelling ratio variations of the nanostructures. This method is applied for the investigation of swelling and collapsing of pNIPAAM-based hydrogel nanopillars that are prepared by UV–NIL. The obtained optical results are compared to Atomic Force Microscopy measurements of the topographic surface structure and unusual behavior (that is not observed for small aspect ratio microstructures) is discussed.

2.3.1 Surface architecture

The photo-crosslinkable hydrogel used as binding matrix is a pNIPAAm-based hydrogel, and it consists in a random terpolymer, composed of N isopropylacrylamide, methacrylic acid (MAA), and 4-methacryoyloxy benzophenone in a ratio of 94:5:1. It is synthesized by free radical polymerization and thoroughly characterized at the University of Siegen [83]. The N-isopropylacrylamide provides thermo-responsive characteristics of the terpolymer, the benzophenone moieties enable its photo-crosslinking, and the MAA is be used for postsynthetic modification and it improves the swelling properties. The chemical structure is presented in Figure 2.6a and the molecular weight of used polymer is 2.49×105 g mol^{-1} and the dispersity is 3.05. pNIPAAm hydrogel with

LCST of 32°C exhibits a swollen behavior below the LCST, while above it shows a collapsed state, see Figure 2.6b.

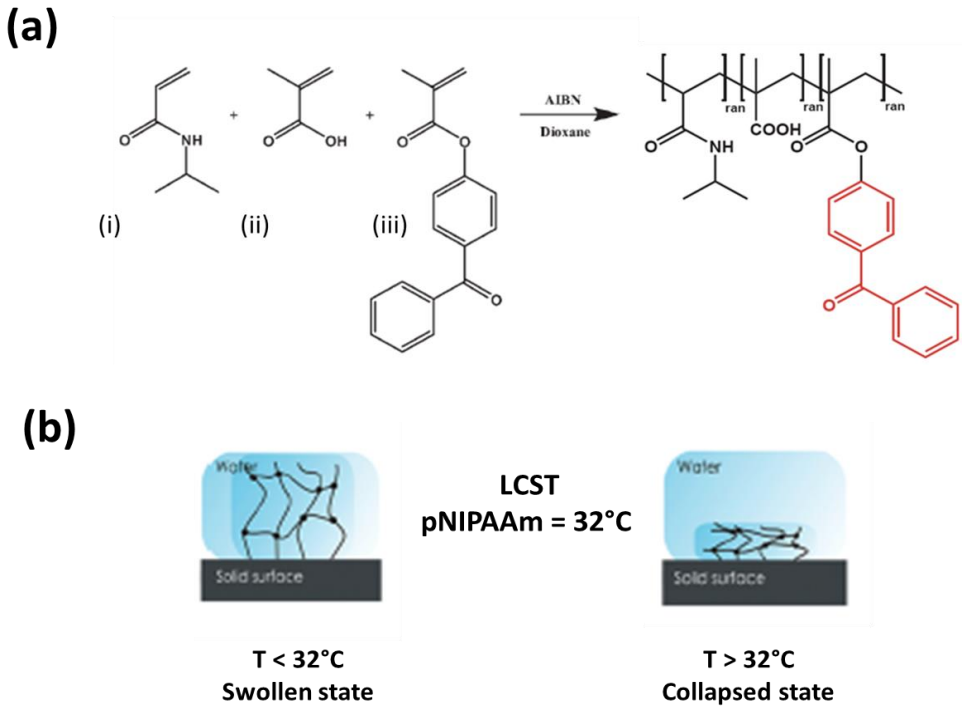

Figure 2.6: (a) Chemical structure of pNIPPAm-based polymer composed of (i) N-isopropylacrylamide, (ii) methacrylic acid (MAA), and (iii) 4-methacryoyloxy benzophenone. (b) Typical behavior of pNIPPAm-based hydrogel tethered to a solid substrate.

pNIPAAm hydrogel film is prepared on high-refractive index LaSFN9 glass substrate that is subsequently coated with 2 nm Cr and 47 nm Au film by vacuum thermal evaporation (FL4000, HHV ltd., UK). In order to promote adhesion of pNIPAAm layer to the Au surface, a thin SU-8 film is spun on its top. SU-8 from Micro Resist Technology GmbH (Germany) diluted with SU-8 thinner at ratio of 1:50 is spin coated onto the Au surface at 5000 rpm for 60 s with 1s, 500 rpm ramping time. Then, the substrate is dried in a vacuum oven for 2 h at 50 °C. Afterward, pNIPAAm polymer (from an ethanol solution at a concentration of 60 mg/mL) is spin coated at 2000 rpm for 2 minutes and dried overnight at 50°C in a vacuum oven. The thickness of SU-8 linker layer ≈ 10 nm and the thickness of dry

pNIPAAm film after rinsing with ethanol and water is ≈ 300 nm as measured by SPR and HOW.

The array of hydrogel nanopillars is prepared by means of UV-nanoimprint lithography technique (UV-NIL), according to following procedure. The dry film is imprinted by using a polydimethylsyloxane (PDMS) working stamp, prepared from a Si wafer with a rectangular array of nanoholes (diameter= 90 nm, depth = 260 nm, and period Λ=460 nm, fabricated by e-beam lithography at Temicon GmbH. (Germany). Since that the provided Si master is composed of nanoholes and the hydrogel film should be patterned with nanopillars, the Si master structure with the area of 1 cm^2 is transferred to the PDMS mold in two steps by using OrmoStamp toolkit provided by Micro Resist Technology GmbH (Germany). In the first phase, OrmoStamp polymer is dispensed on the Si master and putted in contact with a glass substrate, previously coated with an adhesion promoting layer, called OrmoPrime08. Afterwards, the OrmoStamp polymer is crosslinked by UV light (irradiation dose 1 J/cm^2 at a wavelength of λ=365 nm), then detached from the Si master and thermal post cured at 130 °C for 30 minutes. At this point, the Ormostamp inverse copy with array of pillars is treated with a fluorosilane based anti-sticking layer. This layer is prepared by vapor-deposition of 1H,1H,2H,2H perfluorooctyl-trichlorsilane from Sigma Aldrich in a desiccator at 250 °C. In the second step, the as-prepared OrmoStamp with nanopillars structure is used as new master. The PDMS prepared from Sylgard 184 (Dow Corning, USA) by mixing the curing agent with the base at a 1:10 (v/v) ratio. 3 mm thick layer of the PDMS mixture is poured onto the OrmoStamp master and thermally cured for 2 hours at 60 °C. After curing the PDMS stamp is peeled from the master rinsed with ethanol and dried by blowing nitrogen to clean its surface. All the results obtained from this experiment are summarized in ***Publication I*** [84]**.**

The imprinting process of pNIPAAm polymer layer is illustrated in Figure 2.7. The PDMS working stamp that carried arrays of nanoholes is soaked in ethanol for several minutes, allowing the PDMS polymer network to absorb the solvent vapors. Then, the surface of the stamp is dried with a stream of air over several seconds and then brought into conformal contact with the pNIPAAm film. At this point, additional 10 µL of ethanol are dispersed on the top of the stamp, in the opposite side not in contact with the pNIPAAM film. As shown in Figure 2.7a, ethanol diffuses from the PDMS to pNIPAAm layer and partially dissolves the polymer, so its upper part become fluid and fills up the casted nanoholes. The PDMS stamp was kept in contact with pNIPAAm in ambient atmosphere at room temperature for 1 h followed by overnight drying in vacuum. Afterwards, the

PDMS stamp is detached from polymer surface leaving imprinted arrays of nanopillars at the surface of pNIPAAm layer (d_{hp}) and a residual layer (d_{hl}), as illustrated in Figure 2.7b.

After storage in vacuum at elevated temperature of 50 °C for several hours, the imprinted pNIPAAm layer is then irradiated with UV light at wavelength λ = 365 nm and dose of 10 J cm^{-2} (UV chamber Bio-Link 365, Vilber, Germany), in order to crosslink the polymer chains.

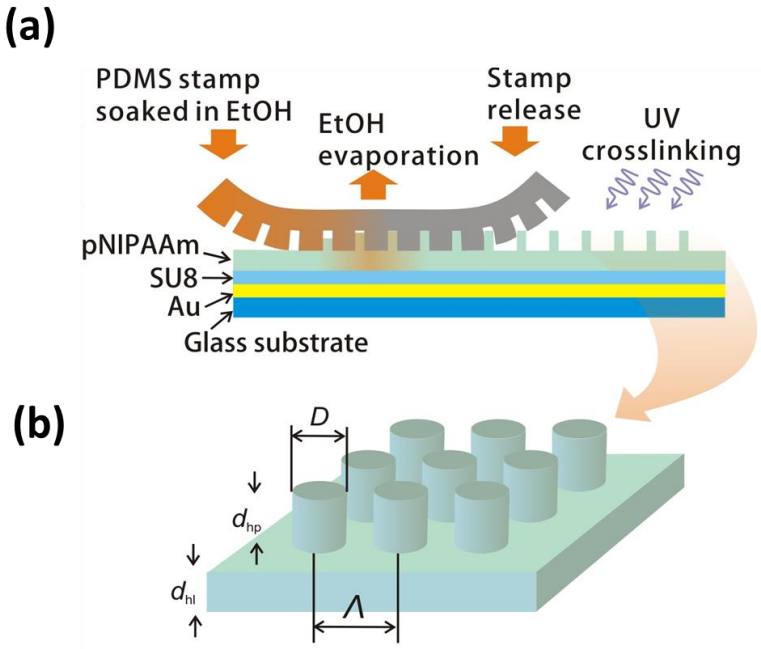

Figure 2.7: (a) Sensor architectures and imprinting process; (b) geometry of pNIPAAm-based hydrogel structure [84].

The topographic structure of freshly imprinted and photo-crosslinked pNIPAAm hydrogel nanopillars is investigate in air at room temperature by AFM from Molecular Imaging (USA). The surface is probed in tapping mode by n^+-silicon cantilevers (PPP-NCHR, Nanosensors, Switzerland) with a spring constant with a spring constant of 42 Nm^{-1}. Figure 2.8a reveals that as-prepared pNIPAAm nanopillar arrays, before any contact with a swelling solvent, exhibits the same period of Λ = 460 nm as the Si master structure, smaller height of imprinted nanopillars ($d_{hp} \approx$ 208 nm) and the diameter D = 130 nm (measured at half of the maximum height) is wider than the original one, probably due to the multistep

replication process. If the cross-linked pNIPAAm nanopillar arrays and the underlying residual layer are allowed to swell in water at temperature T = 22 °C, the structure is completely erased after the subsequent drying at the same temperature (see, Figure 2.8b), showing the same aspect of a flat surface. Interestingly to note here, when the surface is swollen again in water at T = 22 °C and dried at a higher temperature of T = 38 °C after the temperature-induced volume collapse, the array topography of the nanopillars partially recovers the original shape on the surface, see Figure 2.8c. As a possible explanation, the strong surface tension of the air–water interface as it passes over the surface structure during water evaporation, lead to a topographic erasure of the array features upon drying at low temperature [85]. This process induces the rearrangement of the swollen polymer chains as the surface tension strongly competes (and apparently exceeds) the elastic restoring force of the swollen polymer network. This hypothesis is confirmed by the observation of structure recovery when drying is performed at temperatures above the LCST of 32 °C for the used NIPAAm copolymer [86]. In this case, the temperature-induced collapse of the pNIPAAm network leads to a substantial increase of the elastic modulus in the hydrogel material. It exceeds the drying forces induced by the water meniscus and thus the nanopillar topography is preserved during water evaporation.

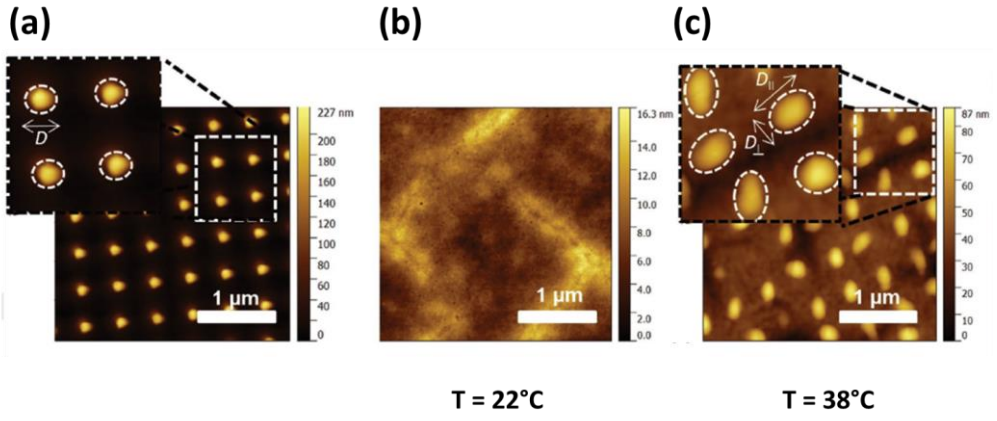

Figure 2.8: AFM observation performed in air of (a) freshly prepared pNIPAAm nanopillars compared to the structure that is swollen in water and dried at different temperatures (b) T= 22°C; (c) T=38°C. The scale bar is the same for the three microscopy images [84].

Anyway, the shape of the pillars that are swollen and dried at higher temperature (Figure 2.8c) compared to that of the freshly prepared arrays are changed (Figure 10a). The height of the nanopilars (d_{hp} = 76 ± 6.8 nm) is decreased, as well as the original shape is changed, showing an elongated elliptical footprint with the width in the half maximum of $D_{\parallel}$= 288 ± 12.0 nm and $D_{\perp}$ = 205.5 ± 6.6 nm along the long and short axis, respectively, after drying at elevated temperature of T = 38 °C. The prolonged shape of dry nanopillars indicates that they bend upon the collapse or during the drying step of pNIPAAm hydrogel. Interestingly, volume of swollen and collapsed nanopillars stayed approximately the same ($3.4 \times 10^{-3} \pm 0.5 \times 10^{-3}$ μm^3 of pristine nanopillars and $3.55 \times 10^{-3} \pm 0.4 \times 10^{-3}$ μm^3 after the swelling and collapsing defined as $\pi D_{\parallel} D_{\perp} d_{hp}/4$).

2.3.2 *In situ* observation of responsive hydrogel nanostructures

The nanostructured pNIPAAm is optically probed by OWS by employing the attenuated total reflection (ATR) method in Kretschmann configuration, described in details in the previous subsection 2.2. The optical system allowed for the resonant excitation of optical waveguide modes, is illustrated in Figure 2.9.

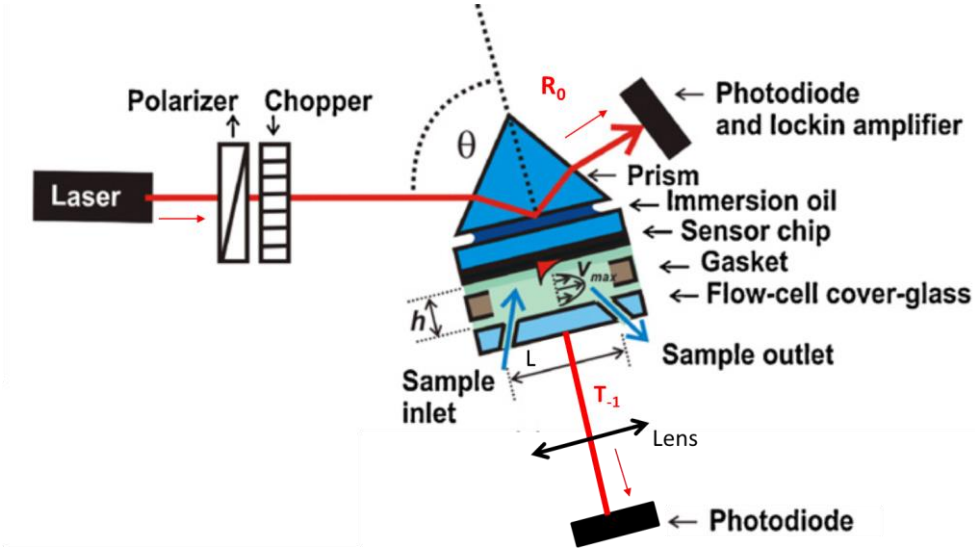

Figure 2.9: Optical set-up employed for probing the swelling and collapsing of pNIPAAm hydrogel nanostructure by optical waveguide spectroscopy and optical waveguide-enhanced diffraction.

A collimated monochromatic light beam, emitted by a He-Ne laser (SPT, CVI Melles Griot, Germany), at wavelength of $\lambda = 633$ nm with its intensity modulated by a chopper is coupled to a 90° LASFN9 glass prism. Transverse magnetic (TM) and transverse electric (TE) polarization of the incident laser beam was selected by a rotation polarizer and the area illuminated on the surface was of several mm^2. The glass substrate with Au film and imprinted pNIPAAm layer is optically matched to the prism base. A flow cell with a volume of 25 µL is attached to the sensor surface to flow liquid samples at 0.5 mL/min by using a peristaltic pump. The temperature of water that was flowed through the flow-cell was controlled by a Peltier device, connected to a driver LFI3751 from Wavelength Electronics (USA). The whole assembly of prism, glass substrate, and flow cell is mounted on a two-arm coaxial goniometer for the control of the angle of incidence θ (measured outside the prism). The laser beam is partially reflected and partially scattered in a series of diffraction orders upon its incidence at the surface with the periodic arrays of pNIPAAm nanopillars. The intensity of reflected light beam R_0 is detected by a photodiode connected to a lock-in amplifier 7260 from EG&G (USA). An identical detector is used to measure the intensity of -1^{st} order diffracted beam T_{-1} transmitted through the flow cell. The data acquisition, image processing and control of the overall sensor system is performed by using a home-developed LabVIEW-based software (National Instruments, USA) and by the software Wasplas (Max Planck Institute for Polymer Research in Mainz, Germany). The reflectivity spectrum $R_0(\theta)$ is analyzed by fitting with a Fresnel-based model implemented in the software Winspall (Max Planck Institute for Polymer Research, Mainz, Germany) [58]. In this analysis we use the follow refractive index values, @λ=633nm, Au = 0.2 + 3.51i, Cr = 3.14 + 3.3i and SU-8 = 1.48 and the thickness is determined by fitting reflectivity spectra $R_0(\theta)$ measured on respective reference samples prior to their coating with pNIPAAm. As said before, a "box model" is used for the investigation of 1D swelling of pNIPAAm hydrogel film, (assuming a thickness d_{hl} and homogeneous refractive index over the whole hydrogel layer n_{hl}). In order to capture changes in the geometry of nanopillars from variations in the T_{-1} spectrum, a numerical model based on finite element method was employed. This method was implemented in a diffraction grating solver DiPoG developed at the Weierstrass Institute (Germany). The structure was approximated as a linear binary grating with the surface modulated only in lateral direction in the plane of incidence and it was described by width D and height d_{hp} of a dielectric ridge (see Figure 2.10). The mesh size of the unit cell with a stack of layers and a ridge with the width D and height d_{hp} was adjusted in order to converge simulated reflectivity R_0 and diffraction efficiency T_{-1}.

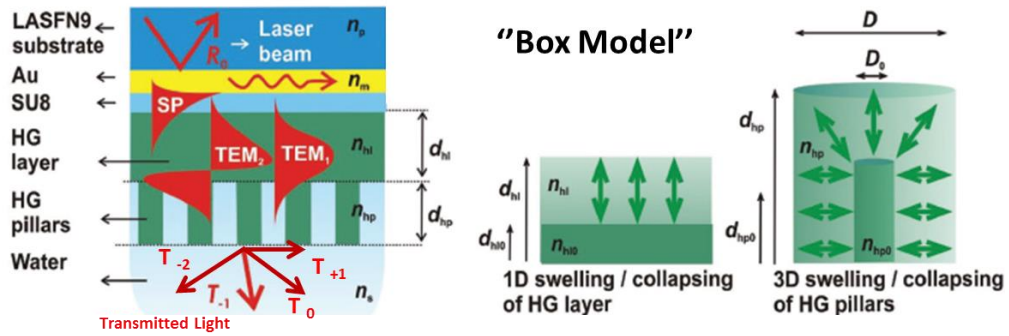

Figure 2.10: Sketch of the sensor surface architecture probed by surface plasmon (SP) and optical waveguide (TEM) modes travelling along the surface. Box model assumed to investigate the 1D and 3D swelling/ collapsing of hydrogel (HG) layer [84].

The observation is carried on by investigation the resonantly excited $TE_{0,1}$ and $TM_{1,2}$ waveguide modes travelling along the surface with the hydrogel film manifested as series of characteristic dips in the reflectivity spectrum $R_0(\theta)$. The hydrogel layer is used to support the modes and the propagation of light is confined by the reflective Au surface at the inner interface and by total internal reflection at the outer interface between the hydrogel (exhibiting higher refractive index n_{hl}) and water (exhibiting lower refractive index n_s). Figure 2.11 shows a preliminary analysis performed on a flat and nanostructured pNIPAAm hydrogel swollen in water by measuring the reflectivity variation upon rapid change of temperature from room temperature to 50°C, in transverse magnetic ($TM_{1,2}$).

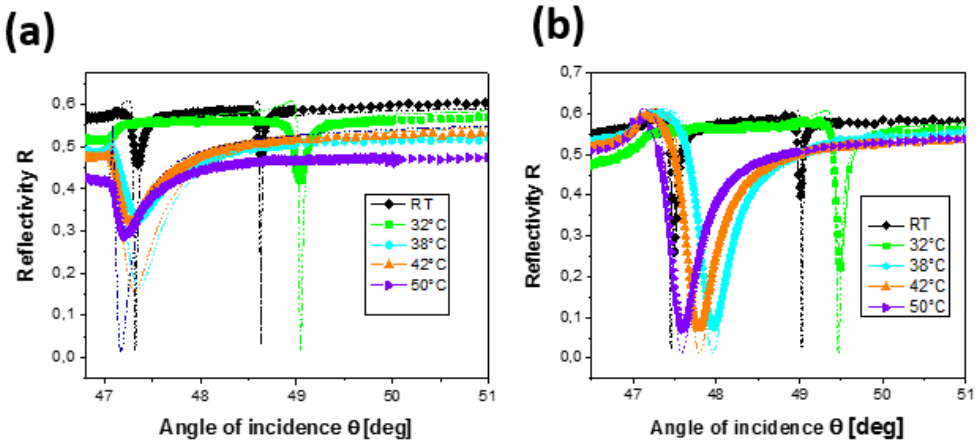

Figure 2.11: Reflectivity spectrum $R_0(\theta)$ of (a) flat pNIPAAM-based hydrogel and (b) nanoimprinted pNIPAAm hydrogel in the same condition at different temperatures Teq = 23°C, 32°C, 38°C, 42°C, 50°C.

The reflectivity spectrum of the structured hydrogel (Figure 2.11b) compared to flat one (Figure 2.11a) presents just a slight shift of the characteristics dips towards higher angles, this confirm the presence of the nanopillars structures on its surface. So since the flat and the structured spectra are comparable, the following test is carried on considering the structured film at temperatures of T= 22°C, 31°C, 38°C and 50°C, in transverse magnetic ($TM_{1,2}$) and in this case even transverse electric ($TE_{0,1}$) polarization, as shown in Figure 2.12.

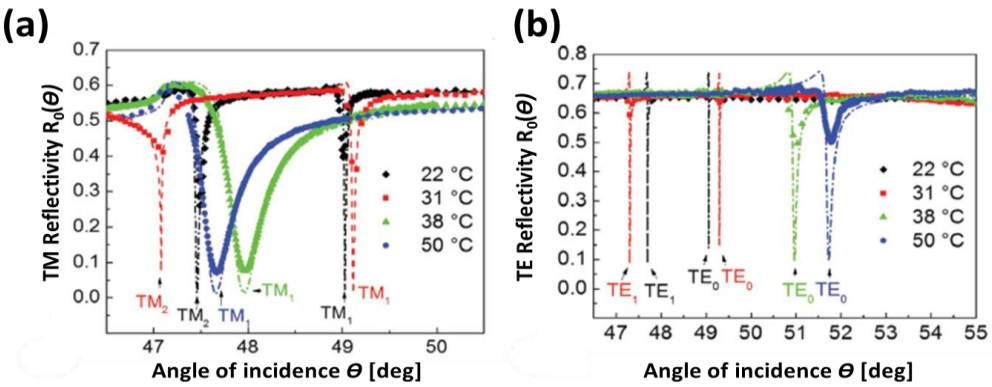

Figure 2.12: Angular reflectivity R0(θ) spectra measured with a) TM and b) TE polarized light for a nanopillar-imprinted pNIPAAm hydrogel layer, at temperatures T = 22, 31, 38, and 50 °C. Symbols indicate measured data and lines show respective fits [84].

In both configuration, the swollen pNIPAAm-based hydrogel film at low temperature below LCST supports two waveguide modes in transverse magnetic ($TM_{1,2}$) and transverse electric ($TE_{0,1}$) polarization. If the temperature increases above the LCST, the layer starts to collapse and only one waveguide mode is observed in each polarization. In figure 2.12, the reflectivity curves are fitted with the transfer matrix-based model in order to determine thickness d_{hl} and refractive index n_{hl} of the pNIPAAm layer. Figure 2.13 reveals the results summarized, in which the refractive index n_{hl} and the thickness d_{hl} of hydrogel flat and imprinted are plotted against the temperature T. The swollen pNIPAAm layer at room temperature T = 22 °C exhibits a thickness of d_{hl} = 2.3 µm and refractive index of

n_{hl} = 1.356; while the temperature is increased above LCST = 32 °C, the hydrogel layer starts to abruptly collapse (d_{hl} = 380 nm,) until further raising the temperature to T = 50 °C, exhibits a refractive index increas to n_{hl} = 1.47. Three relevant phases are identified, corresponding to different behavior of the pNIPAAm hydrogel upon an increase of temperature, the sketches are confirmed by AFM analysis showed before (see Figure 2.8). We clearly observe that an increase of temperature causes an increase of refractive index, this means a decrease of thickness.

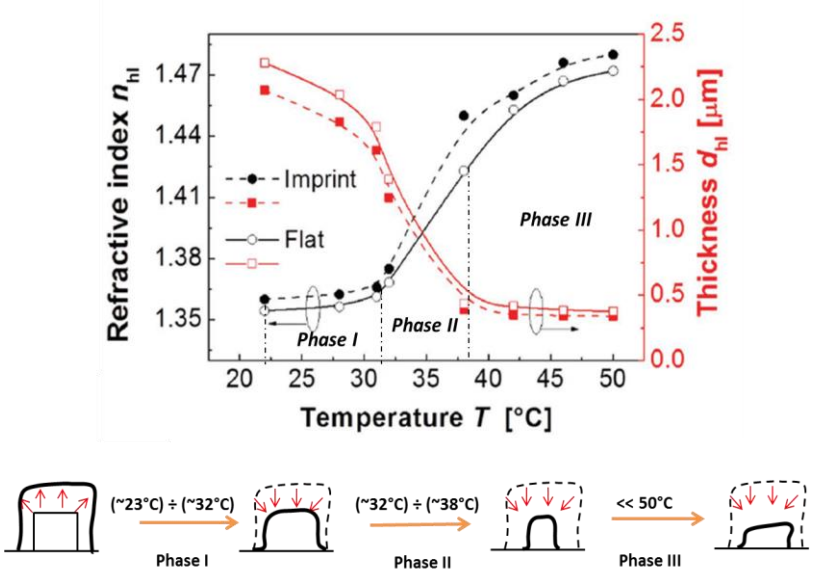

Figure 2.13: Refractive index n_{hl} and thickness d_{hl} plotted as a function of temperature with flat and imprinted surface. Illustrative scheme of the different behavior of hydrogel layer in water.

The imprinted nanopillar structure in the upper surface of the pNIPAAm layer weakly affected the spectrum of guided waves in $R_0(\theta)$ and thus the evaluated thickness d_{hl} and refractive index of structured and flat surface are similar. The reason is during the imprinting of the nanopillars, in which only a small volume fraction (few percent) of the underlying polymer layer is tranferred into the pillar volume, which led to only a slight decrease in its thickness d_{hl}. In figure 2.14 the Swelling Ratio (SR) is plotted as a function of temperature, determined as the ratio of the thicknesses d_{hl} in swollen and dry states for both imprinted and non-imprinted pNIPAAm layers. The swelling ratio of the hydrogel layer is SR ≈ 6 at room temperature, and about 4.5 at 32°C. This parameter is inversely proportional to the

polymer volume fraction ΦP of the swollen hydrogel material with water, which can be obtained from Maxwell Garnett effective medium theory [86] as

$$\Phi_P = \frac{n_{hl}^2 - n_{hlo}^2}{n_{hl}^2 - 2n_{hlo}^2} \Big/ \frac{n_s^2 - n_{hlo}^2}{n_s^2 - 2n_{hlo}^2}$$

where $n_{hl0} = 1.48$ is the refractive index of the (dry) polymer and n_s is the refractive index of the water phase $n_s = 1.332$ [87].

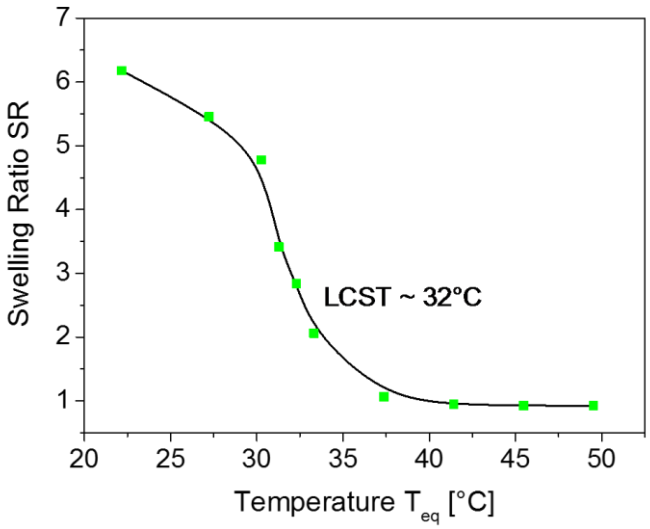

Figure 2.14: Swelling ratio vs Temperature.

The obtained value for the polymer volume fraction at room temperature of $\Phi_P = 0.17$ is consistent with the swelling ratio calculated from the volumetric change SR ≈ 6. ($\Phi_P = 1/SR$).

The optical waveguide-enhanced diffraction measurements are carried out by measuring changes in the intensity of -1 diffraction order T_{-1}. The light beam hits the surface (optically matched to the prism in such orientation that the structure lies in the plane of incidence) at angles above the critical angle ($\theta > 47°$). It is partially reflected back into the prism (R_0 signal) and partially diffracted to -1^{st}

diffraction orders toward the prism (R_{-1}) and toward water (T_{-1}), as illustrates in the setup, Figure 2.9. Worth to note, that for the chosen period $\Lambda = 460$ nm the -1^{st} diffraction orders travel at angles θ that are close to zero as indicated in Figure 2.10. Unlike the reflected diffraction order R_{-1}, the intensity of transmitted beam T_{-1} can be easily detected through the transparent flow cell. The spectra in Figure 2.15 are measured at temperatures between T = 22 and 50 °C and and shows the dependence of the T_{-1} intensity on the angle of incidence θ for TM and TE polarized light beams. They reveal that the overall (relative) T_{-1} intensity does not vary with temperature and it can be ascribed to the background signal. However, a series of strong peaks above this background occurs at angles θ where $TE_{0,1}$ and $TM_{1,2}$ modes are resonantly excited and where the diffraction intensity is amplified. Within this framework, interestingly to note is that the diffraction of TE polarized light is accompanied with much stronger intensity than that for TM polarization.

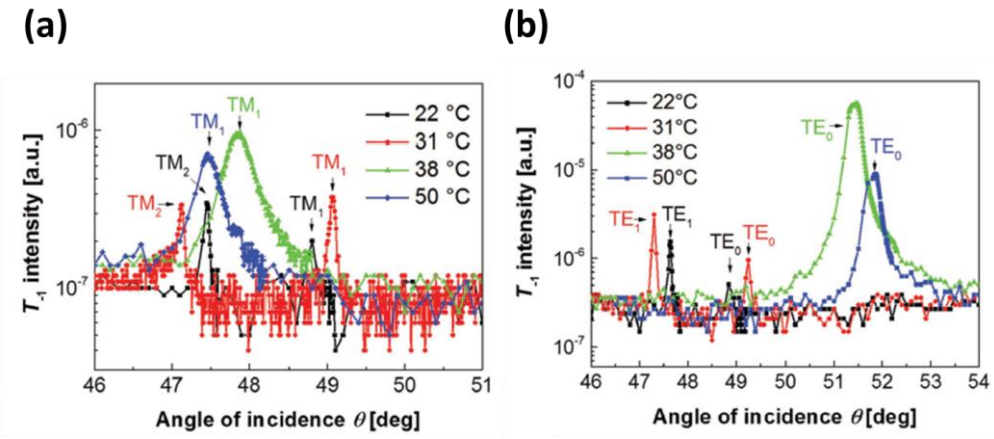

Figure 2.15: Transmitted beam intensity T_{-1} angular spectra for (a) TM and (b) TE polarization [84].

As presented in Figure 2.16, diffraction intensity of the peak associated with the coupling to TE_0 mode increases by a factor up to 30 when changing the temperature from T = 22 to 38 °C. This can be attributed to a shrinking of the hydrogel pillars that translates to an increase of their polymer volume fraction Φ_p. These changes lead to higher refractive index of nanopillars n_{hp} and thus enhanced optical contrast of the hydrogel diffraction grating. The magnitude of observed variations in the peak intensity amplified by TM_1 mode is lower than that for TE_0 mode. The reason is that the weaker TM polarized signal is partially masked by background (indicated as a dashed line in Figure 2.15). Therefore, further only TE

polarization is used for the investigation of swelling characteristics of prepared pNIPAAm nanopillars. The measured diffraction intensity T_{-1} enhanced by the resonant coupling to TE_0 waveguide modes exhibits its maximum at a temperature of T ≈ 38 °C. Above this temperature the diffraction intensity gradually decreases and drops again by a factor of about 6 at a temperature of T = 50 °C.

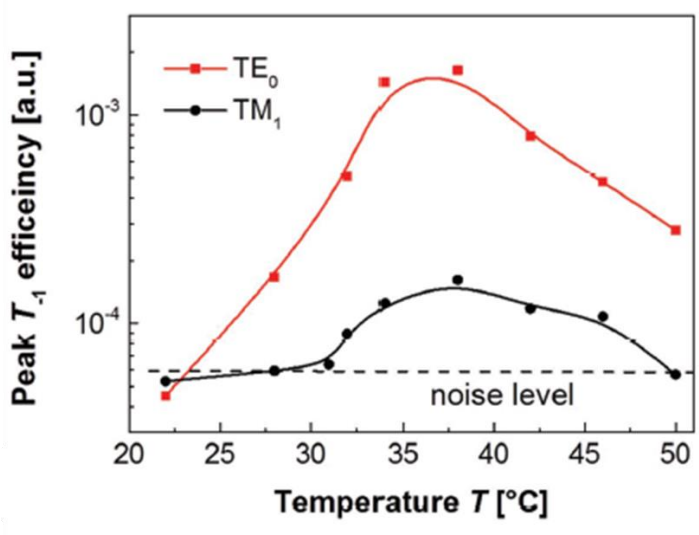

Figure 2.16: Diffraction intensity T_{-1} peak upon the resonant excitation of TE_0 and TM_1 modes [84].

The measured dependence of the diffracted beam intensity T_{-1} on temperature was compared with simulations in order to estimate the swelling ratio of the pNIPAAm nanopillars. In the performed simulations, the values for the thickness d_{hl} and refractive index n_{hl} of residual pNIPAAm layer were determined by OWS as described in the previous theoretical section 2.2. The swelling of nanopillars was assumed to increase their height $h_{hp} = \alpha h_{hp0}$ and diameter $D = \alpha D_0$ by the same factor α (representing a 3D swelling process in contrast to the 1D swelling of the surface-attached hydrogel layer).

The refractive index of the hydrogel nanopillar n_{hp} was assumed homogenous and depends on polymer volume fraction Φ_p as follows from effective medium theory [86].

$$n_{hp} = n_s \sqrt{\frac{n_p^2\left(1 + 2\Phi_p\right) + n_s^2\left(2 + 2\Phi_p\right)}{n_p^2\left(1 + \Phi_p\right) + n_s^2\left(2 + \Phi_p\right)}}$$

In order to simplify the numerical analysis, the structure was periodic only in the direction in the plane of incidence (i.e., the nanopillars were represented by ridges with a width D and height h_{hp}). Then the polymer volume fraction of such hydrogel feature can be described by the volume ratio in the swollen and dry states as $\Phi_p = D_0 h_{hp0}/D h_{hp}$. In this equation, the values measured for dry nanopillars are D_0 = 130 nm h_{hp0} = 208 nm. In order to translate changes in the optically measured diffraction intensity to the variations of the nanostructure volume, the dependence of T_{-1} diffraction efficiency on the polymer volume content Φ_p was simulated for angles θ where TE_0 and TM_1 modes were resonantly excited. The obtained data plotted in Figure 2.17a show that the diffraction efficiency T_{-1} amplified by the resonantly excited waveguide modes increases with the polymer volume content of the nanopillars Φ_p which is inversely proportional to the nanopillar volume. Interestingly, the amplification by TE_0 mode translates to T_{-1} intensity that is ≈100-fold higher than that for the TM_1 mode. The experimentally observed drop in the coupling efficiency can be ascribed to small variations in the thickness of the pNIPAAm layer dh, which smear resonances in the measured reflectivity [manifested as lower depth of reflectivity dip in $R(\theta)$]. Such smearing is more pronounced for the excitation of TE modes, which exhibit much narrower resonances than TM modes due to the stronger Ohmic losses in the metallic Au film. The swelling ratio of prepared pNIPAAm nanopillars was estimated by comparing the simulated diffraction efficiency with the measured values. The log–log plot presented in Figure 2.17a shows a linear decrease of T_{-1} diffraction efficiency with decreasing polymer volume fraction Φ_P. From its slope the change of polymer volume fraction Φ_P by about five times was estimated for the experimentally observed 30-fold change in T_{-1} diffraction efficiency (see Figure 2.16). Assuming that the collapsed nanopillars exhibit Φ_P = 0.8–0.9 at around 38 °C, the polymer volume fraction of the structure in the swollen state at T = 22 °C of Φ_P = 0.17–0.2 is predicted based on these results. Indeed, such swelling ratio is similar to that measured for the pNIPAAm layer composed of identical polymer network attached to a solid support. This observation does not agree with Flory–Rehner theory which suggests that a hydrogel structure which can expand in 3D swells more than a tethered hydrogel film of which swelling is constrained to 1D [53]. A possible explanation for the observed behavior is that the 3D swelling of nanostructures becomes restricted when their size is comparable to the radius of gyration of the polymer chains. The effect of nanopillars bending that changed

measured T_{-1} diffraction was captured by simulating the optical response for different aspect ratios h_p/D. In these simulations, the volume of a hydrogel feature was kept constant $h_pD = h_{p0}D_0$ and the refractive index was set to $n_{hp} = 1.47$. Data presented in Figure 2.17b correspond to diffraction on nanopillars in the collapsed state and they confirm that lowering the aspect ratio decreases the diffraction efficiency.

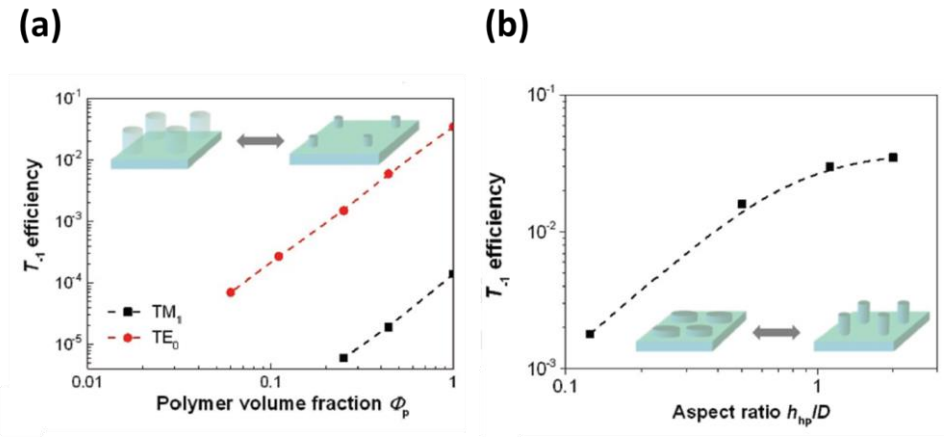

Figure 2.17: (a) Simulated diffraction efficiency T_{-1} (supported by a swollen hydrogel film) depending on the polymer volume fraction of the nanopillar Φ_P. (b) Simulated dependence of T_{-1} diffraction efficiency amplified by TE1 mode (supported by a collapsed hydrogel film) for varied aspect ratio of the collapsed nanopillar ($n_{hp} = 1.47$) [84].

This observation is consistent with the measured drop of the diffraction efficiency when raising the temperature from T = 38 to 50 °C (see Figure 2.16). The measured decrease in aspect ratio of 6 corresponds to the decrease in aspect ratio of ≈6 based on simulations in Figure 2.17b. In order to verify the OWS data on the swelling and collapsing of imprinted pNIPAAm nanopillars, in situ AFM measurements were carried out in water at temperatures varied from T = 22 to 50 °C. At lower temperatures T < 30 °C, the imprinted structure was not discernible under the applied AFM conditions and the topography of the soft pNIPAAm surface exhibited only irregular wavy features (see Figure 2.18a). Such features can be attributed to a buckling process that is associated with a lateral swelling stress resulting from the covalent surface attachment of the polymer network. This confinement leads to anisotropic swelling of the underlying pNIPAAm layer predominately in the direction perpendicular to the surface. It is worthwhile noting that such buckling behavior was observed for other hydrogel films with thicknesses

of several tens of µm and a cross-link density gradient perpendicular to the surface to which they were attached [88]. Such a cross-link density gradient was also observed by OWS for the herein used pNIPAAm-based films with a swollen thickness of several µm [83]. When the temperature approached the LCST of the pNIPAAm network, the imprinted nanopillar structure became apparent in AFM images measured under water. Figure 2.18b–d illustrates that the height dhp and diameter D of the periodic features decreased with temperature T. The height of contracting pillars of ≈45 nm was observed at T = 31 °C and it shrunk to ≈30 nm at T = 50 °C. In addition, Figure 2.18d clearly indicates that the imprinted pillars bend and lay randomly oriented on the surface at temperatures well above the hydrogel LCST. This is similar to the observations in air (see Figure 2.18c) but under the present conditions of full immersion in water this effect cannot be due to the surface tension upon the drying and it is rather associated with increasing hydrophobic attraction between the pNIPAAm pillars and the underlying pNIPAAm polymer film. The associated hydrophobicity of the pNIPAAm polymer network gradually increases with temperature, as previously reported for AFM studies on similar pNIPAAm-based layers [59].

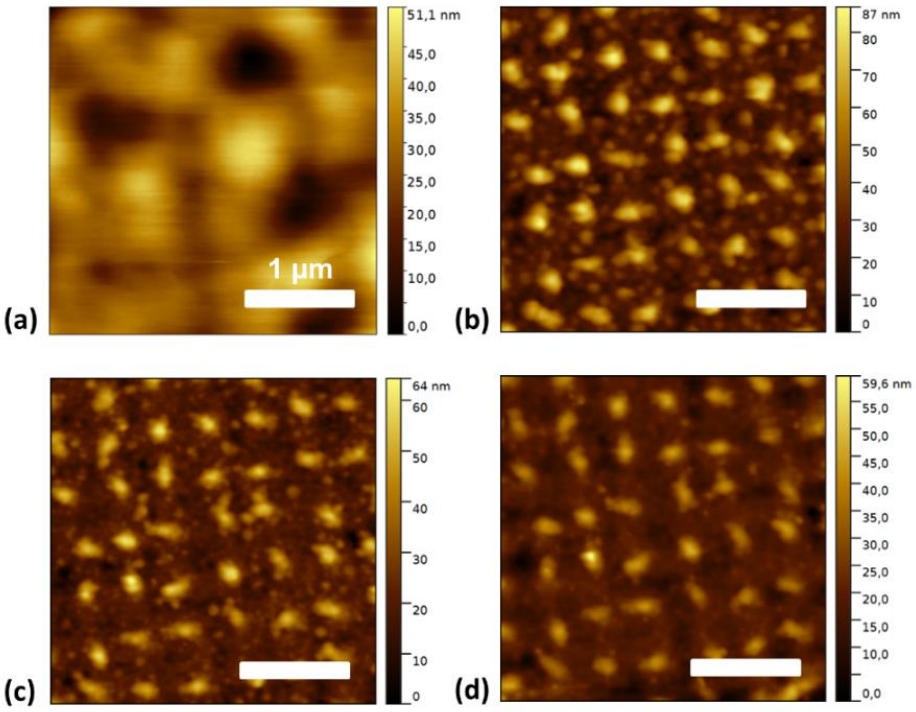

Figure 2.18: *In situ* AFM observation in water of pNIPAAm hydrogel nanopillars at temperatures a) T = 22 °C (swollen), b) 31 °C (beginning to collapse), c) 38 °C (collapsed

and starting to bend), and d) 50 °C (collapsed and bend). The scale bar is the same for the three microscopy images [84].

To conclude, the temperature-induced collapsing of pNIPAAm leads to the preservation of the nanopillar structure during drying. Bending of these structures is observed when the temperature is raised above the LCST, which is explained by the attractive hydrophobic interaction with the underneath hydrogel surface. The structure can be reversibly erased by drying at temperatures below the LCST and recovered by swelling at temperature below LCST and drying at elevated temperatures above the LCST. As compared to previous works [82], the presented approach provides versatile platform for *in situ* observation of low refractive index contrast nanostructures from materials like highly swollen hydrogels.

3

Azobenzene: photocontrol through photoisomerization

Light, is the second attractive trigger studied in the present dissertation, since it offers precise and fast switching and spatial control from remote distances. Within this framework, photocromic molecules are widely employed to prepare light-responsive materials they can be reversibly switched by light between two different conformational states that exhibit distinct spectroscopic and physical properties [89]. Photochromic materials have been extensively studied for their versatile and fascinating response to light, because due to photon absorption they undergo on modifications that lead to changes in material properties such as shape, phase, wettability, permeability and solubility [90]. The most broadly investigated photochromic compounds are the azobenzene derivatives. The interesting light-induced phenomena in this materials has been under attention of scientist, due to the efficient and reversible photoisomerization of the azobenzene molecules, that can be used to induce various types of molecular motions into the material system, being the key to a number of unique optical and photomechanical effects [91].

Herein, in this thesis we concentrate on azobenezene-containing polymers, also noted as azopolymers, which they represent a materials platform that combines the ease of processing and high optical quality of polymers with the photocontrol provided by the azobenzene units. The potential of photoisomerization induced optical and photomechanical effects has attracted great research interest towards the fundamental properties as well as the practical applicability of azobenzene-containing polymers.

Azobenzene is an aromatic molecule consisting of two phenyl rings connected by a nitrogen double bond, (an azo-linkage, –N=N–), giving rise to strong absorption in the ultraviolet (UV) and visible wavelength. ‘Azobenzenes’, or

simply 'azos' are a class of compounds obtained by substituting the benzene rings with various substitutes. The substitution of an azobenzene-based molecule determines its photochemical behavior, so the azobenzene can be tailored to be responsive in various wavelengths ranging from UV to visible region of the spectrum. Thus, azobenzenes are typically divided into three spectroscopic categories: azobenzene-type molecules, aminoazobenzenes-type molecules and pseudostilbenes [92]. This classification is based on the relative energies of the transition from a non-bonding orbital to an antibonding p-orbital (n, π^*) and from bonding p-orbital to an antibonding p-orbital (π, π^*) transition. Azobenzene-type molecules, which are similar to the unsubstituted azobenzene or only contain non-polar substitutes such as long aliphatic chains, have an intense $\pi \rightarrow \pi^*$ band in the UV region and weak n $\rightarrow \pi^*$ band at ca 400nm. Aminoazobenzenes, which are *ortho*- or *para*-substitutes with an electron-donating group, the $\pi \rightarrow \pi^*$ band is red-shifted to the proximity of the n $\rightarrow \pi^*$ band which is sensitive to substituent effects. Pseudostilbenes, are substituted at the 4 and 4' positions with an electron-donating and an electron-withdrawing group (such as an amino or nitro group). For this so called, *push-pull* molecules, the $\pi \rightarrow \pi^*$ is considered to be of the lowest energy, and the n $\rightarrow \pi^*$ is overshadowed by this intense transition [93]. As a common feature of these types, the conjugated π system gives rise to a strong electronic absorption in the UV and/or visible range of the spectrum, confirmed by the prominent colors of the compounds: yellow, orange and red. The structural differences between the three types of azobenzene are presented in figure 3.1.

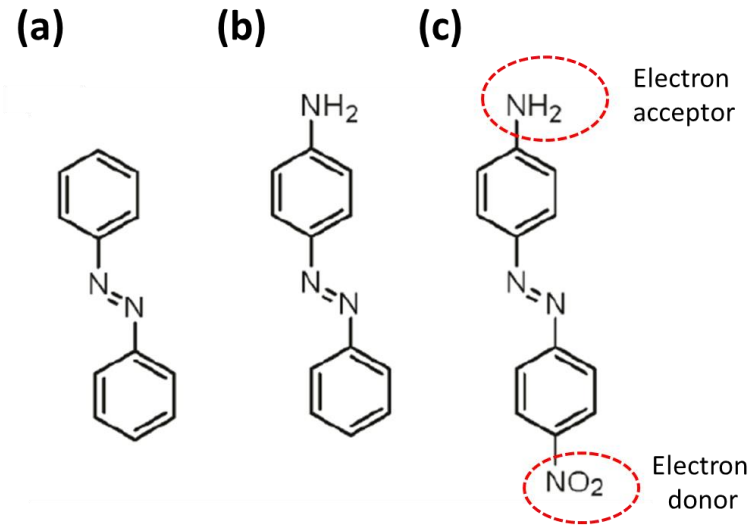

Figure 3.1: Example molecular structures: (a) azobenzene-type, (b) aminoazobenzene-type and (c) pseustilbene-type molecules.

The spectral and photophysics properties of azobenzene are highly sensitive to its substitution pattern, but a common feature to all azobenzene and its derivatives is the fast and reversible photo-isomerization between a *trans-cis* state [94]. Upon photon absorption, the azobenzene molecule crosses an energy barrier of ca. 200 kJ mol^{-1}, within a time scale of picoseconds, to isomerize from a thermally stable *trans*-form to a metastable *cis*-form [95], as illustrated in Figure 3.2. Geometrically, the *cis*-azobenzene is characterized by 90° twisting of the phenyl rings relative to plane of the azo bond [96], and 44 % reduction in the distance between the 4 and 4' positions (from ca.1 nm to ca. 0.6 nm) [97]. This conformational change can proceed either via out-of-plane rotation or in-plane inversion around the N=N double bond, of which the latter is favored due to smaller free volume needed. The reverse reaction back to the stable *trans*-form occurs via thermal relaxation or illumination with light within the absorption range of the *cis*-isomer [98].

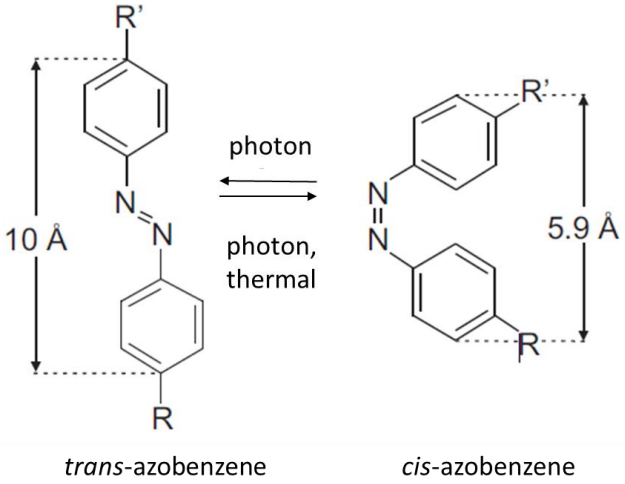

Figure 3.2: *Trans-cis* isomerization of azobenzene triggered by UV/vis or thermal relaxation.

The rate of thermal reconversion strongly depends on the substitution pattern of the azobenzene, typical lifetime for azobenzene-type molecules, aminoazobenzenes, and pseudostilbenes are respectively, on the order of hours, minutes and seconds. In a photostationary state, the ratio of chromophores in *cis* and *trans* states is constant. In this condition it is dependent on the quantum yields of the two isomerization processes as well as on the thermal relaxation rate, because it is highly sensitive to the local environment and the irradiation conditions and it strongly dependent on the irradiation wavelength [99]. For the unsubstituted

azobenzene the fraction of cis-isomers is 91% when irradiated with 365 nm and 12% if irradiated with 405 nm [100]. When the illumination is terminated, the metastable cis-form tends to thermally relax to the stable trans-form with a time constant determined by the chemical structure and local environment of the molecule. Among azobenzenes, the pseudostilbene-types are of particular interest because they have both donor and acceptor substitutes, which leads to overlapping of the absorption spectra of *trans* and *cis* state at blue-green wavelengths [101,102]. Therefore, a single wavelength of illuminating light can drive both isomerization directions leading to continuous cycling between the two isomeric states *trans-cis-trans*, that is needed for many photoinduced effects such as photo-orientation and photo-induced mass migration phenomenon. For this reason, the main azobenzene chromophores utilized in this thesis, belong to the pseudostilbene category.

3.1 Photo-induced motions and movements

Under light irradiation, the molecular movements of azobenzenes induce the multi-level motions in the polymer. In this framework, the motions triggered by the photoisomerization process can be classified into three types [41], by their characteristics length scales: (1) molecular-scale motions, (2) domain-scale motions and (3) macroscopic motions. This division is oversimplified, since motions on different size-scales are always concurrent and inter-dependent, see Figure 3.3.

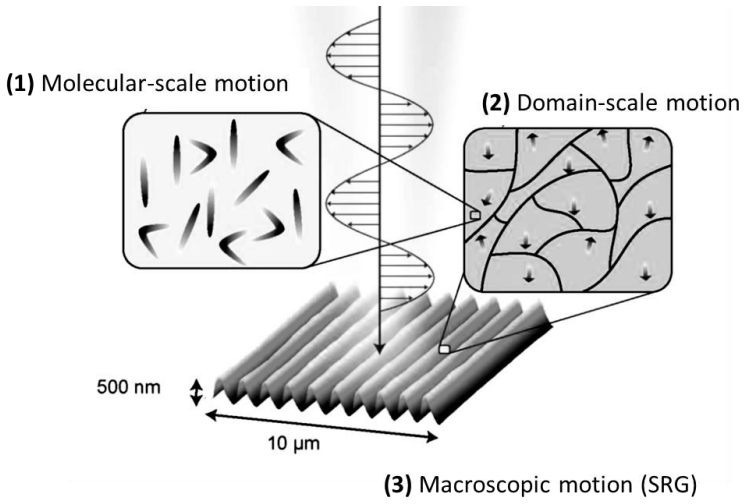

Figure 3.3: Levels of light-induced motions in azobenzene-containing materials.

The basic molecular-level process is the *trans–cis* photoisomerization reaction itself, leading the photo-induced orientation of randomly oriented chromophores within the polymer matrix [103]. A linearly polarized light of appropriate wavelength activates only the chromophores with dipole moment parallel to the axis of light polarization, in such a way that the azobenzene molecules statistically reorient and accumulate to the direction perpendicular to the polarization plane [104]. The concentration of the chromophores aligned perpendicular to the light polarization gradually increases under illumination with polarized light, until a saturation level is achieved. This selectivity originates from the highly anisotropic structure of *trans*-azobenzene, and finally leads to anisotropic alignment of the chromophores and birefringence in the material. The resulting molecular alignment can be erased by irradiating the sample with circular polarized or unpolarized light [41]. Pseudo-stilbene-type azobenzenes is the best molecule for inducing photo-induced orientation because of their fast isomerization process. Aminoazobenzenes are good candidates for the motion, but "normal" azobenzenes shows little photoinduced orientation due to their slow back isomerization process [105].

The domain-level motion, which occurs roughly on the nanometer scale, concerns an interaction between the azobenzene molecules and the matrix material [41]. The process is amplified through collaborative motions that arise from some level of intrinsic order within the polymer system, e.g in the form of liquid-crystalline, semi crystalline, Langmuir-Brodgett or monolayer film. The azobenzenes show photo-isomerization and alignment even in the constrained matrix and thus whole liquid crystals or crystal's domains reorient to a direction perpendicular to the light polarization [106]. In such systems, photoisomerization drives reorientation of whole liquid crystalline or crystalline domains, resulting in a high degree of overall orientation, much higher than in amorphous polymers. This phenomenon is called ‘co-operative motion and these kinds of "domain" motions are ranging from the nanometer to submicron level. For inducing these motions, any types of azobenzenes are useful.

The third type of motions occurs at a macroscopic scale and it is able to produce structural changes in the total volume of the material that is visible to the naked eyes. For this kind of motion, it also requires that the azobenzene should be connected to polymers. The most studied and also complicated type of macroscopic motion is the light-induced surface patterning [105]. When a thin film of an azopolymer is exposed to a simple interference pattern of two laser beams with spatial variations of intensity and/or polarization, the photoisomerization of azobenzene invokes mass migration of the material from the illuminated to the dark

areas, forming high-modulation-depth-sinuosidal periodic surface-relief grating (SRG) [106]. The SRG formation was first observed in 1995 by the Natashon/Rochon [107] and Tripathy/Kumar [108] research team. However, the mass transport is supported only by the spatial intensity and/or polarization variation of the incident light, so arbitrary structures could be inscribed as well. The phenomenon occurs well below the glass transition temperature (T_g) of the amorphous material, and allows formation of surface-relief grating structures (SRG) with modulation depths in a range of several hundreds of nanometers and grating periodicities larger than the irradiation wavelength [109]. This motion has been considered to be a photo-driven mass transport effect because total volume of the polymer is almost the same after irradiation, which is quite different from other conventional microscopic surface processing. The driving mechanism behind the light-induced mass transport is still debated, although it is commonly acknowledged to originate from fast cycling between *trans* and *cis* azobenzene isomers and the subsequent modifications in the local environment of the chromophore [110].

3.2 Light-induced shape manipulation

One of the most remarkable light-induced effects caused by azobenzene photoisomerization is the capability of directional micron-scale mass transport of the bulk materials. This thesis is focused in the light-manipulation of an azopolymeric pre-fabricated structures, by exploiting the 'athermal photofluidization' phenomenon, which means a photo-softening of the material. Starting from a pre-structured material, which is initially solid, upon irradiation with linearly polarized light of appropriate wavelength, it becomes 'fluid', without any significant variation of temperature, leading to a directional deformation of the azopolymer according to the polarization direction, probably due to the reversible *trans-cis-trans-* photoisomerization. Such photo-motion seems to allow azo-materials to fluidize even under glass transition temperature (T_g) by light irradiation [99]. This extraordinary fluidic behavior of azopolymers has been a long-lasting problem in solid state physics; to date, several models have been suggested in order to disclose such mysterious and interesting phenomena, particularly in terms of SRGs generation (far-field irradiation): (i) thermal model [111]; (ii) pressure gradient force model [112]; (iii) mean-field model [113]; (iv) optical field gradient force model [114] ; and (v) asymmetric diffusion model [114] (the work by Labarthet provides all aspects of the proposed mechanism in terms of molecular

orientation) [115]. Despite such theoretical efforts, none is suitable for all photofluidic phenomena at first. Furthermore, thorough understanding on how the polymer structure affect the surface patterning efficiency has not been reached. Anyway, important parameters include molecular weight and the glass transition temperature of the polymer, as well as the azobenzene content of the material are known. The effect of chromophore concentration is particularly interesting as it can help to gain fundamental understanding on how much power the azobenzene isomerization reaction can actually translate into large macroscopic movements. Here, we show that adopting azopolymer and using light to control its fluidic-like behavior, allows to achieve a new degree of control in designing 2D and 3D complex soft-matter architectures. Nowadays, a large number of processing technologies are available for fabricating complex polymeric architectures which are mostly static in nature, therefore they cannot be morphologically modified once fabricated [1]. So, by employing stimulus sensitive materials we are able to overcame such a limitation. In this framework, by employing azopolymers, we perform an *in situ* active and dynamically manipulation of a structure, just by using light with an appropriate wavelength and polarization state.

In the present work, we exploit the light-induced mass migration phenomenon in a 2D lattices for deterministic manipulation in terms of reshaping of microstructures by using directional "superficial" photofluidization of azobenzene materials. As a proof of its principle, we start with different pristine structures (regular array of micro-pillars with different dimensions and periods, and micro-wells) and reshape them by applying a uniform polarized illumination.

3.2.1 Azopolymers Micro- Structured Surfaces

The micro-pillar array (azobenzene-based polymer) is fabricated on a glass substrate by soft lithography technique [116]. The technique can be divided into three steps: preparation of a silicon wafer master, fabrication of an elastomeric stamp from the master and imprinting of a micro-structured surface using the stamp.

The silicon wafer master is fabricated by optical lithography using a Cr mask prepared directly by using a laser writer. Geometry of the master is designed in AutoCAD software and consists of four square regions (size of each region is 2.5 x 2.5 mm) with a regular pillar structure. Each region has defined sizes of the pillars and periods (λ), see Figure 3.4. The four pillar regions on the silicon wafer have λ of 5, 7, 9 and 11 μm and diameter of each pillar is half of this length.

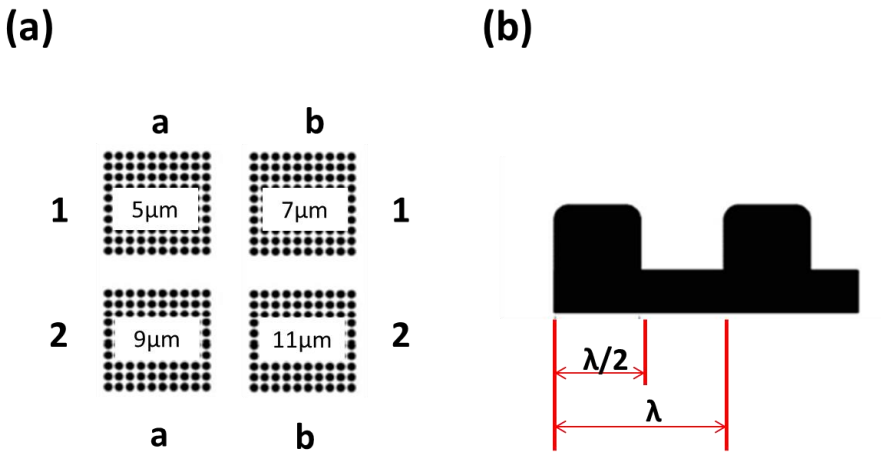

Figure 3.4: Scheme of four arrays of the pillars on the silicon wafer mask with varying the period (λ) and the diameter of pillar in each region is half of λ. (a) top view; (b) lateral view.

As regards the micro-well structures, instead of a Si wafer, we use a film mold (FleFimo provided by Soken Chemical & Engineering Co., Ltd.) as master.

The silicon master and the FleFimo mold are used in the preparation of an elastomeric stamp from polydimethylsiloxane (PDMS). The PDMS stamp is prepared from Sylgar 184 kit (Dow Chemicals) by mixing the base with the curing agent at a 10:1 (v/v) ratio. 5 mm thick layer of the PDMS mixture is poured onto the mold and cured for 2 hours in oven at 60°C. After curing the PDMS stamp is peeled from the master, rinsed with ethanol and dried by blowing nitrogen to clean its surface.

The protocol developed in the preparation of the structures is the following. A certain amount of azopolymer solution (varying from 5 to 10 µm) is casted on a clean glass cover slip in a form of a droplet, which is covered with the PDMS stamp. The system (coverslip-azopolymer drop-PDMS stamp) is positioned on a hot plate (55°C) for 2 hours to let the evaporation of the proper solvent in which the azo is dissolved. Then the PDMS stamp is carefully removed from the glass cover slip, leaving the azopolymer film patterned. The obtained micro-pillar structure are checked under optical microscope in order to verify the quality of the imprinting process and possible irregularities of the imprinted micro-pillar pattern or unwanted artifacts. After each use, the PDMS stamp is washed in ethanol and placed for 20

min into ultrasound bath to remove eventual traces of attached azopolymer solution from its surface. Each stamp is used 3 to 10 times to prepare the structured surfaces, based on its condition.

In the present experimental study, two different azopolymers are employed and investiagated: a commercial azo-polyelectrolyte poly{1-4(4-(3-carboxy-4-hydroxyphenylazo)benzene sulfonamide)-1,2-ethanediyl sodium salt} named as PAZO and the speudostilbene side chain polymer, poly(Dispersed Red 1 Methacrylate) (pDR1M).

PAZO is a highly light-responsive material showing efficient SRG formation upon visible irradiation during short illumination time [19,18], amd it presents the maximum absorption at around 360 nm. The most significant disadvantage, is the water solubility of PAZO, which makes it unsuitable for bio applications and experiments in water environment. In order to overcome such a limitation, in a previous work we proposed a PAZO thin films coated with a protective polyacrylic acid layer (PPAA) that is plasma-deposited [117]. In this way, the aim is to prevent PAZO dissolution in aqueous environments whilst maintaining its effective mass-migration capabilities.

To low the solubility of the PAZO and to improve the hardening of the material under irradiation, without affect the photofluidization, another strategy is adopted. We employ in the experiments a passive material, poly(methyl methacrylate) (PMMA), simply added to the azo in order to obtain a well-homogenous blend.

More specifically, we use a mixture of commercially available PAZO (Figure 3.5a) and poly-(methyl methacrylate) (PMMA) (Figure 3.5b), (both from Sigma-Aldrich), prepared as follows. A certain amount of PMMA with molecular weight (Mw) of ~15000 g/mol, is dissolved in N,N-Dimethylformamide (DMF) at a concentration of 4 wt%. PAZO (Mw ≈ 369,33 g/mol) is dissolved in methanol at concentration of 25 mg/mL. 10 repeat units of PAZO solution are mixed to one unit of PMMA solution. Then, the blend is mechanically stirred for 30 minutes and then sonicated for one hour until a homogeneous dark yellow/orange mixture is formed.

Poly(Dispersed Red 1 methacrylate) (pDR1M) is an hydrophobic azopolymer (Sigma Aldrich) (Figure 3.5c), and it could be dissolved in different non-polar solvents, depending on the purpose, e.g tetrahydrofuran (anhydrous, ≥ 99.9%, Sigma Aldrich) (THF), toluene (TO) and N,N-Dimethylformamide (DMF), keep maintaining the same concentration at a 2 wt.%. The UV-Vis spectra in Figure

3.5d reveals the relative absorption peak of PAZO+PMMA around 380 nm and of pDR1M at 467 nm.

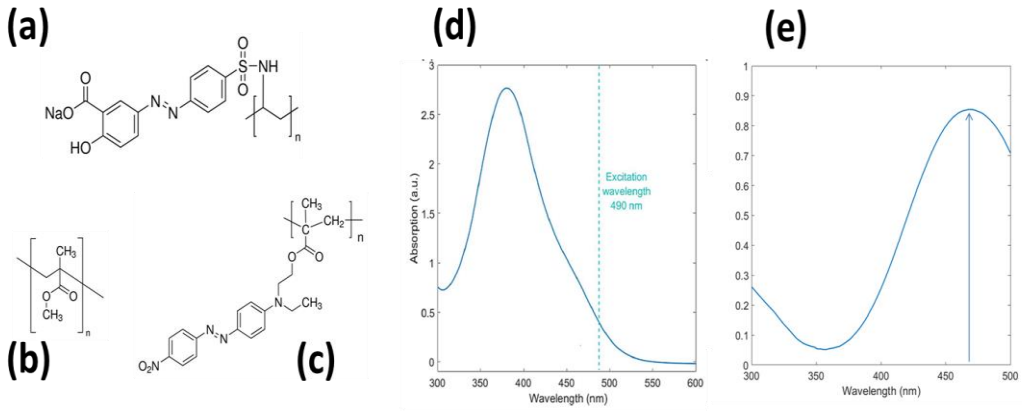

Figure 3.5: Chemical structure of: (a) PAZO; (b) PMMA; (c) pDR1M and corresponding optical absorption spectrum: (d) PAZO+PMMA blend and (e) pDR1M.

The micro-pillar and pore topographies on the glass cover slips are analyzed with scanning electron microscopy (SEM) and atomic force microscopy (AFM) to check the fidelity of the imprinted structures, see Figure 3.6. An array of well-defined azo-polymeric micro-pillars over large area is then obtained as showed in Figure 3.6a. AFM reveals circular pillars with a D= 3 μm diameter, and h= 1.5 μm height, arranged as a squared lattice with λ= 5 μm periodicity, according to the region a-1 of the silicon master (see Figure 3.4).

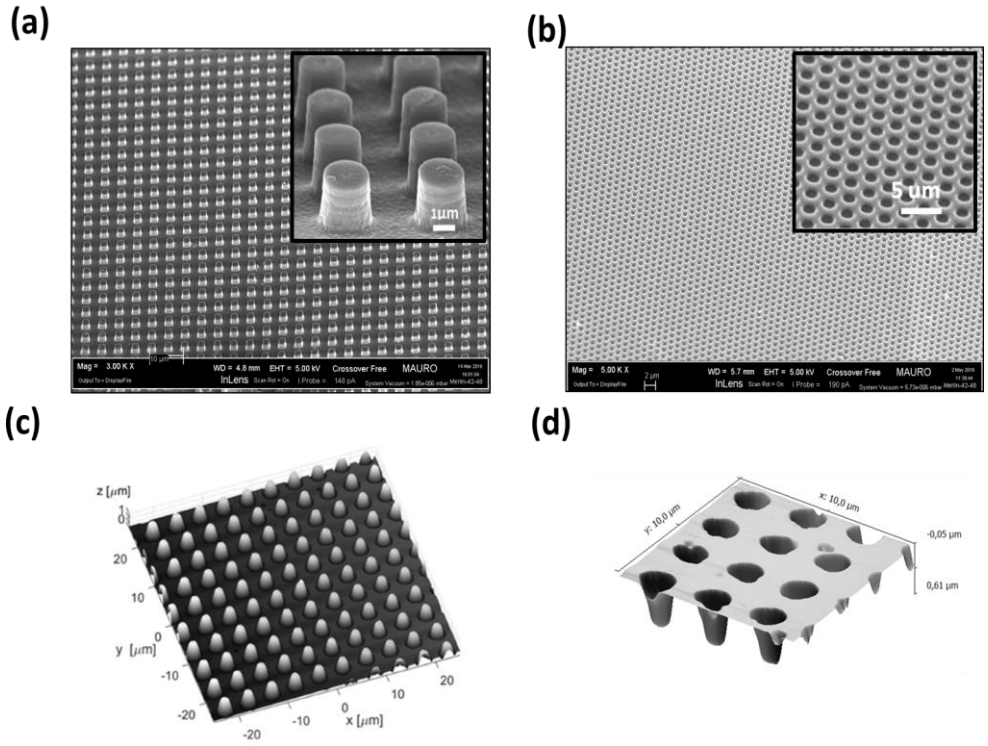

Figure 3.6: SEM images and corresponding 3D representation of AFM topography map of as-fabricated (a,c) micro-pillars, (b,d) micro-wells by soft imprinting.

The micro-wells exhibit a round shape, diameter D = 1µm and a period of 3 µm and the depth of the well is about 0,55 µm.

3.2.2 Directional mass migration

The effect of linearly polarized light on the azopolymeric structures is firstly investigated and discussed in ***Publication II***. In agreement with previous experimental finding and results from literature [118], we expect a directional mass migration of the material along the polarization direction. In order to study in details this phenomenon, for triggering and monitoring the surface modification, we employ an experimental setup, build up in our laboratory [119], see Figure 3.7.

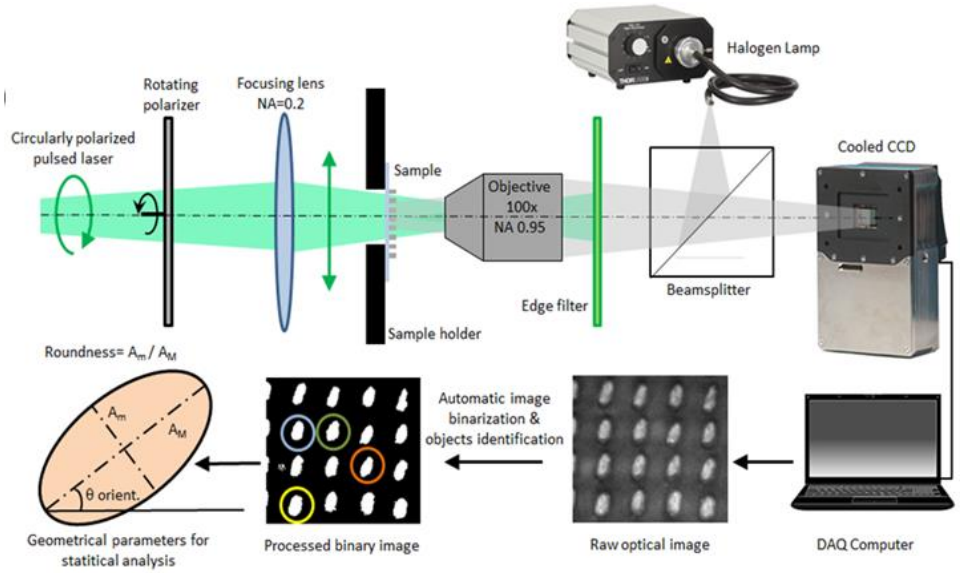

Figure 3.7: Sketch of the optical setup, the data acquisition and the processing flow [119].

A pulsed laser beam (10 ps pulse duration, wavelength λ = 490 nm, laser intensity 1kW/cm^2) circularly polarized is used to irradiate the sample. The beam can be eventually filtered by a linear polarizer placed on a rotational stage to obtain the linearly polarized light along arbitrary directions. During laser irradiation, a white-light wide-field imaging system (reflection) is employed to real-time monitor a homogeneous circular area of roughly 250 μm diameter. A 100x objective (NA=0.95) coupled with a tube lens allows to image the sample surface on CCD camera. The laser beam is filtered out by an edge filter (FEL550 from Thorlabs) along the imaging arm. Upon optical image collection and analysis (by employing an ImageJ tool), some geometrical parameters, including the major axis A_M, the minor axis A_m and the orientation θ of the pillars, where θ is the angle between the major axis and a horizontal axis, are extracted for all individual objects within each image. In addition, mean values are calculated in order to add significance and robustness to the overall description of the collective shape modification involving a plurality of pillars.

We consider the azopolymeric blend, consisting of PAZO-PMMA, as a typical representative for this study of this class of light-sensitive azobenzene materials.

The laser beam is slightly focused in such a way that the spot size on the sample surface is roughly 30-micro-pillars, thus resulting in a density of power of 1.6 kW/cm^2, see Figure 3.8a We point out that the pulsed laser has been employed because of its tunable frequency, that allows for a better matching with the absorption band of PAZO (see figure 3.5d). Due to the slow thermal relaxation time of the isomerization transition (typically in the range of hundreds of ms) as compared to the repetition rate of the pulsed laser (80 MHz), it seems reasonable to approximate the pulsed radiation to a CW light.

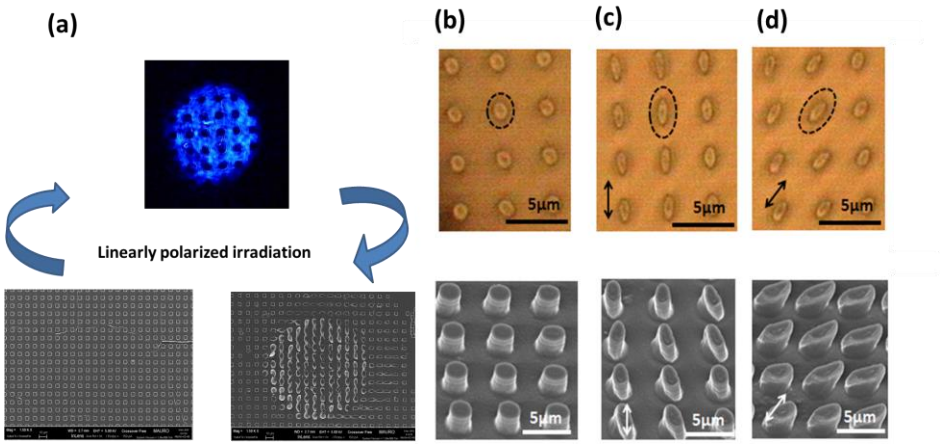

Figure 3.8: White light and SEM images of (a) the illuminating beam and the light-guided deformation of cylindrical-shape pattern. Various deformation orientation obtained by exposing the sample at different angle of incidence (b) no irradiation, (b) $\Theta = 0°$, (c) $\Theta = 45°$.

The laser polarization can be changed by use a powered waveplate, while the laser intensity is constant at 1 mW, in order to obtain a homogenous deformated area. Upon linearly polarization, the pillars became elongated according to the polarization direction, as clearly visible from Figure 3.8b-d. This effect is mainly due to the preferential direction in the glassy azo-polymer material displacement, parallel to the light polarization, while the long-axis of azobenzene molecules is found to be aligned in a direction perpendicular to the light polarization in accordance to previous studies on photofluidization [120]. The structures in the Figure 3.8 are obtained by exposing the sample to the expanded laser beam for 1 min at different angle of incidence. In a micro-wells structure, Figure 3.9a, the directional mass migration of the material (red circle and arrows corresponding to the polarization direction), induces a closure of the pores into narrow slits

perpendicular to the polarization plane (yellow arrow in Figure 3.9c), due to the fluidization of the material in the parallel direction. In figure 3.9d, diverse deformation steps are performed by keeping the irradiation for different time intervals.

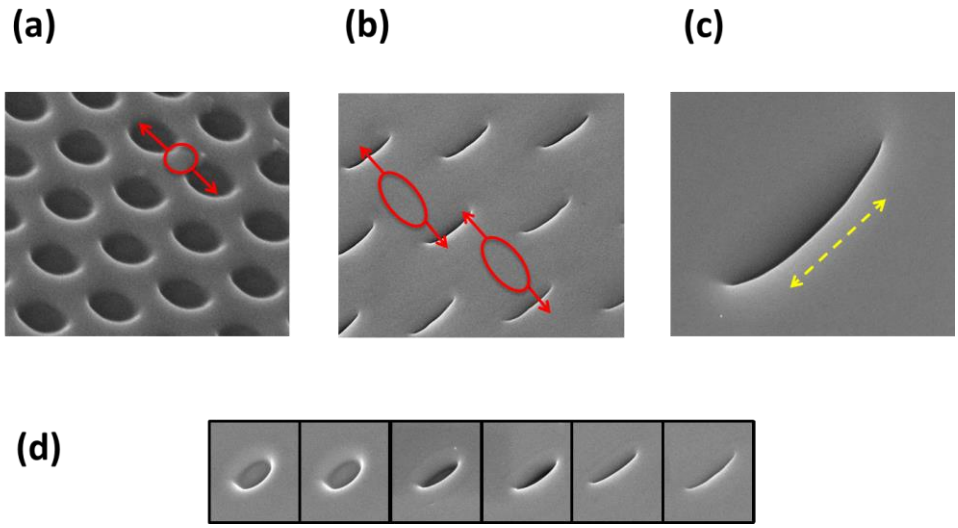

Figure 3.9: SEM images at 45 deg of micro-well (a) before and (b) after irradiation with lineary polarization at $\Theta = 45°$ (red arrows: direction of the mass migration of the material), (c) single hole manipulated (yellow line indicates the direction of pore closing), (d) time-evolution of micro-wells deformation.

By playing with the polarization state (Figure 3.10 a,b), with the angle of incidence of the laser beam (Figure 3.10c) and irradiation time (Figure 3.10d), interesting structures can be obtained in a single-step of irradiation, overcoming the typical limits founded in the traditional lithographic fabrication techniques. Exploiting this phenomenon, some fabrication issues or defects can be settle up and even exotic and fancy architectures can be obtained.

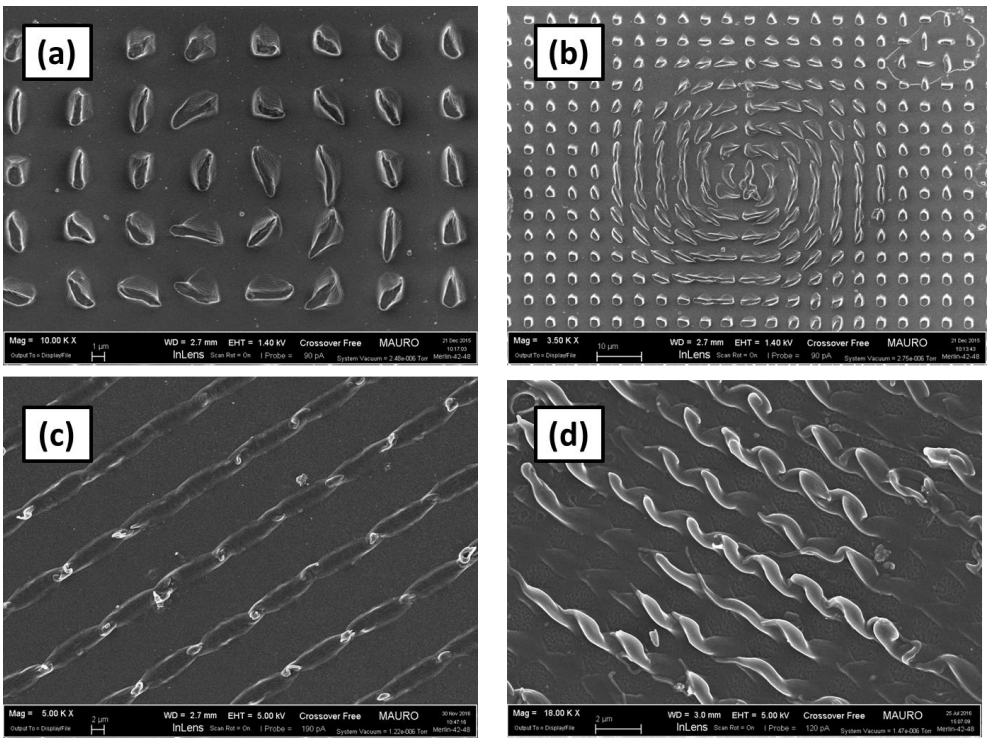

Figure 3.10: Structure manipulation obtained by using (a,b) azimuthal polarization, (b) angle of incidence of 45°, (d) with a prolonged irradiation time.

Interesting to note here, that in figure 3.10d, starting from an array of individual pillars, by means of a prolonged irradiation (t > 3 min), twisted linear grating can be obtained. The ability to tune the morphological features of a simple structures into complex architectures has attracted significant interest in many application field, especially in biology for cell conditioning, which is well described in Chapter 5.

3.2.3 Light-triggered restoring structures

In this section, we explore the effect of polarized light irradiation, in such a way that the anisotropic photofluidic movements of azomaterials is exploited in the post modification of arbitrary microstructures. We demonstrate that an azopolymeric film prepatterned by soft-lithography, can be anisotropically deformed and consequent restored in its initial shape via single irradiation just by controlling the polarization state of the incident laser beam. Figure 3.11 shows a typical result from this findings, which was previously discussed in ***Publication III***.

PAZO-PMMA is transferred as a squared lattice of circular pillars over large area (Figure 3.11a), which upon linearly polarized irradiation they become strongly elongated (Figure 3.11b), as describe in the chapter before. A rotation of the polarization by 90 degree respect to the previous irradiation, triggers a retraction of the elongated pillars. Despite some detrimental effects on the morphology quality, a substantially circular cross section is restored by triggering a laser-induced stretching along the minor axis of the elongated pillars (Figure 3.11c).

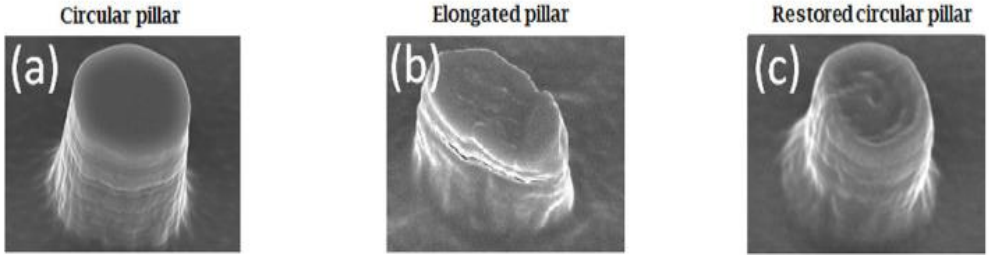

Figure 3.11: SEM pictures of individual pillars: (a) as-fabricated circular pillar, (b) after a single laser exposure with linear polarization, (c) restoration after two laser exposures with orthogonal polarizations [119].

The reversible elongation process can be performed over several times, showing just a slow progressive degradation of the structures after 3-4 cycles. To add significance and robustness to the analysis, we perform a quantitative investigation, as shown in Figure 3.12a. The mean roundness is evaluated time by time as the average of the ratio Am(t)/AM(t) over 20 micro-pillars included in the optical images that are collected, binarized and analyzed as described above (Chapter 3.2.2). We observe that elongation-restoration cycles can be repeated upon irradiation with the very same laser power, by simply rotating the incident polarization by 90 degrees, from a vertical to a horizontal orientation and vice-versa [119]. In Fig. 3.12b–f, exemplary binarized images are shown corresponding to relevant times during the light-induced modification of the pillars. In time cycles lasting about 400 s, almost circular pillars, mean roundness about 0.9, are elongated along the vertical direction (mean roundness down to 0.6, as estimated from Figure 3.12 c,e) and then restored back to a circular shape (Figure 3.12d,f).

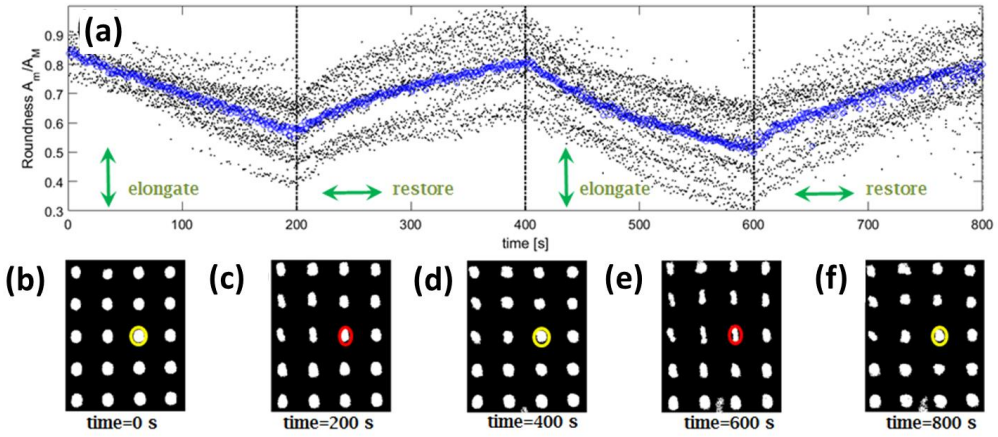

Figure 3.12 : Pillar reversible elongation. (a) time-resolved roundness values for pillars during laser irradiation with time-varying polarization states (black dots: roundness of individual pillars, blue circles: mean value over pillars in each frame); (b–f) binarized optical images of micro-pillars at relevant times during pillar light modification.

This reversible pillar modification is advantageously promoted by the presence of a stabilizing PMMA component which improves stiffness of the polymeric mixture, as suggested elsewhere in other co-polymer matrices containing azobenzenes [121]. In this way, the mass migration triggered by photofluidization is prevented to flow outside the pillar volume even without external constraints [118]. Interesting to note here, that illuminated PAZO-only micro-pillars are prone to quickly lose their regular shape because of the strong mass diffusion away from the volume initially occupied in their as-fabricated state. The elongation-restoration mechanism can be hardly repeatable over many cycles, as demonstrated by the time-dependent mean roundness plot shown in Figure 3.13a. In fact, when several elongation-restoration steps are performed in sequence, the PAZO pillars get completely melted and the pillar cross section cannot be optically recognized anymore [119]. For comparison purposes, SEM pictures of PAZO-PMMA and all-PAZO pillars after an overall irradiation time of 400 s are shown in Figure 3.13b,c. The softening of PAZO pillars due to the athermal photofluidization hampers the full recovery of a regular pillar shape because of the progressive leakage of polymer out of the initial confined volume.

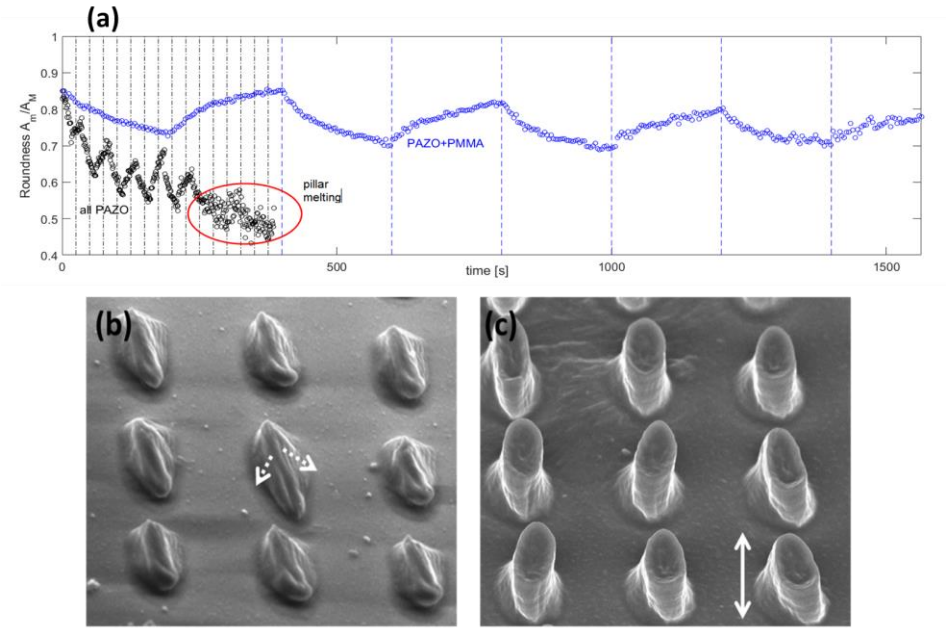

Figure 3.13: (a) Time-resolved mean roundness values for pillars during laser irradiation with time-varying polarization states; SEM picture of (b) all-PAZO and (c) PAZO-PMMA pillars after exposure.

The stretching/shrinking effect described above can be extended for longer time periods. In such a case, a new deformation of the micro-pillars can occur, eventually along a different orientation as determined by the illumination polarization. Figure 3.14a,b illustrates the time-evolution of the mean roundness and the mean orientation angle θ (t) calculated over 30 micro-pillars exposed to a laser beam sequentially switching between two orthogonal linear polarizations. During the first 100 s, as-fabricated circular micro-pillars (Figure 3.14c) are illuminated with an H-polarized beam such that a horizontal elongation is produced, corresponding to a mean roundness of about 0.7 (estimated from Figure 3.14d). When the polarization is rotated by 90 degrees (V-polarization), the initial circular shape is restored (mean roundness 0.9) in 130 s irradiation (estimated from Figure 3.14e). However, if the V-polarized illumination is kept for additional time, the mean roundness parameter starts to decrease again, the elongation occurring along a different direction. In fact, from 100 s to 400 s, the mean orientation angle θ experiences a rather quick change from 0 degrees (horizontally oriented micro-pillars) to nearly − 70 degrees (almost vertically oriented micro-pillars). After 700 s, the micro-pillars are well elongated (roundness 0.5) and flipped as shown in Fig. 3.14f.

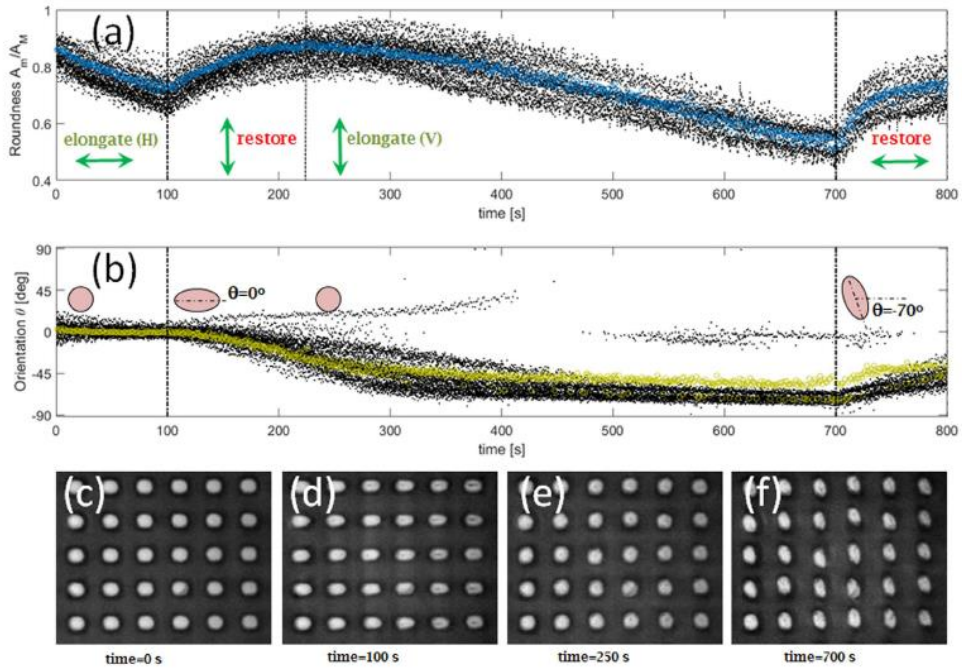

Figure 3.14: Pillar flipping. (a) Time-resolved roundness values (black dots: roundness of individual pillars, blue circles: mean value per frame) and (b) time-resolved orientations (black dots: orientation of individual pillars, green squares: mean value per frame) for pillars during laser irradiation with time-varying polarization states; (c–f) optical images of micro-pillars at relevant times during pillar light-modification [119].

Afterwards, upon a further switch to H-polarization, a restoring force is triggered, such that the roundness parameter starts to increase again. Worth to note here that the maximum orientation change we could induce on already elongated pillars with a given orientation has been generally limited to angles smaller than 90 degrees only. In the specific case illustrated in Figure 3.14, after the first horizontal elongation, pillars are hampered to fully orient in a vertical direction, despite a vertically oriented polarization has been used for illumination. As an explanation, we speculate that some degree of polarization-induced irreversible plasticity within the PAZO-PMMA matrix might occur during the very first exposure. In alternative, a phase separation between PMMA and PAZO due to the light-induced diffusion might constrain the mass-migration mobility. By rotating the polarization of the incident laser by angular steps smaller than 90 degrees, it is possible to induce micro-pillars to smoothly orient accordingly, while still keeping a given elongation. Therefore, there is a reorientation of the ellipsoidal pillars whose major axis rotates parallel to the driving electric field. For example, in Figure 3.15a, elongated pillars

are observed to maintain a roughly constant (mean) roundness value during a 400 s illumination wherein the polarization is rotated by 45 degrees each 100 s (green arrows in the figure).

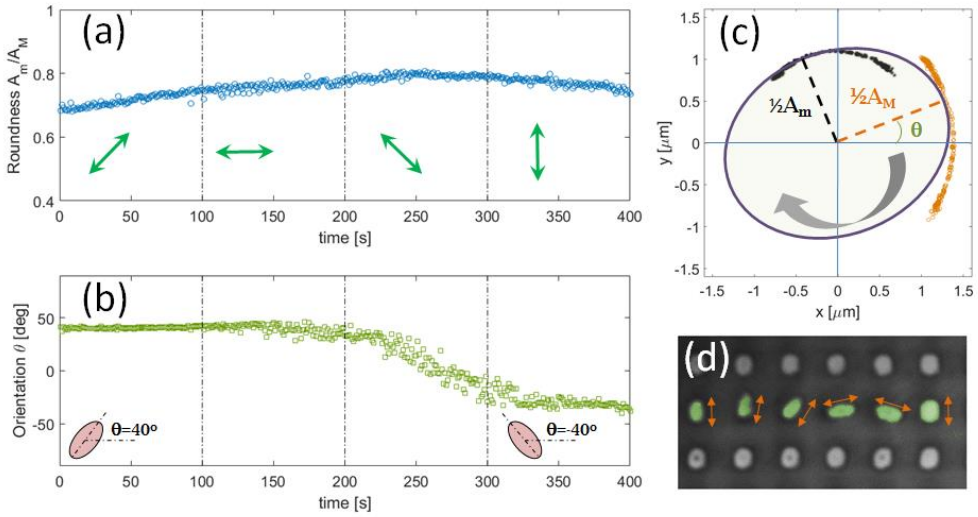

Figure 3.15: Pillar rotation. (a) Time-resolved almost constant roundness and (b) time-resolved orientation (mean value per frame) for pillars during laser irradiation with time-varying polarization states; (c) rotational trajectory traced by the minor (black asterisks) and the major (orange circles) axis of an equivalent "average ellipse" (blue lineprofile) during clockwise rotation; (d) optical image of individually modified pillars (in green) with varying orientation as indicated by the orange arrows [119].

In this case, light-induced deformations are provided such that an overall rotation of the elongated pillars directly occurs without an intermediate restore of the initial circular shape. As shown in Figure 3.15b, the mean orientation angle suggests that pillars are substantially experiencing a smooth rotation of about 80 degrees according to the instantaneous polarization direction (with some delay due to the viscosity of the polymer). In order to better illustrate this effect, starting from the estimated mean values for Am(t), AM(t) and θ (t) in each time frame, the trajectories defined by the ray vectors associated to the pillar minor axis and major axis are traced on an xy-plane that ideally contains the pillar top surface (black circles for the minor axis and orange circles for the major axis in Figure 3.15c). As a result, a 'mean' elliptical pillar can be drawn having a minor axis and a major axis oriented according to the instantaneous value of θ (t). Such a graphical representation of the 'mean' elliptical pillar in time provides an intuitive description

of the substantially rigid rotation experienced during the polarization changes. The fine control on the elongation and orientation of PAZO-PMMA structures demonstrated above can also allow a tuning of the surface pattern on an individual-pillar basis. In fact, if illumination is provided as a localized light spot (e.g. by means of a focusing system), micro-pillars can be sequentially modified according to the desired polarization state. In Figure 3.15d, a SEM image of several pillars sequentially elongated in different directions is illustrated.

The reconfiguration in its pristine shape, has been also performed in the azo-polymeric micro-wells. Part of the work described in this section has been previously published in International Journal of Polymer Science, 2017 (***Publication VI***) [122] The micro-wells, initially showing circular shape (figure 3.16a), turn into almost closed slits after about 220 seconds of irradiation (figure 3.16b). Subsequently, by rotation of the polarization by 90° observe a gradual restore of the circular shape is visible (figure 3.16c). The image analysis reveals that an average roundness of about 1 is achieved after further 200 seconds of irradiation. In figure 37d we plotted the average area of the holes versus time of irradiation. The graph shows that upon irradiation the hole area is actually reduced till a compete closure of the holes (marked by the black dashed line in the graph). Experimentally we find that the polarization rotation by 90° triggers a recovery of the micro-wells area. After probing the effect of linearly polarization on the hole shape, we aim at exploiting circularly polarized light to reduce the pore size eventually until complete closing. Figure 3.16e shows the effect of circularly polarized light on an array of micro-wells. The graph indicates that irradiation with circular polarization does not affect the roundness of the micro-structures, that is kept constant around a mean value of 0.8. The inset in the graph shows optical images of a sequence of micro-wells individually addressed and irradiated with different doses (the position along the timeline corresponds to the irradiation time). The sequence shows that, although the roundness is preserved, the holes tend to isotropically reduce their size until complete closure.

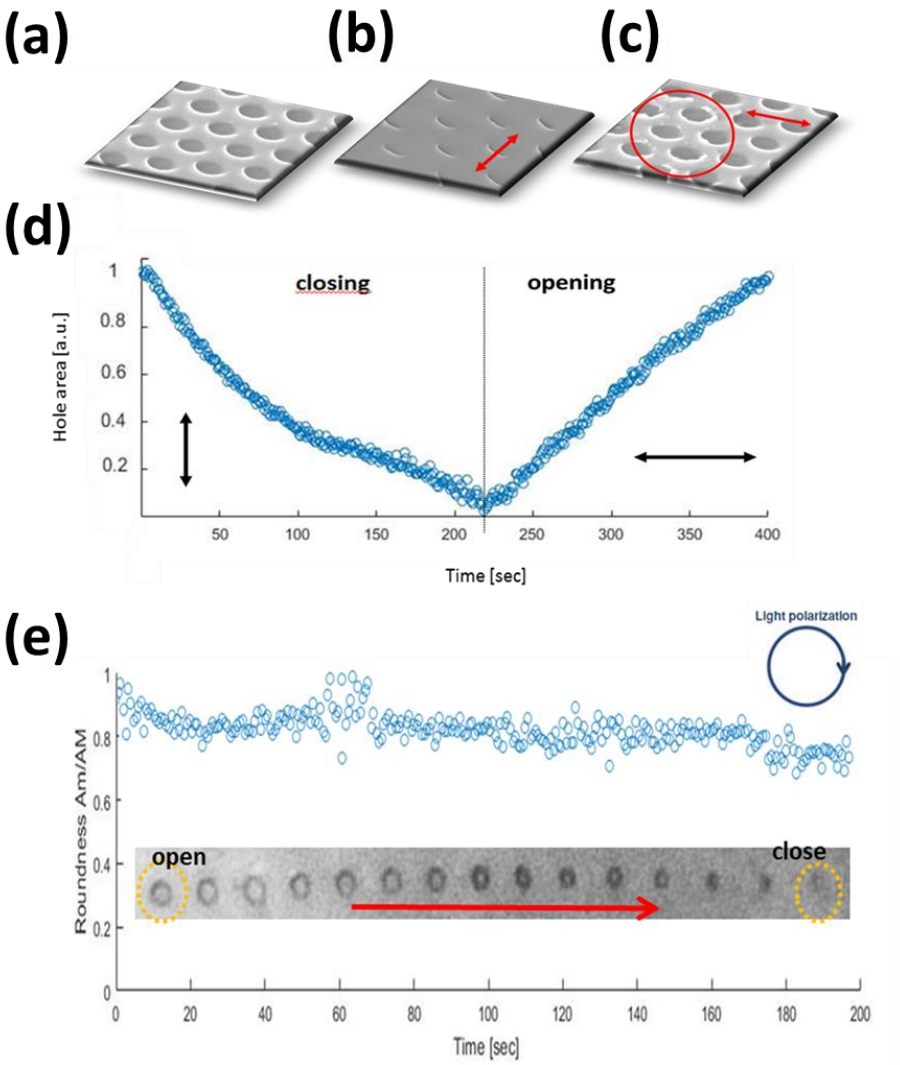

Figure 3.16: Photo reconfigurationof pristine micro-wells arrays by using linearly polarized light: (a) original concavity shape, (b) closed slits, (c) restored shape. (d) Time-resolved hole area values for pores during laser irradiation with time-varying polarization states and (e) time resolved roundness evolution micro-wells during laser irradiation with circularly polarized light. In the inset, optical images of individual micro-wells exposed to different light doses.[122]

Micro-structures have been chosen in order to allow a quick and statistically meaningful optical characterization, an analogous mechanical light-responsivity is expected to occur also in nano-sized objects.

3.2.4 Laser irradiation in a water environment

The elongation-restoration process is also performed in a water environment, see Figure 3.17. We clearly observe in the optical images (Figure 3.17a,b, in immersion mode) that upon irradiation the pillars start to dissolve. The laser spot is focused in such a way that a circular area of roughly 15 μm in diameter can be homogeneously illuminated. The interaction of the light with the azopolymer in water leads the pillars to detach, to lose their initial shape and to dissolve.

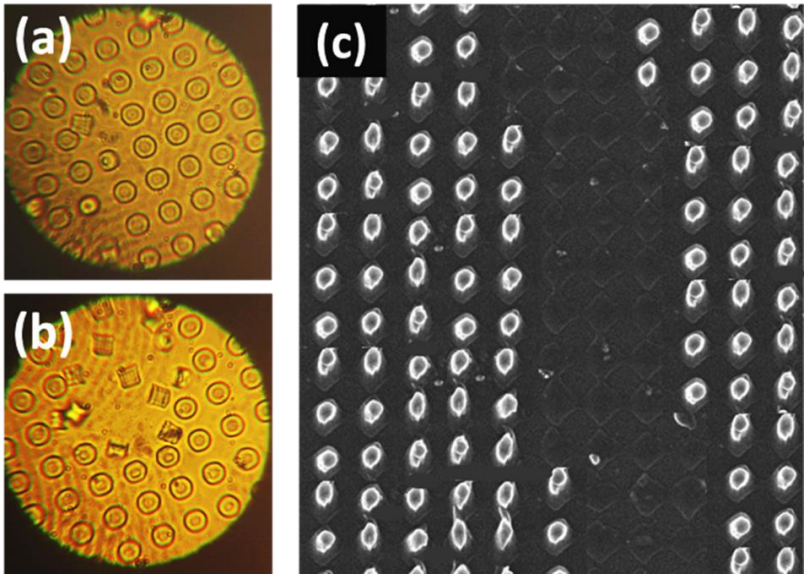

Figure 3.17: White light images at different irradiation step in a water environment (a) irradiation on (first 3 sec); (b) collapse and progressive dissolution of the pillars upon irradiation; (c) resulting SEM image of unidirectional light-solubility of PAZO-PMMA micro-pillars.

Worth to note here, by exploiting the light-induced solubility of the PAZO-PMMA blend, a selective erasure of the structure (Figure 3.17c) is obtained, just by driving the beam spot across the array. This structure modification leads a change in topographical as well as in wetting features.

In order to obtain stable structures upon irradiation even in a liquid environment, Poly(Dispersed Red 1 methacrylate) is employed in the next experimental part. pDR1M is a suitable azopolymer according to our aim, due to its hydrophobic nature. By taking advantage of the laser-induced mass migration, we

demonstrate the possibility to modify even the surface hydrophobicity of a pre-patterned phot-sensitive film surface by exploiting an *in situ* deformation by a single laser exposure (in Chapter 5).

3.3 Light-induced wettability changes

In this framework, the fabrication of complex superficial topographies has acquired a growing remarkable importance. Therefore, surface topography, in addition to the surface chemical properties, is a relevant aspect affecting the wettability of a surface. In the past years many groups proposed studies based on photo-responsive surfaces with tunable wetting properties, focused on the surface chemical properties, by photo-switching between *trans* and *cis* triggered by UV/vis irradiation, leading to a change in the surface hydrophobicity behavior. It is well known that the *trans* isomer has a small dipole moment and a low surface free energy resulting in a higher contact angle with water, while the *cis* form shows a lower contact angle due to its higher dipole moment and surface free energy [123]. Ichimura et al. [124] and Radüge et al. [125] managed to induce light-driven wettability changes of a surface modified with a photoisomerizable azo-monolayer by exploiting a polarity change based on the molecular switching of the azobenzene groups included therein. Other approaches for obtaining photo-responsive surfaces with tunable wetting properties include Langmuir–Blodgett [126], self-assembly [127] and layer by layer method.

Here we focused on the opportunity provided by the dynamic manipulation and reconfiguration of superficial pre-pattern, investigating how a light-driven deformation of arrays of azopolymeric micro-pillars can induce an *in situ* anisotropic and controlled change of wettability. More specifically, micrometer-sized pillars are induced to elongate along the polarization direction of an incident laser radiation, in such a way that a hydrophobic behavior is produced according to the laser polarization direction [128]. The results of this study are discussed in ***Publication IV***.

To this aim, we employ a pseudostilbene-type azopolymer, poly(Dispersed Red 1 Methacrylate) structured in squared 3.5μm x 3.5μm x 1.1μm pillars arranged in two dimensions, with 11 μm periodicity along each orthogonal direction, see Figure 3.18. For triggering and monitoring the structure deformation, we use the same setup described before, except for the laser source. In this case we employed a

continuous laser double frequency Nd:YAG cavity emitting a TEM_{00} beam at 532 nm wavelength, with an output power adjustable to a maximum of 250 mW. This is because of the pDR1M absorption pick which is around 467 nm, so green is the most suitable light to trigger a cyclic *trans-cis-trans* isomerization.

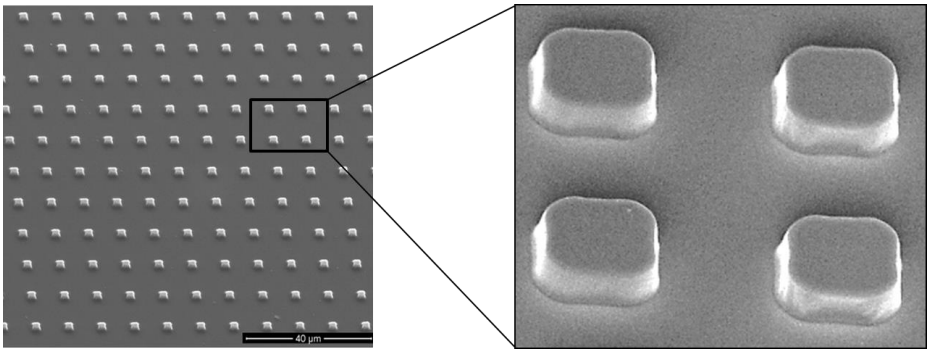

Figure 3.18: illustrative SEM images with inset of squared pDR1M micro-pillars.

All measured performed here, are carry out under the same environmental conditions on four nominally identical samples, which have been laser processed according to the irradiation protocol. Contact angle measurements are performed over the irradiated area of the structure by employing a sessile drop method (Dataphysics OCA-20). A 0.5 µl water droplet is injected onto the sample surface through an automatic syringe. Each contact angle (CA) measurement is repeated by using three different water droplets, and then an average value and an associated square root mean value are calculated. In Figure 3.19 the average CA values as measured onto structured pDR1M samples featuring different pillar cross sections are plotted. More specifically, each data point corresponds to micro-pillars irradiated in a way to exhibit a specific mean roundness parameter ε, as estimated by the automatic image processing system implemented in the setup. The mean roundness parameter (A_m/A_M) is evaluated over 120 micro-pillars. While a pDR1M flat surface is intrinsically hydrophobic because of its chemical structure (CA = 85.2± 62.5µm), such a hydrophobicity is sensibly increased (CA = 97.55 ±61.65 µm) when a textured pDR1M surface is considered, because of a largest effective surface area (data point (a) in Figure 3.19). However, when micro-pillars are deformed along the incident polarization direction, with a roundness ε=0.71, the contact angle is reduced to CA= 79.52± 60.90 µm (data point (b) in Figure 3.19).

Such a CA change occurs anisotropically, along the elongation direction, as detailed in the following. For an 8 s overall irradiation time, micro-pillars further elongate to reach a mean roundness ε=0.51. In this case, a corresponding average CA = 72.25 ±0.9 μm is observed (data point (c) in Figure 3.19). A rotation of the illumination polarization by 90° triggers a reconfiguration of the elliptical pillars resulting in a restoration of the initial shape [119]. Interestingly, the initial hydrophobicity is restored as well, as the contact angle increases back to value CA=89.41±1.5 μm (data point (d) in Figure 3.19).

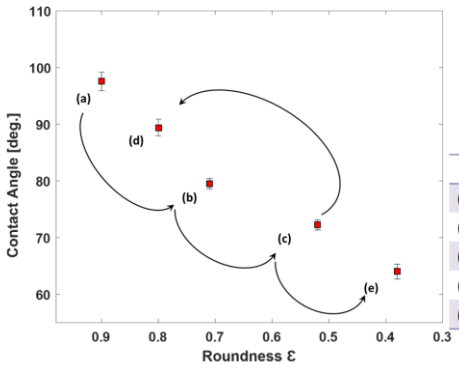

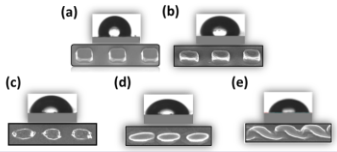

Sample	Water contact angle [deg.]
(a) as-fabricated	97.55 ± 1.65
(b) fisrt step of elongation	79.52 ± 0.90
(c) second step of elongation	72.25± 0.90
(d) reconfiguration	89.41 ± 1.5
(e) irreversible elongation	64 ± 1.3

Figure 3.19: Graph corresponding to mean CA values as a function of roundness of the micro-pillars. Representative water droplet and SEM images of structured pDR1M samples featuring different pillar cross sections.

However, we found this value as systematically slightly smaller than the initial one, probably because of some irreversible degradation effects occurring in the shape restoring process. For each fresh sample, we observed that up to two irradiation cycles can be performed with a good reversibility in morphology and wettability characteristics. The error bar for the CA measurement at point (d) in Figure 3.19 is taking into account variation in the micropillar shape restoring process over two irradiation cycles. For longer irradiation times (larger than 8 s) at a fixed polarization direction, pillars become irreversibly elongated, with mean roundness values ε<0.38, eventually merging together to form twisty linear gratings. As a smaller amount of air is trapped underneath the water droplet, a further decrease of the contact angle is observed, down to CA=64±1.3μm (data point (e) in Figure 3.19). The contact angle measurements presented are taken along a direction parallel to the elongation of micro-pillars. In fact, as the surface structure exhibits an anisotropic topography, the water droplet arrangement on the sample is

anisotropic as well. In Figure 3.20 two water droplets (0.5 µl) left onto either an as-fabricated or an irradiated sample are optically imaged from above. While the two-dimensional symmetry of the as-fabricated micro-pillar array induces the droplet to arrange isotropically (Figure 3.20 (a)), the symmetry breaking due to laser irradiation results in a water droplet significantly spreads along a direction parallel to the micro-pillar elongation (Figure 3.20 (b)).

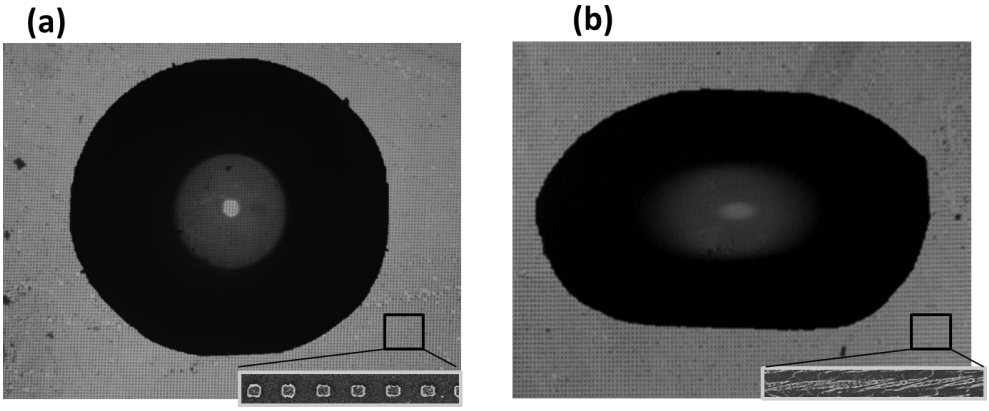

Figure 3.20: Wide-field reflection images of water droplets onto pDR1M micro-pillars with illustrative SEM corresponding to (a) initial squared shape, (b) strongly elongated pillars along the horizontal direction.

In order to understand the experimental observation presented above, an AFM analysis is performed. Here we consider the topography of three illustrative cases, as depicted in Figure 3.21, comprising (1) as-fabricated, (2) slightly elongated, and (3) strongly elongated pillars. We did not perform AFM analysis on reconfigured pillars, because we focused in the study of how a strongly topographic variation of the features can affect the hydrophobicity of the substrate. From AFM maps shown in Figs. 3.21 (a)–4(c), topographic cross-sections along the two orthogonal directions of the square lattices are extracted. In Figures 3.21 (d)–41 (f), V-cross-sections (parallel to the polarization direction) reveal that the inter-pillar distance is significantly decreasing from d=7.5 µm (as-fabricated) to d_1 =2.3 µm (slight elongation), down to d_2 =1.2 µm (strong elongation). Furthermore, perpendicularly to the polarization direction, the inter-pillar distance is maintained at a rather similar value to the as-fabricated sample ($d_3 = d_4 \approx 7$ lm), as shown by the H-cross sections presented in Figures 3.21 (g)–(i). As it is well-known that texture-induced wettability depends on the amount of air trapped within the surface

corrugations, below the water droplet [129], we explain the observed anisotropic decrease of hydrophobicity as an anisotropic distribution of such trapped air volumes. It is worth to note that the pillar height is observed as almost constant (≈1 μm) regardless of the elongation state of the pillars, with just a slightly decrease of less than 300 nm in the strong elongation state. This observation supports a change of hydrophobicity as mainly related to the modified pillar cross section rather than a drastic decrease of the pillar height.

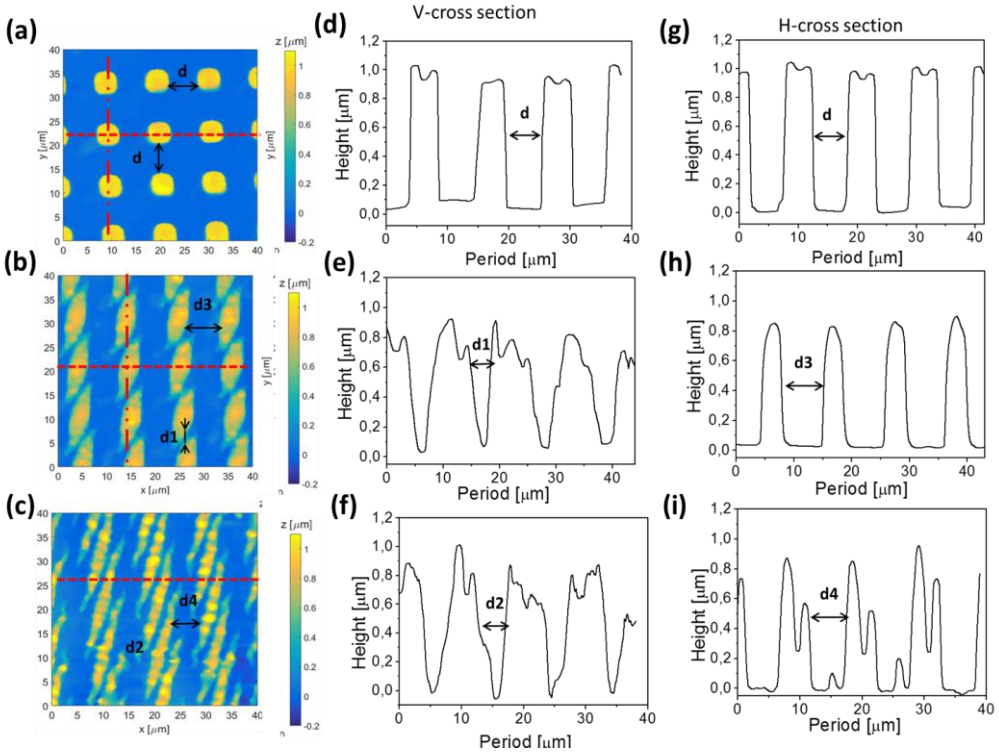

Figure 3.21: AFM maps and topographic cross sections of pDR1M textured surfaces: (a), (d), (g) as-fabricated; (b), (e), (h) irradiated for 8 s; and (c), (f), (i) irradiated for 12 s [128].

With this approach, we are able to vary the contact angle of a water droplet on the structure by more than 30°. This process can be partially reversed provided that the pillar elongation is kept within a roundness larger than about 0.5. It is well know that the photofluidization is a polarization direction-sensitive phenomenon. So since the light induced modification of the pillars is a plastic deformation, it is necessary to adopted a linearly polarized light to driven a reconfiguration of the

shape along a specific direction, instead of using just a circularly polarized or not polarized light, which it lead to a disorder and not realignment of the azo-molecules along a selected direction. However, other azopolymeric compounds can be adopted to improve reversibility deformation.

3.4 Polarization-Driven Birefringence on Flat and Structured Surfaces

The interest of some materials for their optical properties upon irradiation with polarized light has been known since the beginning of the 1900s in photographic silver emulsions. In azobenzene-containing viscous liquids and polymers, a photoinduced anisotropy was observed in the 1960s, and was soon after associated with the photoisomerization reaction. In 1984, Todorov et al. [130] suggested the use of azobenzene-containing polymers for polarization holography [131]. Liquid crystallinity was believed to be necessary for the light-induced alignment of the azo chromophores, known as photo-orientation, but by early 1990s it was realized that intrinsic order was not a prerequisite for stable photoinduced birefringence and amorphous systems could be used as holographic recording medium as well [132]. Afterwards, a substantial amount of research has been dedicated to understanding the optimal conditions regarding both the material itself and the experimental setup [133]. These efforts have resulted in a number of highly efficient materials for applications such as LC alignment [134,135], holography and reversible data storage [136] .

An azobenzene molecule, if irradiated with linearly polarized light, preferentially absorbs light polarized along the long axis of the molecule (transition dipole axis). Actually, this means that the absorption of molecules perpendicular to the polarization axis of the incident light is negligible compared to the molecules positioned along the long axis. Repeated cycling between the *trans* and *cis* states (highly efficient in pseudostilbene-type chromophores), results in reorientation perpendicular to the polarization direction(s) of incident light. Upon continuous illumination the concentration of azo molecules perpendicular to the polarization direction increases gradually before reaching a saturation level. The resulting anisotropy, which induces large and stable in-plane birefringence, can be observed in the Figure 3.22. Irradiation with unpolarized or circularly polarized light can re-establish the original isotropic orientation, enabling many subsequent photo-reorientations. In a typical photoinduced birefringence experiment, a linearly

polarized beam of moderate power and wavelength matching the absorption band of the chromophores is used to induce orientation of the chromophores. The anisotropy evolution is monitored by measuring the transmittance of a low-power probe beam through a polarizer/sample/analyzer configuration. The transmission direction of the polarizer/analyzer is set to ±45° with respect to the polarization direction of the writing beam in order to maximize the transmitted signal I. Once the irradiation is terminated, a fraction of the oriented chromophores will be randomized again due to thermal relaxation, resulting in a decrease in the birefringence.

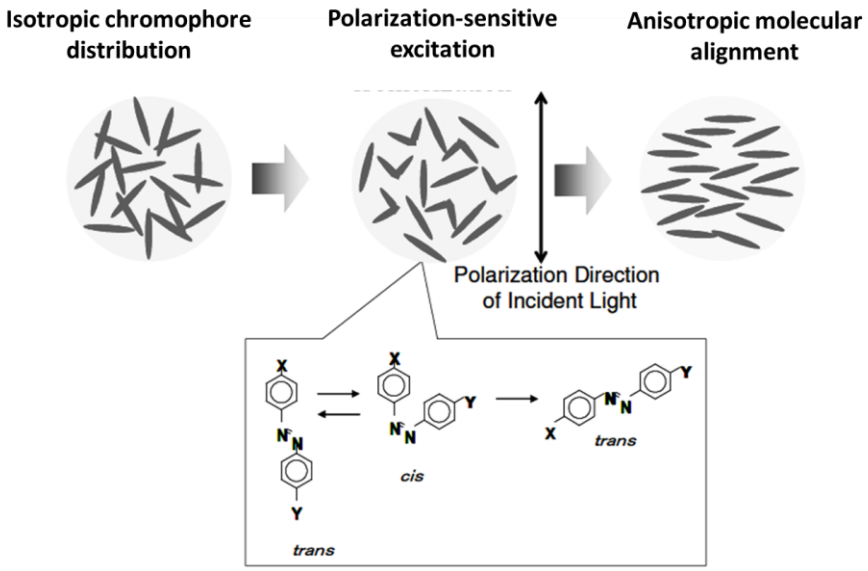

Figure 3.22: Photoinduced orientation of azobenzene derivatives resulting in an anisotropic molecular alignment.

The efficiency of photo-orientation in a given material is a complex result of many parameters such as chromophore structure and intermolecular interactions, type of bonding to the matrix and cooperative motions. The nature of matrix material plays a very important role as it can either enable or restrict the motion and interactions of the chromophores. In general, photoinduced anisotropy has been reported to be higher and more stable in LC systems than in amorphous polymers due to strong cooperative movement and intermolecular interactions of the photochromic units and the mesogens [104].

In this subsection, we show that the optical behavior of a photo-responsive polymer can be tuned in a reversible way. First, we demonstrate that the PAZO-PMMA film exhibits birifringence when illuminated by properly polarized light. Afterwards we show that the same polymer can be easily structured over large area by means of soft-lithographic techniques. In particular, we present an array of micro-pillars, and we show that light transmittance can be tuned in each element of the array. As a result, the polarization state of the emerging light can be finely controlled in space and time. The opportunity to manipulate the polarization state of light by an active optical control enables the fabrication of dynamically tunable holographic surfaces and metasurfaces.

The optical setup used in this experimental part, is represented in Figure 3.23. It consists of an holgen lamp whose white light is linearly polarized and used to illuminate the sample. Collection is performed by means of an objective and then polarization-filtered by a second polarizing filter orthogonal to the first one The image obtained on the CCD is therefore composed by light with polarization orthogonal to the initial polarization of white light. A Beam splitter (BS) allows to superpose a linearly polarized laser beam ($\lambda = 490$ nm) to the white light path. The laser beam passes through a quarter wave plate and is circularly polarized. Subsequently, a linear polarizer that can rotate selects the polarization direction of the laser beam.

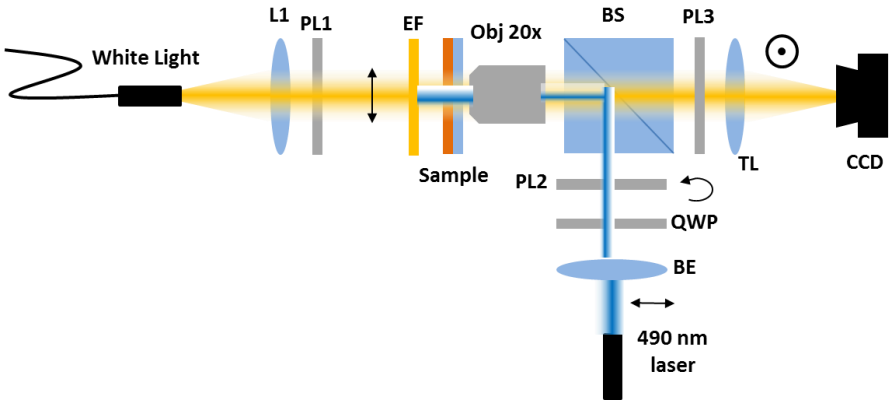

Figure 3.23: Optical custom-made setup used in the experimental part. L: lens, PL: polarizer, EF: edge filter, Obj 20x: objective, BS: beam splitter, TL: tube lens, QWP: quarter wave plate, BE: beam expander.

First we aim at characterizing the material response on a flat surface. The sequence of images below shows that in the initial state there is no light reaching the CCD camera because of the orthogonal polarizer provide complete extinction of transmitted light (fig. 3.24a). When the blue laser is turned on and its polarization is set parallel to the PL3 axis, a bright spot appears. The bright spot is associated to white light whose polarization state has been rotated due to interaction with the azo-polymeric thin film. By moving the sample, we can create a transmissive pattern (fig. 3.24a,b), showing that the birefringence induced has a latency that may be attributed to the limited motility of the azopolymer within the PMMA matrix. The process can be reversed by rotating the polarization state of the laser beam, thus restoring the initial condition (fig. 3.24d).

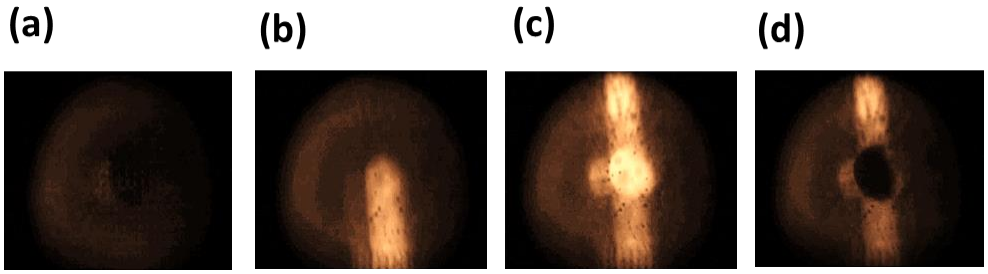

Figure 3.24: image sequences of the creation of a transmissive pattern.

The latency of the induced birefringence has been characterized by measuring the time evolution of the transmitted intensity of white light after switching off the laser beam. The intensity profile is well fitted by a bi-exponential function (fig. 3.25a) with a fast decay time $\tau_1 \approx$ 2s and a slow component with a much longer decay time $\tau_2 \approx 10^2 s$.

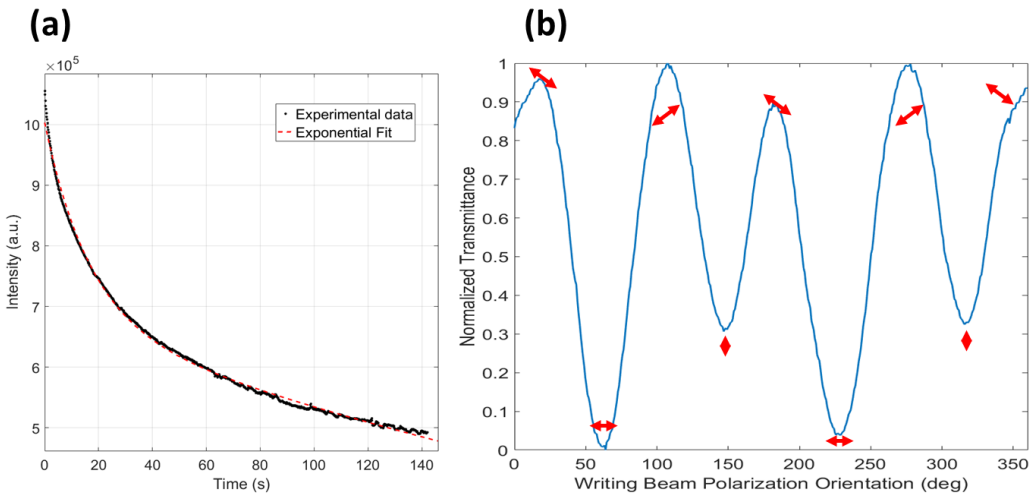

Figure 3.25: (a) Transmitted Light Intensity as a function of time. At time t = 0 s the writing beam is switched off; (b) Normalized Transmitted Light Intensity as a function of the writing beam polarization orientation.

Figure 3.25b shows that the transmittance can be modulated by rotating the polarization state of the incident beam. The maxima of transmittance are found when the Electric field of the writing beam is oriented at 45° with respect to the white light polarization. As the writing beam polarization turns parallel or perpendicular to the white light polarization state, the transmitted intensity drops to a minimum. The intensity profile is therefore periodic by rotations of 90° of the writing beam electric field orientation.

When the surface is structured in an array of micropillars, the polarization induced birefringence can be exploited to address the transmittance of individual micropillars (Figure 3.26). The amount of light transmitted through each individual pillar depends on the total thickness of the pillar itself, while the dependence on the writing beam polarization orientation follows the behavior described in Figure 3.25.

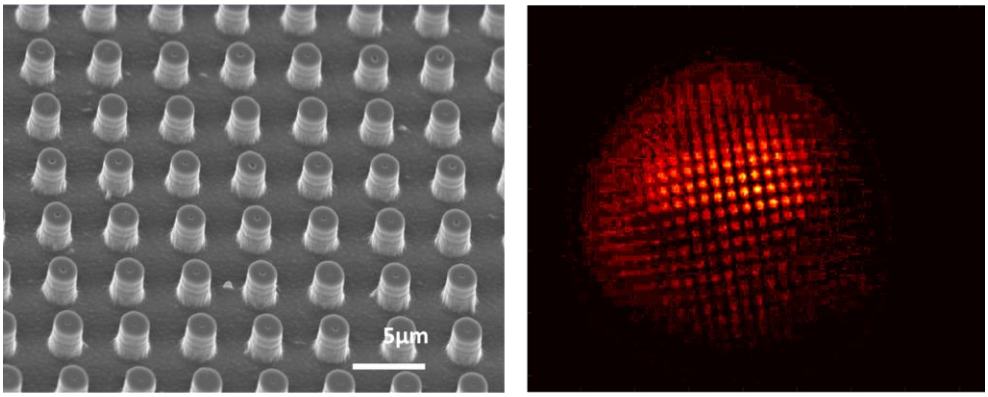

Figure 3.26: SEM image of the PAZO-PMMA array of micropillars and image of the structured surface when a region is irradiated by the writing beam.

4

Guest-host azopolymeric material

The interest in polymeric optical materials is a consequence of the intriguing optical properties of organic molecules, which can be optimized to meet the requirements of a specific application. In this work, polymeric optical materials refer to material systems where the optical response is provided by guest molecules, that are either doped into or bonded to the host polymer [137]. The optical response arises from chromophores, while the task of the polymer matrix is not only to ensure good film-forming, thermal, and mechanical properties but also to prevent excessive chromophore–chromophore interactions. The function of the chromophores can be based, e.g., on their photoisomerization, photoluminescence, or nonlinear optical response [138]. In fact, quantitative understanding of the structure–property relationships, orientational ordering, and relaxation phenomena in polymer–chromophore systems has largely been driven by the nonlinear optics community and was later applied to analyze the photoinduced orientational mobility of azobenzene-containing polymers [101]. Each application requires an active chromophore with a different structure and properties, and when it comes to practical device applications, the sample composition and the nature of bonding to the polymer matrix have to be carefully designed and optimized.

Among these, in this chapter we focus in the design of novel materials based on azobenzene doped-systems and in the study of their photo-responsive behavior and potential applications.

The incorporation of the photoactive chromophores into the polymer matrix can be done in different ways [139]. The first approach is the simplest and it consists in dissolving the chromophores into the host polymer to form a guest–host system (Figure 4.1a). These systems are simple and cost-effective as they only require mixing of the constituents in order to produce the desired compound. So in principle, the chromophore concentration and the composition of a guest–host system can be easily controlled. In practice, however, there are numerous undesirable features that limit the practical usability of guest–host systems. The

solubility of the dopant molecules is limited to moderate levels because of aggregation effects and macroscopic phase separation. Another severe issue is the high degree of orientational mobility of the chromophores within the polymer matrix due to the lack of chromophore–polymer interactions. To overcome the problems of guest–host systems, the active molecules have been chemically attached to the polymer backbone (Figure 4.1b).

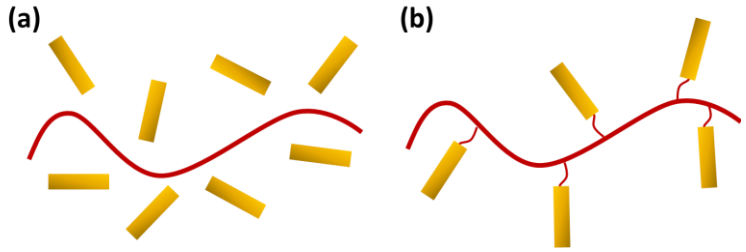

Figure 4.1: Schematic representation of (a) conventional guest–host system with essentially no interaction between the chromophores and the polymer chains, (b) covalently functionalized side-chain polymer.

Such covalently functionalized polymers allow high concentration of the active chromophores to be homogeneously incorporated into the polymer without phase separation. An important advantage is that the orientational relaxation of the chromophores is hindered by the covalent attachment and the T_g is generally higher than in corresponding guest–host systems, resulting in superior temporal and thermal stabilities in applications that require net alignment of the chromophores [140].

The incorporation of such photosensitive groups or molecules into a tailored polymer surrounding is a well-established strategy for transferring effects from the molecular level into effects that are macroscopically visible.

Here, we investigate the possibility to incorporate azobenzene chromophore both in a flexible matrix and in a rigid host matrix, in order to study the photosensitive behavior at a macroscopic scale by exploiting optical characterization. A highly sensitive, tunable and flexible material based on azo chromophore-embedded PDMS and a rigid azo-doped acrylic suspended membrane are developed.

4.1 Photo-deformable elastomeric system

In this work, the light responsivity of proper azo compounds incorporated within an elastomeric matrix (which is unresponsive in its pure form) is exploited as tunable optical lens with adjustable focus capabilities.

Polydimethylsiloxane (PDMS), is a low cost flexible and optically transparent polymer that is inert to many organic/inorganic compounds, has been widely used as a template/mold for structuring [141], and as a substrate for microfluidic channel formation [142]. During investigation aimed at the development of innovative and more performing PDMS mold for developments in soft imprinting, we formulated the hypothesis that embedding of photoactive azobenzene molecules in PDMS would enable fabrication of a unique, transparent, flexible and reversible system.

The novel material developed is a mixture of Polydimethylsiloxane (PDMS, from Dow Corning, Sylgard 184) and azopolymer. The elastomeric compound containing the azopolymer is obtained by means of a mixing and drying method. The PDMS prepolymer is obtained by mixing the elastomer solution and the curing agent in a proper ratio (10:1, w/w). The mixture is left in a desiccator until the air bubbles are completely removed. The choice of the azo is crucial to obtain good optical quality. In Figure 4.2 two different samples are shown.

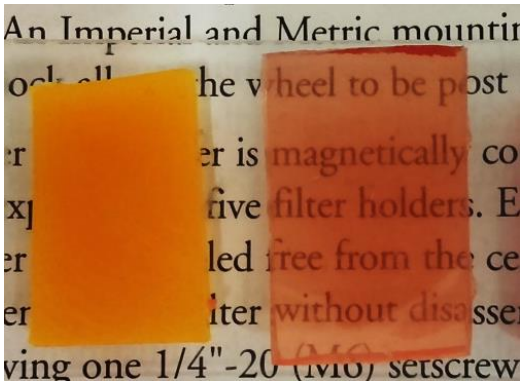

Figure 4.2: Thick membranes based on PDMS with PAZO and pDR1M respectively.

On the left side (yellow sample), the compound is a mixture of poly[1-[4-(3-carboxy-4-hydroxyphenyl-azo) benzene sulfonamido]-1,2- ethanediyl, sodium salt] (PAZO) and PDMS. The sample appears as rather opaque because of the high scattering effects, raising from a bad dissolution of PAZO in PDMS. The sample

on the right is obtained by mixing pDR1M with PDMS and shows good optical quality, thanks to the good miscibility of poly(Dispersed Red 1 Methacrylate) into PDMS, making it the best candidate. Therefor in all experiments we use pDR1M dissolved in toluene (anhydrous, ≥99.8%, Sigma Aldrich) at 2 wt.% concentration. In order to find the finest material in terms of optical quality and photoresposivity, different amounts of pDR1M in solution (20µl, 70µl, 120µl, 170µl) are mixed to 5 ml of the PDMS prepolymer and vigorously stirred until the azopolymer is totally dissolved in the host material. Mixing is a critical step, as scattering effects due to azopolymer clots should be carefully avoided. For this reason, we employ pDR1M because of its miscibility with PDMS, thus enabling a good optical quality. The resulting blend is left at room temperature to remove the remaining air bubbles and to let the solvent to evaporate completely. Then, the mixture is put in oven at 60°C for 2h, for thermal curing. The results are a flexible PDMS-based material showing different colors from light orange to dark red, depending on the concentration of azo, see Figure 4.3.

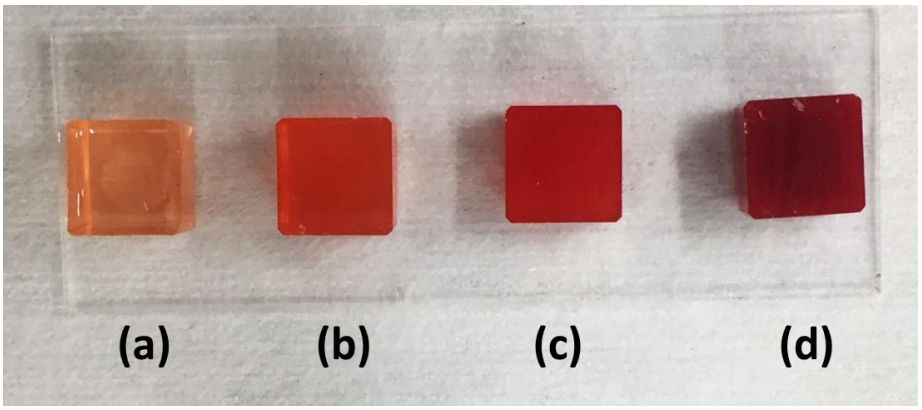

Figure 4.3: PDMS-based material at different containing different amounts of pDR1M in Toluene (a) 20µl, (b) 70µl, (c) 120µl and (d) 170µl.

Finally, the best amount of azo is 70µl, thus enabling a good optical quality and transparency, as clearly visible in Figure 4.4a. Figure 4.4b shows PDMS-pDR1M molded as a squared plate 2.5 cm side length and 2.7 mm thickness used in all experiments. The reddish color is due to the pDR1M absorption band, which make it suitable to be light-triggered by a green radiation (see Figure 4.4c).

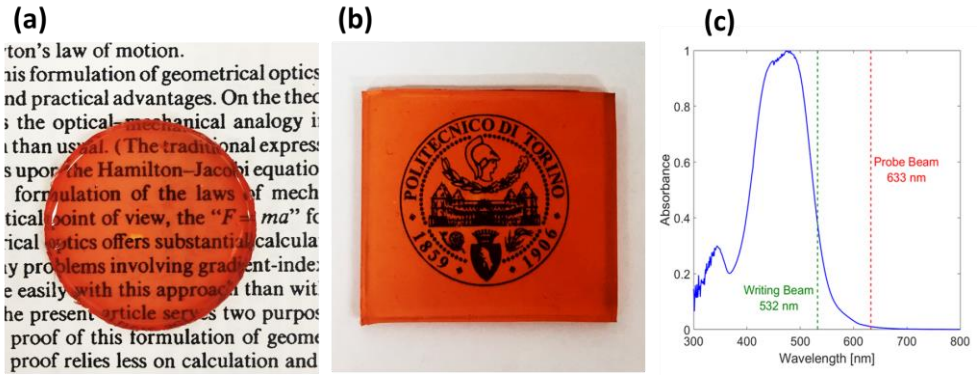

Figure 4.4: PDMS-pDR1M, (c) pDR1M optical absorptium spectrum.

4.1.1 Reconfigurable graded-index optical elements controlled by light

In this work, the elastomeric PDMS-pDR1M, is used as optical element, whose transmission function can be reversibly phase-configured by light. In many optical applications, there is an increasing need for dynamically tunable optical elements able to shape the wavefront of light 'on demand'. In this framework, Liquid Crystals (LC) have been extensively used for wavefront engineering applications [143] because of their ability to tune optical properties when an external electric voltage is applied thereto. Recently, the imaging capabilities of a LC-based micro-lens array wherein the focal length can be electrically varied has been reported [144]. However, such and similar systems based on electrically-driven birefringence exhibit an unavoidable sensitivity to the polarization of light, and polarization free LC based tunable lenses are obtained at the cost of increased complexity in the fabrication process [145]. Beside LC-based devices, liquid lenses have also attracted great interest [146]. In a liquid lens, an accurate modification of the Optical Transfer Function (OTF) can be achieved by varying the curvature of an interface between liquids having different refractive indexes. As an intriguing alternative, flexible membranes made of stimuli-responsive materials can be employed as tunable lenses, wherein the focal length can be controlled by external physical/chemical stimuli, such as temperature, PH or electromagnetic fields [147]. Liquid or membrane-based lenses with adjustable focus capabilities somehow mimic the operation of the human eye, which is still one of the most performing optical system in nature. However, the eye's ability to image objects at different distances with nearly no aberrations relies both on a mechanical actuation and on a

graded refractive index (GRIN) distribution that is typically not provided in state of the art active lenses. In this work, we propose the crosslinked elastomeric blend PDMS hosting pDR1M as adaptive GRIN optical element whose OTF can be reversibly varied by means of laser irradiation, with no need of pre-patterning.

Here we show that the spatial distribution of the refractive index change associated to such a light-induced volume expansion can be exploited as an optical phase function for wavefront-shaping of any other incident radiation whose frequency falls outside the absorption bands of the azo-groups.

Part of the work described in this section has been previously published in Light Science and Application, 2017 (***Publication VII***).

4.1.2 Interferometer optical setup

As sketched in Figure 4.5, a 'writing' laser beam at λ_w =532 nm wavelength illuminates the sample and triggers the pDR1M photo-isomerization (*trans-cis*). As a result, a corresponding density and refractive index decrease is produced within the PDMS network. In order to quantitatively evaluate the amount of refractive index variation, an interferometric system based on a Mach-Zehnder configuration is employed. Thanks to the sample transparency at wavelengths above 600 nm (Figure 4.4c), a well-collimated λ_p=633 nm 'probe' beam superposed to the 'writing' beam is transmitted through the polymeric slab and collected by a long working-distance objective, for subsequent phase imaging. The interferometer implemented in this work is depicted in Figure 4.5. A He-Ne laser beam (λp = 633 nm) is expanded and split into a reference beam and an object beam by means of a polarizing beam splitter (PBS). The fringes contrast is controlled by adjusting the intensity and polarization of the reference beam by means of a Half Wave Plate (HWP) and a neutral density (ND) filter. The object beam is diffracted by a phase-only Spatial Light Modulator (SLM – Holoeye Pluto vis-006c), that sequentially provides five $\pi/2$ phase shifts for phase retrieval. The first-order diffracted beam, referred as the 'probe' beam, is transmitted through the sample and is then collected by an objective (Mitutoyo Long Working Distance, 20x 0.42 NA). A tube lens (TL) produces an image of the object plane of the objective onto a CMOS camera (Thorlabs DCC14p35M), where the reference beam is also superposed. Finally, an interferogram is recorded for each phase shift provided by the SLM. Phase maps are obtained by a proper combination of the 5 interferograms. A phase-unwrapping processes based on the Goldstein method is then performed [148]. The imaging system is arranged in such a way that the wavefront retrieved onto the CMOS

camera is flat (within the objective field of view) when no sample is placed beneath the objective. The interferometer is also equipped with a doubled frequency Nd:Yag laser emitting a TEM_{00} Gaussian beam at λ_w =532 nm wavelength, with tunable power up to 200 mW. This 'writing' beam is superposed to the 'probe' beam and is intended to induce refractive index modifications on the PDMS-pDR1M slab. After a beam expansion stage (BE 1x), the maximum incident power onto the sample is 100 mW. The part of 'writing' beam power transmitted through the sample is then filtered by an edge filter (Semrock RazoEdge MaxLine 532) before reaching the CMOS camera, in order to avoid disturbances to the interferograms recording.

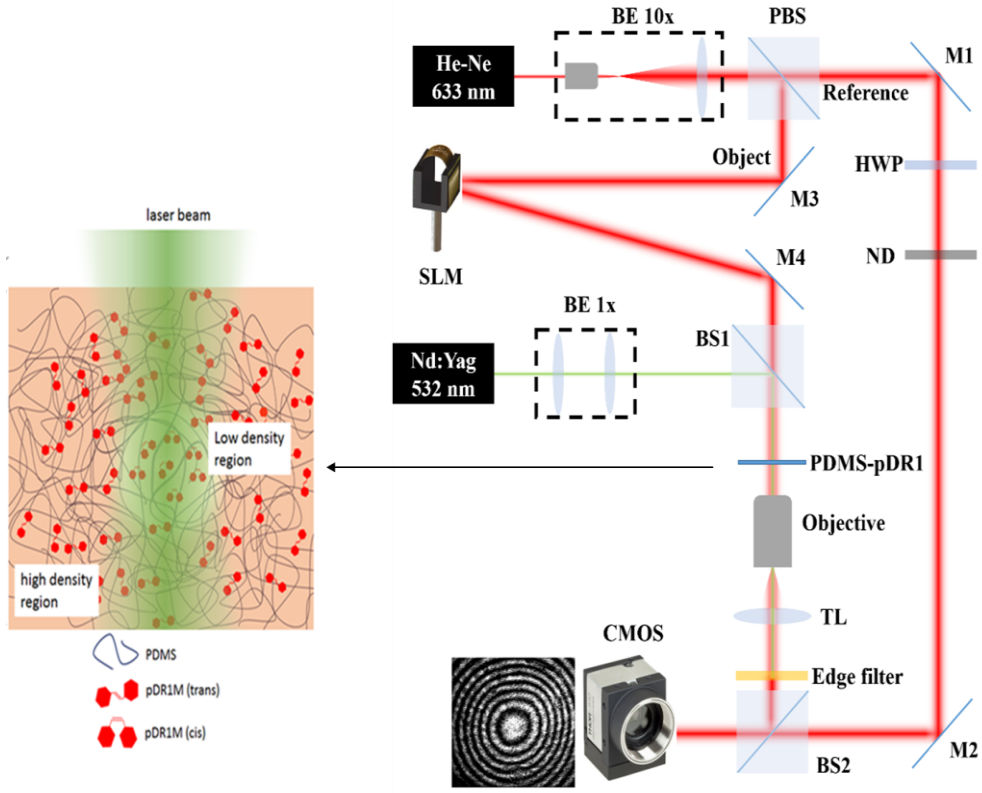

Figure 4.5: Schematic view of the interferometric microscope employed for the characterization of the optical response of the elastomeric GRIN element.

4.1.3 Tunable optical lens-like device

The 'writing' radiation is a linearly polarized Gaussian beam having a beam waist $w_0 \approx 650$ μm that illuminates a 2.7 mm thick PDMS-pDR1m slab

perpendicularly. The collection objective is positioned such that the top surface of the sample is imaged on the camera. Figure 4.6a shows the unwrapped phase map retrieved for the 'probe' beam transmitted through the slab during irradiation by the 'writing' beam (power 100 mW). The unwrapped phase has an axis-symmetric convex profile, meaning that the transmitted 'probe' beam is divergent along the forward-propagation direction. This effect can be explained by invoking an optical path decrease corresponding to the region irradiated by the 'writing' beam, which is in agreement with the expected light-induced mass density decrease described elsewhere [149]. As the unwrapped phase is determined up to a constant, such a baseline value is first determined by means of a Gaussian fitting, and then subtracted. Because of the limited field of view of the imaging system, the measured phase appears as larger than zero at the map boundaries.

For a better evaluation of the phase profile, a cross section along a diagonal line (black dashed line in Figure 4.6a) is shown in Figure 4.6b.

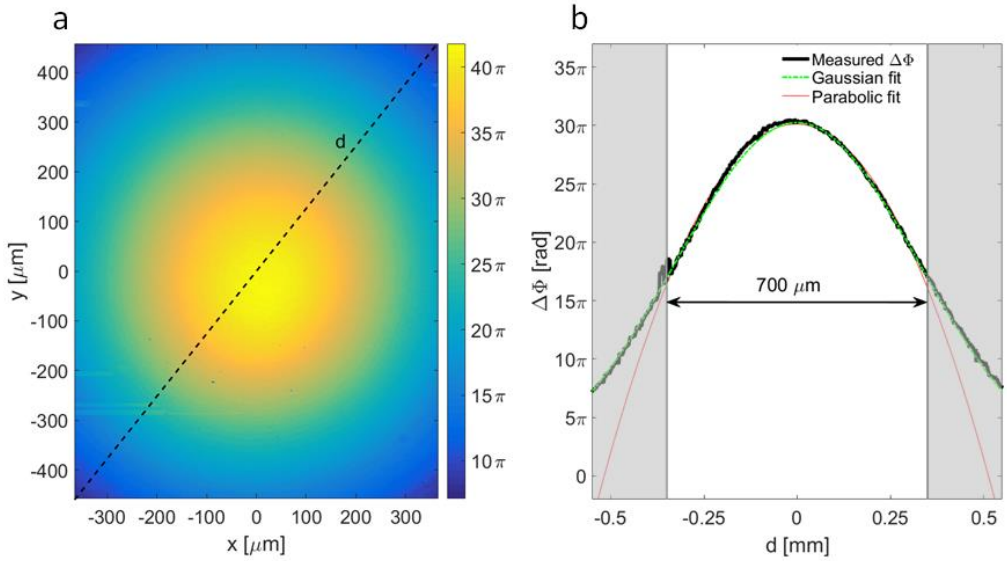

Figure 4.6: a) Unwrapped phase map of the 'probe' beam transmitted through the PDMS-pDR1M slab. b) Cross-sectional phase profile along a diagonal cut and corresponding parabolic fit within the 700 μm-wide fit interval (red dashed line).

Interestingly, the phase profile is Gaussian, as the 'writing' beam is. However, within a range of about 700 μm centered on the symmetry axis, the phase profile is

well fitted by a parabolic function (red dashed line in Figure 4.6b), as the first term in the Taylor expansion of a Gaussian is a quadratic power.

This suggests that this central region of the light-induced GRIN distribution can actually operate as a concave lens with a negative focal length (paraxial approximation).

For a rational use of this light-induced lens effect, a predictive mathematical model is required. To this aim, a Finite Element method for Ray-tracing (FER) in graded index media [150] has been implemented. The model computes ray trajectories within a medium characterized by a given GRIN distribution, therefore it is essential to provide a quantitative estimate of the refractive index distribution within the PDMS-pDR1M volume. In our model, non-linearity is not considered, therefore the intensity distribution of the 'writing' beam is assumed to be independent to the light-induced refractive index change in the medium. According to the experimental configuration, the waist position corresponds to the entrance side of the PDMS-pDR1M slab. The maximum value for the light-induced refractive index can be deduced by comparing the phase values (baseline-subtracted) as measured correspondingly to the maximum intensity of the 'writing' beam (at x=y=0) and outside the region irradiated by the 'writing' beam. As the phase accumulated by the 'probe' beam results from an integration along the optical path, the following phase difference can be calculated as resulting in $n_{ind}^{\max} = 5.6 \cdot 10^{-3}$. The maximum value of the light-induced refractive index distribution $n_{ind}^{\max}$ can be varied by varying the 'writing' beam power. In Figure 4.7a, several phase cross-sections measured in different writing power conditions are shown, wherein the maximum phase difference increases at increasing writing power. However, seems to have a saturable behavior, as suggested by the increasingly smaller ΔΦ variations detected at higher writing power. Within an inner 700 μm wide region, a parabolic profile is well fitting the measured phase for the entire range of writing power considered. From the fit coefficients it is straightforward to calculate the equivalent focal lengths of the PDMS-pDR1M GRIN slab as $f = \pi \lambda_p^{-1} a$ at different 'writing' beam intensities. Results are shown in Figure 4.7b, demonstrating focal lengths as low as 14 mm (corresponding to a NA=0.025 for a 700 μm wide entrance pupil) at maximum writing power.

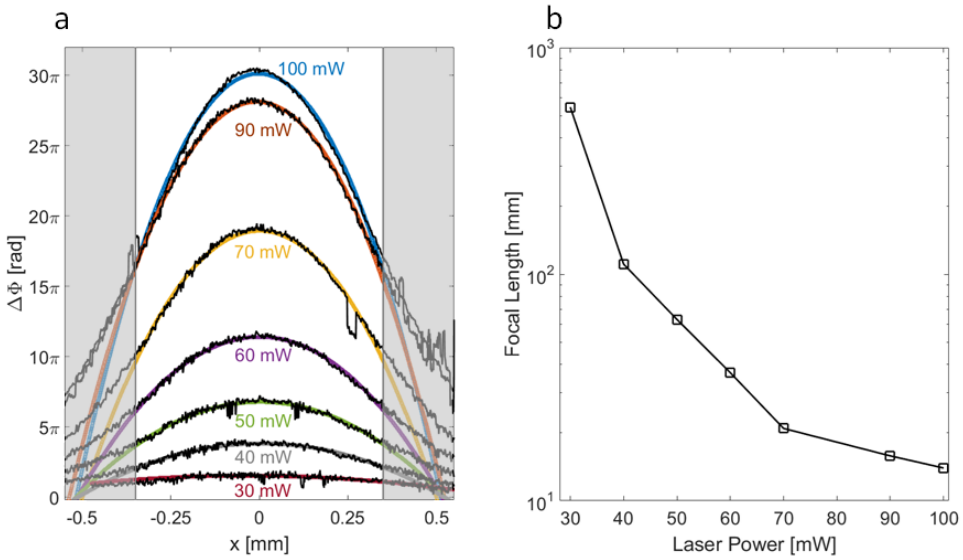

Figure 4.7: a) Phase profiles (black solid lines) of the 'probe' beam for different intensities of the 'writing' beam and corresponding parabolic fits, as indicated (colored solid lines). b) Focal lengths of the PDMS-pDR1M as a function of the 'writing' beam power.

The tunable-focus capability of the PDMS-pDR1M element is exploited for white-light imaging, wherein the 'probe' beam is replaced by a halogen lamp and the reference beam is excluded. The PDMS-pDR1M slab is placed in between the collection objective and the sample, at 10 mm distance from the objective. The sample object is a glass slide 1 mm thick, having two chromium patterns lithographed on each side and it is positioned in such a way that the top pattern is imaged onto the CMOS camera (Figure 4.8a). When the 'writing' beam is switched on, a progressive increase of the effective focal length of the system is produced, till the bottom pattern can be imaged through the glass slide (Figure 4.8b).

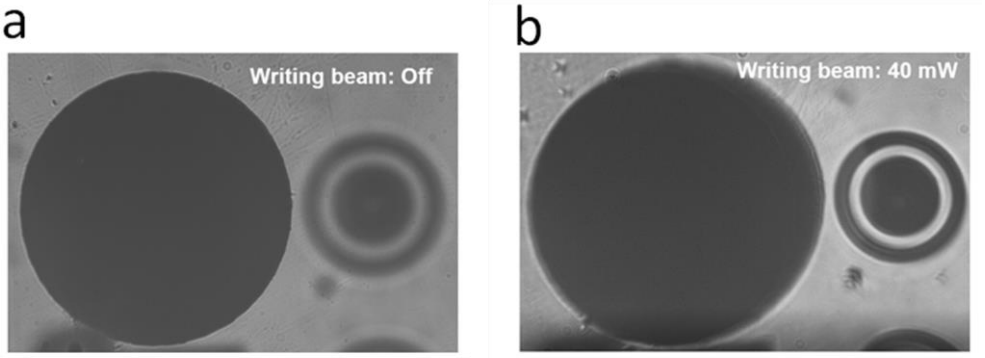

Figure 4.8: a) White-light image of the top pattern of the sample in a switched-off 'writing beam state. b) White-light image of the bottom pattern of the sample in a switched-on 'writing beam state (roughly 40 mW). The two patterns are longitudinally separated by a 1 mm thick glass slide.

As an alternative application, a white-light imaging system based on a pair of 2-inch biconvex lenses (focal length 60 mm) is proposed (Figure 4.9a), wherein the PDMS-pDR1M slab is positioned in the pupil-conjugated plane of a first collection lens, as commonly done in microscopy systems employing tunable lenses. The lens configuration is 4-f, therefore the overall magnification is close to unity. In between the two lenses, a dichroic mirror is positioned such that the λ_w=532 nm 'writing' beam is reflected toward the PDMS-pDR1M slab, while red-IR radiation is transmitted along the optical axis. In front of the CMOS camera, an edge filter blocking the laser stray light and residual reflections from the dichroic mirror is placed. The imaged objects are constituted by a scattering element (a polymeric 3D-printed cantilever array) and an amplitude mask (a photolithographic plate) and are axially separated by a D=1 cm gap. Two independent halogen lamps illuminate the objects from the rear of the amplitude mask and from the front of the cantilever array. Thanks to the large size of the optical elements used, the field of view of this system is roughly 5 mm. The objects are placed in such a way that the cantilever is normally in-focus when illuminated by the halogen lamp (1), as shown in Figure 4.9b. In fact, when the halogen lamp (2) is switched on, the amplitude mask looks out-of-focus, while the cantilevers are still in-focus (Figure 4.9c). As the writing beam (Gaussian shape) is illuminating the PDMS-pDR1M in the back focal plane, an approximately parabolic phase profile is produced, bringing the amplitude mask in-focus on the image plane (Figure 4.9d). We observe here that the advantage of inserting the PDMS-pDR1M slab in the back focal plane of the first collection lens

relies in the opportunity to limit the light-induced refractive index change over a small region of interest, thus alleviating the need of high-power laser sources. In addition, this choice opens the way to a further miniaturization and integration of the polymeric tunable GRIN element in imaging systems.

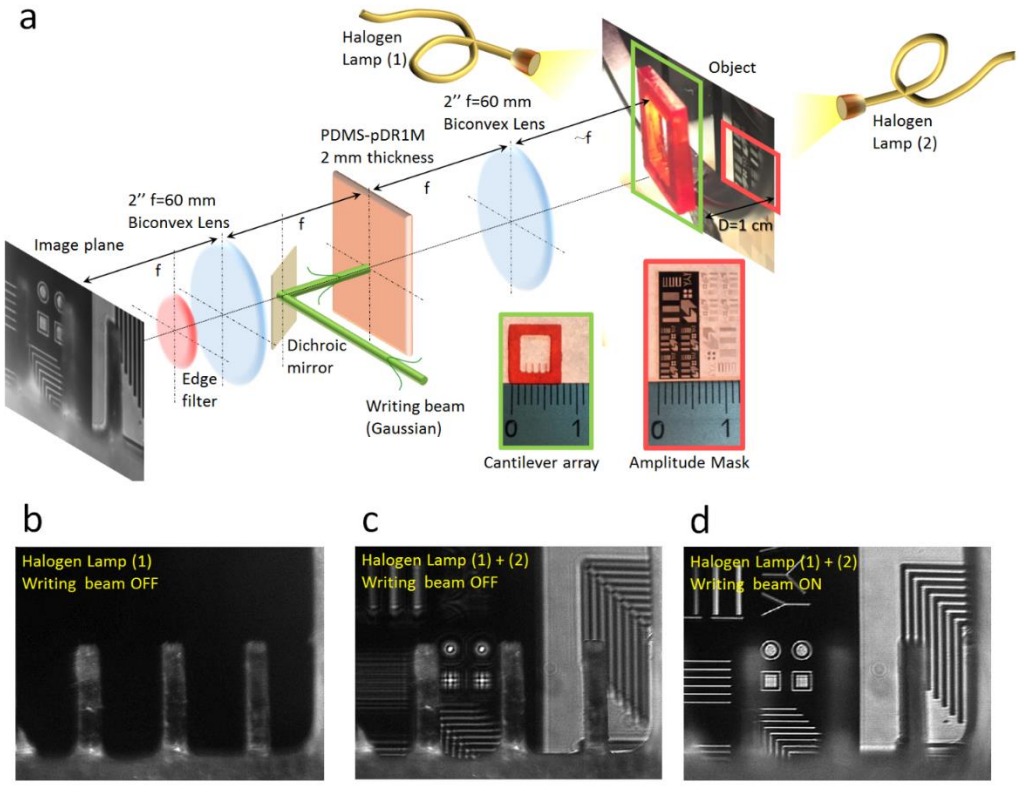

Figure 4.9: (a) Schematic of a 4-f imaging system based on 2" biconvex lenses. Imaged objects are represented by an amplitude mask and a 3D-printed cantilever array (see insets) that are axially separated by an air gap about 1 cm wide. The PDMS-pDR1M slab is placed in the pupil-conjugated plane of the first collection lens. Illumination is provided by two separate halogen lamps allowing the objects to be imaged upon collection of both scattered and transmitted light. b) Illumination by halogen lamp (1): the cantilever array is imaged in-focus (scattered light). c) Illumination by halogen lamps (1) and (2): the cantilever array is imaged in-focus (scattered light) and the amplitude mask is out-of-focus (transmitted light). d) Illumination by halogen lamps (1) and (2): the cantilever array is out-of-focus (scattered light) and the amplitude mask is in-focus (transmitted light) upon irradiation of the PDMS-pDR1M slab by the 'writing' beam.

4.2 Photo-actuable azo-doped acrylic resin

Significant advances have recently been made in the development of functional systems that are able to undergo light-induced shape changes. The main challenge in the development of such polymer architectures is the conversion of photoinduced effects at the molecular level to macroscopic movement of working pieces. From this point of view, polymer actuators capable of responding to external stimuli and deforming are most desirable for practical applications, such as microfabrications, microfluidics, artificial structures (robots) for drug delivery, biosensing and microsurgery [151-153].

Within this framework, photodeformable polymers attract increasing attention from researchers, because they provide such advantages as flexibility, light weight, low cost and quiet operation compliance and light, as external stimulus is a clean energy and can be controlled rapidly, precisely and remotely. Starting in the 1960s, several amorphous polymer systems, including monolayers, gels and solid films, have been developed for the research of photoinduced contraction/expansion [154]. Recently, by using liquid-crystalline elastomers (LCEs), not only photocontraction but also photoinduced bending has been acquired [155,156]. In comparison with contraction/expansion which is a two-dimensional action, bending (a three-dimensional movement) should be advantageous for artificial hands, cellular scaffold and medical microrobots that are capable of completing particular manipulations. As opto-mechanical transduction is concerned, several strategies have been suggested for amplifying the nanoscopic force produced at each trans-cis isomerization of individual azobenzene molecules to a larger scale, one of the most promising being based on a crosslinkable LCE [157]. However, due to pre-defined spatial alignment of LCE chains, the light-induced mechanical actuation provided by the azo component is suffering for strong anisotropy [158].

Here, we propose an alternative smart system, introducing azocompounds within photocurable commercial polymeric formulations.

An available monomer (purchased by Sigma Aldrich), bisphenol A ethoxylate diacrylate, namely BEDA is considered for the production of azo-loaded formulations. It contains a Bisphenol-A group and ethylene oxide chains length which is 2 EO/phenol (Figure 4.10a). BEDA forms a rigid network characterized by a T_g = 36°C, higher than room temperature [159]. Dispersed red 1 methacrylate (DR1M) and poly(Dispersed red 1 methacrylate) (pDR1M) are tested as light-responsive compounds, see Figure 4.10b, which can react with the monomer and

therefore can be chemically linked to the network. The photopolymerization is achieved by the addition of photoinitiator up to a few weight percent (wt%) to absorb at the wavelength of exposure and to trigger the polymerization process, which occurs via opening of chemical bonds (formation of radicals) and subsequent crosslinking. In our case, the photoinitiator is the Phenylbis(2,4,6-trimethylbenzoyl)phosphine oxide, called as BAPO, and its structure is reported in the Figure 4.10c.

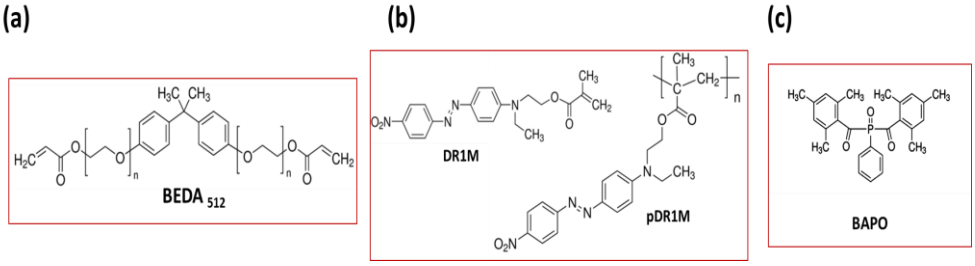

Figure 4.10: Chemical structure of (a) monomer, (b) azopolymers and (c) photoinitiator used in this work.

The very first experiment was to obtain 2D structures by means of soft lithography assisted by UV-light, see Figure 4.11a. The Light induced movement was investigated with doubled frequency Nd:YAG laser emitting a TEM_{00} beam at λ = 532 nm. The laser power is adjustable to a maximum of 250 mW. The experimental set up was made by laser source, LR objective 100xNa, filter, tube lens and cmos camera. Contrary to what expected, we didn't observe any kind of movements of the single-pillars, even varying the quantity of the azopolymer with respect to the liquid monomer starting from 1%wt. to 90%wt., where we found another issue in the UV curing do to the large amount of the azo in the resins, which drastically slowed down the crosslinking process, increasing the exposure time.

(a) (b)

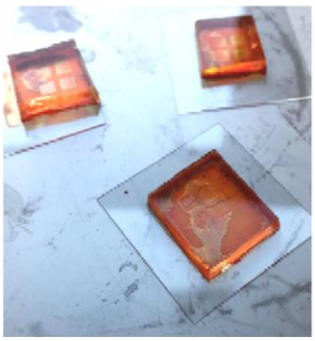

Azo [wt.%] into the resin	Crosslink time
0.2	60 sec
0.3	
0.5	
1	3 min
5	~ 25 min
10	
30	
50	~ 1 hour
70	
80	~ 2 hours
90	

Figure 4.11: (a) Commercial resins loaded with azopolyers structured by means of PDMS stamp and successively cured by UV-soft lithography technique. (b) Summary table of the different concentration added into the liquid monomer.

One of the possible explanation is due to the crosslinked network, that hampers the movements of the individual pillars, inducing a macroscopic movements of the whole volume. Another reason could be the substrate, on which the resin film is casted, that's limits the expansion and consequent deformation of the membranes. So, in this context, we prepared very simple and easy-to-fabricate self-standing membranes, see Figure 4.12, in order to see if the detachment of the material from the coverslip is a relevant and essential aspect for a mechanical actuation of the membrane. Upon irradiation (532 nm), the self-standing membranes started to expand progressively, in accordance to the intensity of the laser beam. This effect occurs just when the membrane is illuminated, and concludes as soon as the laser is turn off. The best combination in terms of light actuation was resulted to be the solution with 1% of azopolymer incorporated into the liquid monomer. The result obtained from this trial is that free suspended membranes have more degrees of freedom. As a consequence, there are no constraints for the movement and the light actuation is clearly visible over a large area.

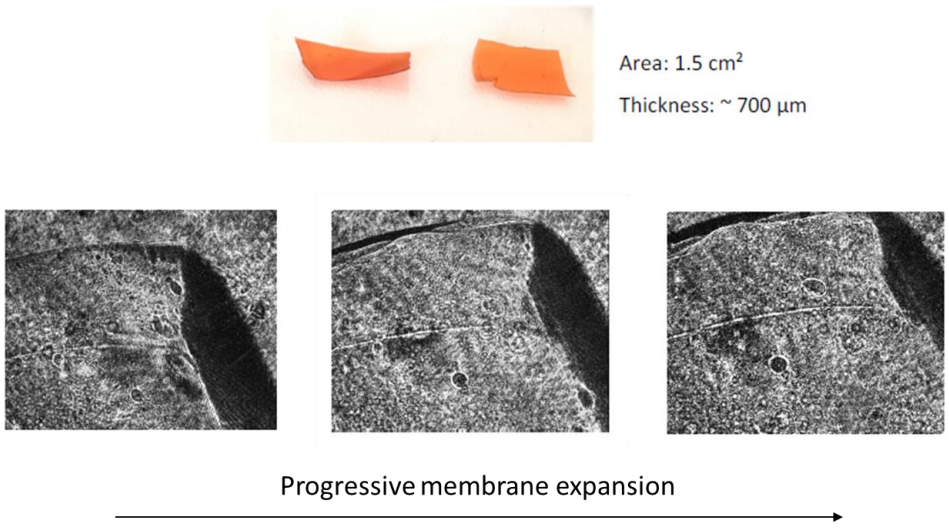

Figure 4.12: Self-standing membranes, and white images of the progressive membrane expansion upon laser irradiation.

The idea is to observe this effect on microscale suspended membranes, for a potential application in a biological field. A 3D responsive structure able to undergo on an expansion/contraction could be a suitable scaffold for cell culture.

Therefore, the next step is to obtain accurate suspended membranes of crosslinked matrices in a three dimensions scale by employing the two photon lithography technique (TPL), exploiting the benefits of the acrylic resins which is a suitable material for two photon polymerization. According to this aim, we provide a free-standing crosslinked amorphous network incorporating azopolymers, in order to study the opportunity to induce an optomechanical transduction of the membrane itself, just by a proper laser irradiation.

The first goal of the work is to obtained a clear, transparent and stable azo-loaded solution, able to be crosslinked by two photon polymerization process. Therefore, the best condition is to dissolve the azo in powder directly into the liquid monomer and magnetic stirrer the solution until the complete dissolution of the azo compounds is obtained. We adopted this strategy both for the DR1M (solution 1) and pDR1M (solution 2), as shown in Figure 4.13 a. What we observed, is the presence of many aggregates in the solution 2 (see Figure 4.13b), while a homogeneous and transparent red solution is found in the first case (Figure 4.13a).

Indeed, azopolymers show an intrinsic crystal nature that can cause several issues in the solution preparation (in terms of dissolution) and in the printing step, due to the potential scattering and formation of crystals aggregates. For the same reason, behavior changes at bulk level could take place during the photo isomerization process. The main difference between the two azopolymers employed is the length of the polymeric chain, longer in the pDR1M than in DR1M. This leads in a major and completely dissolution of the azo in the solution 1. To avoid this problem there is a possible way: dissolve the azopolymer into the matrix by means of a proper solvent. Anyway, it is better to avoid the use of a solvent in the solution preparation, because the solvent remained into the blend can induce the formation of cavitations/cavities during the lithography process. Furthermore, it's been proved that solvent can limit the absorption properties of azobenzene [160]. Nevertheless, pDR1M needs a solvent-assisted preparation, so it was firstly dissolved in a proper solvent, in our case in tetrahydrofuran (THF) and then into the liquid monomer (see Figure 4.13c). Anyway, the final solution was not clear and transparent, due to the presence of crystals precipitated after 48 hours, Figure 4.13e.

(a)

Solution	Azo compound	Liquid monomer	Photoinitiator
1	DR1M (powder)	BEDA	BAPO
2	pDR1M (powder)	BEDA	BAPO
3	pDR1M (THF)	BEDA	BAPO

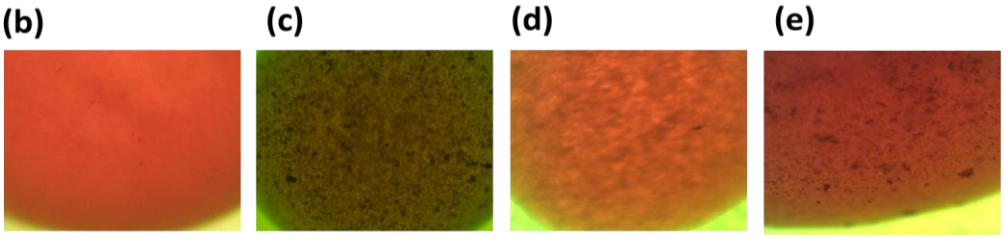

Figure 4.13: (a) list of the solution prepared, (b) solution 1, (c) solution 2, (d) solution 3 and (e) solution 3 after 48 hours.

Within this framework, DR1M and the photoinitiator BAPO, both in powder, are directly added to the liquid monomer BEDA (molecular weight 512 mol wt.) in a ratio of 1:2:97. All the materials are purchased from Sigma-Aldrich. The solution is magnetic stirred for several hours at 400 rpm, maintaining a constant temperature of 40°C. The final result is a clear and transparent light red solution. The second

solution is obtained by dissolving 1 wt.% of PDR1M and 2 wt. % of BAPOs in tetrahydrofuran (THF, anhydrous ≥ 99.9%). Next, 97 wt. % of BEDA is added to the pDR1M+BAPO (in THF) solution. The blend is firstly stirred at 70°C, 400 rpm for 8 hours to let the evaporation of the THF and then at room temperature at 400 rpm for 14h. At last, by means of a heated sonication, we obtained a final dark red solution. However, the complete dissolution of the azo into the resin is limited by the presence of aggregates of crystals after 48 hours.

As mentioned before, our goal is to obtain a printable azo-loaded resin by means of two photon lithography. The process involves the simultaneous absorption of two photons at wavelengths far from a material's linear absorption region. Whenever the material has an electronic energy level at twice the frequency of the input beam, two-photon absorption can occur. Therefore, there are many aspects that had to be consider in order to choose the best solution for two photon lithography (TPL). TPL is a very sensitive system, that needs a pure and homogenous material in order to avoid fabrication matters. Most common fabrication issues are the presence of a solvent, the formation of cavitations and the presence of crystals, that lead the generation of "bubbles" during the process. This phenomenon compromises the fabrication of stable structures, so, the suspension and stability of the 3D structures is no longer guaranteed. Crystals are given by the not complete dissolution of the powder into the liquid monomer. Cavitations are due to the presence of a solvent into the matrix. In order to avoid these potential issues, after several tests, we found the best solution to be employed in the two-photon polymerization fabrication is solution 1, which consists in BEDA monomer doped with DR1M in powder.

4.2.1 Two- photon fabrication of 3D suspended membranes

Micro/nano scale three-dimensional (3D) structures are showing their potential in different fields like photonics, electronics, telecommunication and biomedicine being exploited in application such as MEMS, information storage, metamaterials and tissue scaffolding. Different approaches have been employed for the fabrication of 3D structures including self-assembly, layer-by-layer stacking of planar patterns realized with traditional lithographic techniques, focus-ion-beam and laser holographic lithography. These techniques show a few limitation as in the complexity of the structures can be created or in the time required in the fabrication steps. An emerging alternative is direct laser writing (DLP), in which the rapid development of ultrashort laser systems is creating exciting possibilities for very precise localization of laser energy in time and space. These achievements have

triggered novel laser applications based on nonlinear interaction processes. A promising three-dimensional microfabrication method that has recently attracted considerable attention is based on two-photon polymerization via two-photon absorption and subsequent polymerization. It consists into focusing a pulsed near infrared (NIR) laser beam into a photopolymer, made by a proper mixture of a photoinitiator and a monomer, through a high numerical aperture (NA) microscope objective, leading to a multiphoton absorption only at the focal volume. The simultaneous absorption of two-photon creates radicals triggering the monomer for crosslinking only in vicinity of the focused laser beam. This results in a small solidified volume around the focal spot. By either scanning the laser beam through the resin volume or by moving the sample in three perpendicular directions, arbitrary tridimensional microstructures can be created, with no limitations in the complexity of the shape geometry. After illumination of the desired structures inside the photoresist volume and subsequent development – e.g. washing out the non-irradiated regions – the polymerized material remains in the prescribed 3D form. This allows the fabrication of any computer-generated 3D structure by direct laser recording into the volume of a photopolymerizable material. In accordance of the purpose of the work, loading the traditional resin with photosensitive compound, we aim to fabricate mechanically tunable 3D suspended membranes, aiming at giving new functionalities and opportunities for opto-mechanical transduction.

The suspended membranes are fabricated by means of two-photon lithography system, provided by Nanoscribe Photonic Professional (GT), Germany, showed in Figure 4.14. The system is equipped with a pulsed erbium doped femto second fiber laser source at a center wavelength of 780 nm. The laser power ranges between 50mW and 150mW at a pulse length between 100 fs and 200 fs. The Nanoscribe comes with a motorized coarse positioning stage (x-y-stage) and a piezo stage (piezo) for fine positioning. The x-y-stage automatically address different substrates and different writing positions on one single substrate, aiming at obtaining high defined 3D structures. The system is used in Direct Laser Writing (DLW) configuration with a high magnification oil immersion objective (100X NA 1.4).

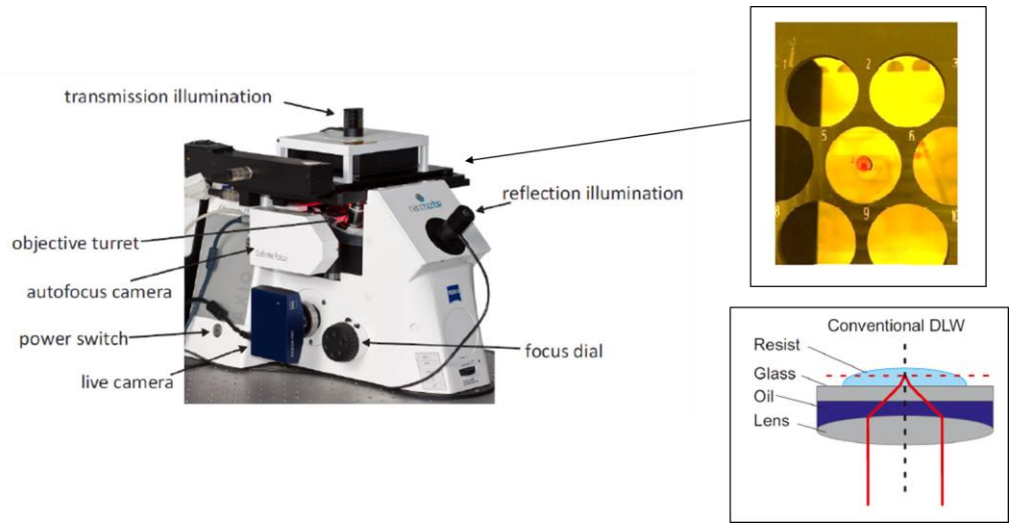

Figure 4.14: Nanoscribe microscope equipped with the relevant components. The insert corresponds to the writing method adopted for the fabrication of 3D structures.

Immersion oil is index-matched to the glass substrate and, hence, allow for ideal focusing in a resist, casted on top of the glass substrate. Then the substrate is placed into the sample holder, on the bottom side of the glass Immersol 518 F immersion oil (Thermo Fisher Scientific, USA) is placed, while the as-prepared solution is casted on the top side.

In order to obtain a large suspended membrane, the design was thought as follow, four squared pillars support a rectangular membrane, as depicted in Figure 4.15.

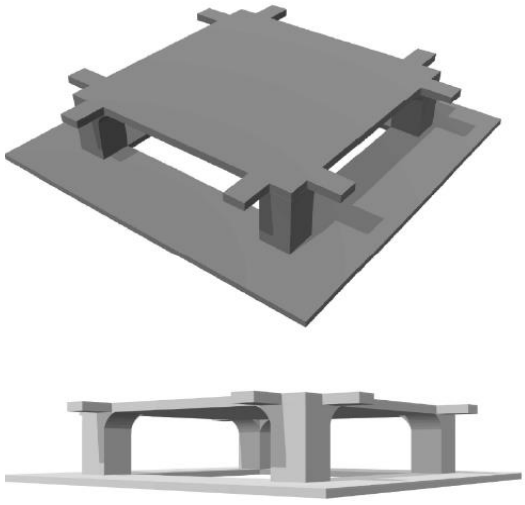

	Base	Thickness/Height
Top Layer	120 µm X 120 µm	4 µm
Bottom Layer	170 µm X 170 µm	3 µm
Pillars	15 µm X 15 µm	28 µm

Figure 4.15: Example of suspended membrane drawn on Solidworks.

The standard software applications that are commonly used in conjunction with Nanoscribe Photonic Professional laser lithography system are SolidWorks and Describe. The first one is employed to obtain the CAD file, while the latter is used to convert in a compatible file (.STL) for Nanoscribe. Since the material is home-made and it has never been used in this system, we performed different tests in order to define the best writing dynamic range, avoiding in this way the shrinking of the structure (see Figure 4.16a) and some effects due to our resist (e.g. bubbles and cavitations, Figure 4.16b). Various combinations of laser power (LP), scan speed (SS), slicing (S) and hatching (H) are tried in order to fabricate reproducible and stable architectures, as shown in Figure 4.16c.

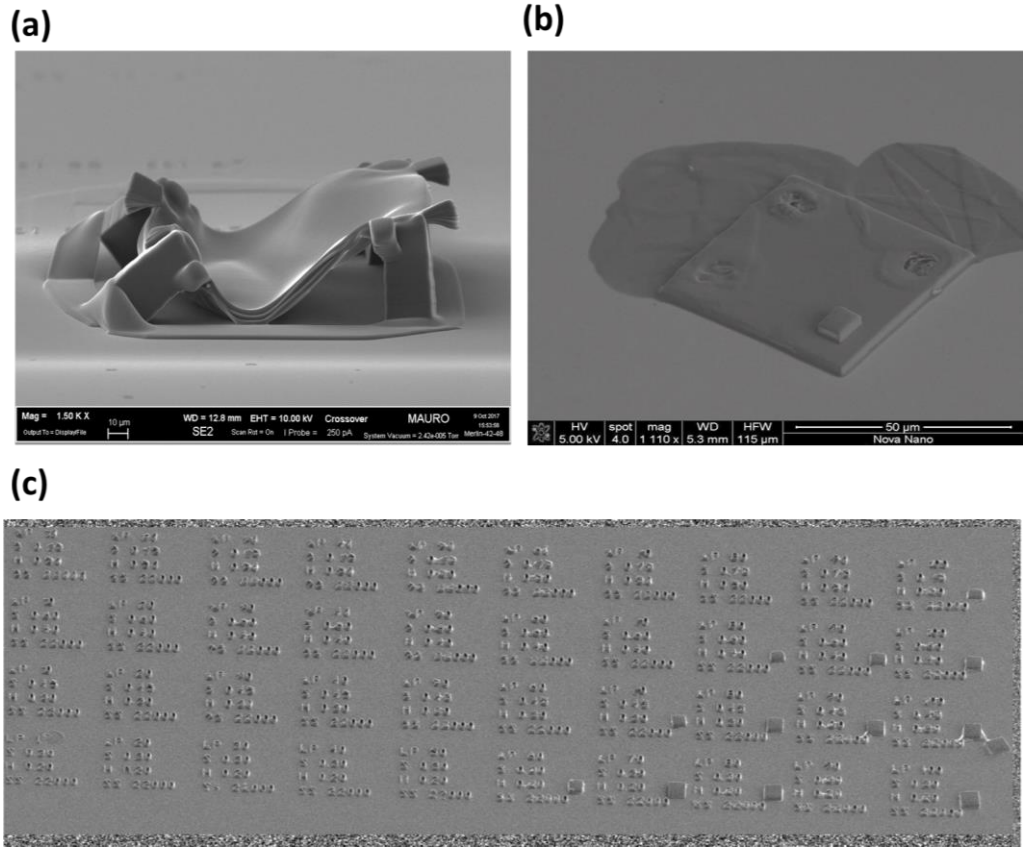

Figure 4.16: SEM images of (a) collapsed of the structures after the development; (b) bubble effect during the fabrication process; (c) dynamic range test.

After having found a proper dynamic range for our materials, we proceeded with the fabrication of the structures, with the following parameters: LP 100, SS 15000 µm/s, S 0.3 and H 0.1. Once fabricated, the sample were developed in

tetrahydrofuran (THF) by rinsing for 5 minutes. The final structures are suspended and stable membranes as shown in Figure 4.17.

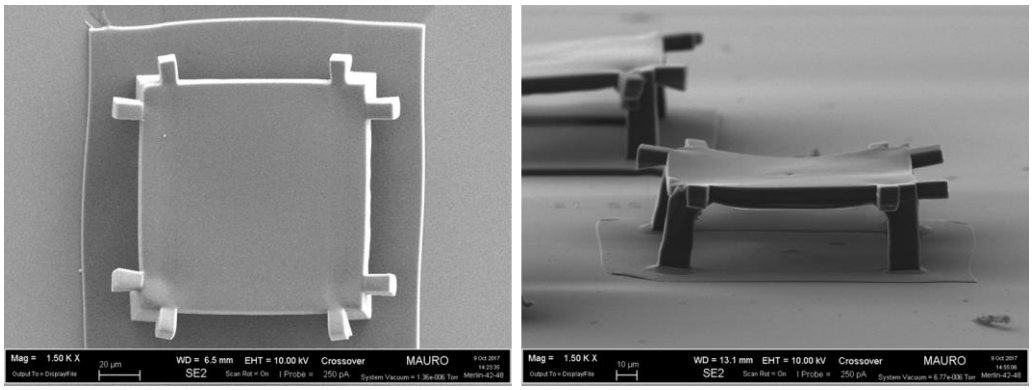

Figure 4.17: SEM images of stable 3D suspended membranes fabricated by two photon lithography.

Some possible issues from the fabrication process are the not uniform crosslinking of the material and the degradation of the azobenzene compound during the two photon polymerization. Therefore, to this aim Raman spectroscopy is employed to observe the crosslink level and its homogeneity across the suspended membranes and even the preservation of the azo. The graph in Figure 4.18a, exhibits the characteristics peaks of monomer, azopolymer and photoinitiator of the unpolymerized solution. As shown, the characteristic peak of the N double bound, typical of azopolymers, is located at ~1580 cm^{-1}. Subsequently, comparing the unpolymerized and polymerized spectra at different laser power (LP 60, LP 70 and LP 80), it is possible to confirm the preservation of the azo group and to define the specific level of crosslink for each configuration, with an average of 65% of crosslink, see Figure 4.18b. The homogeneity measurements were conducted by taking three points along the membranes and comparing the corresponding spectra. It is observed that the crosslink peak, located at ~1653 cm^{-1}, remained unchanged for each taken point, Figure 4.18c. As a consequence, the level of crosslink resulted to be the same in each part of the fabricated structure, confirming the homogeneity of the membrane in terms of polymerization of the material.

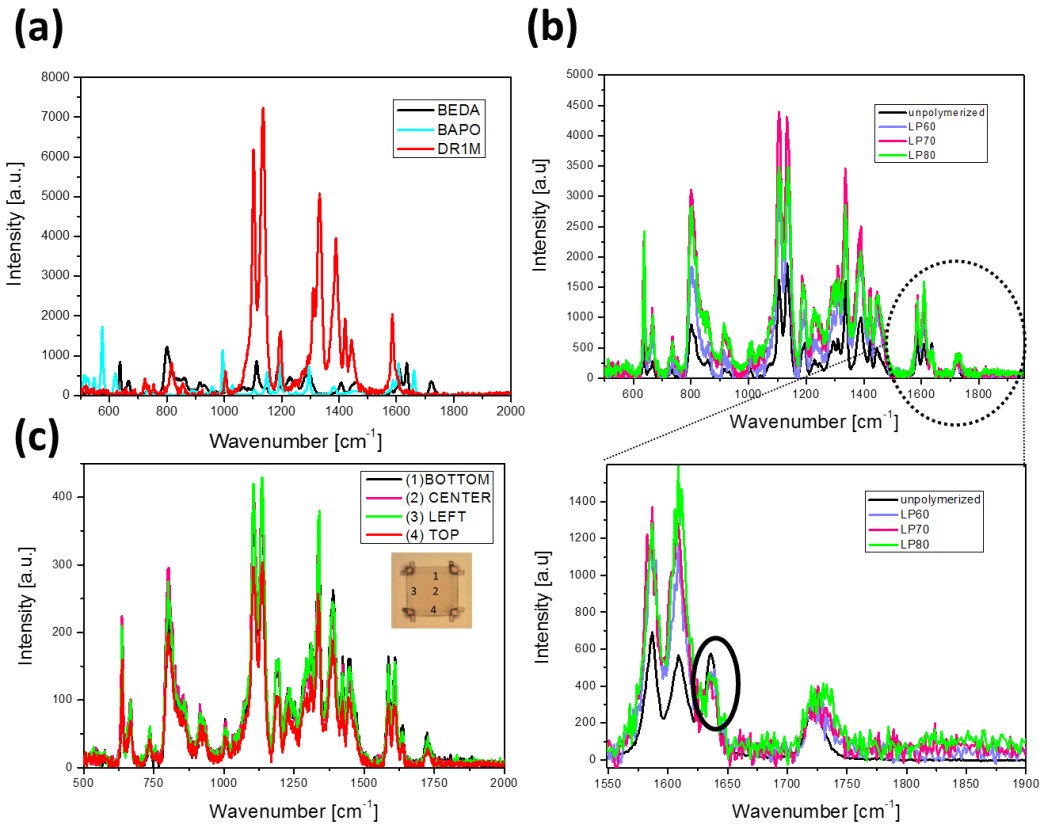

Figure 4.18: Raman Spectroscopy of (a) Reference spectra of the monomer (BEDA), azopolymer (DR1M) and photoinitiator (BAPO), (b) Unpolymerized and polymerized and (c) Spectrum in 4 different point of the membrane.

4.2.2 Photo-mechanical actuation based on suspended membranes

The experimental part is carried out by means of the interferometer set up described in chapter 4.1.1. Briefly, membranes are illuminated by a collimated beam (λ=633 nm). Transmitted light is collected by a NA=0.95 objective ad imaged (through a tube lens) onto the CMOS camera (Thorlabs DCC14p35M). A collimated reference beam is also hitting the camera, in such a way that images produced by the objective shows interference fringes. A piezo-driven mirror is shifting the optical path of the reference beam by steps of π/4. For each cycle consisting of 5 steps, the corresponding images are collected and processed in such a way that a phase image of the collected light is produced. Worth to recall here that the phase distribution refers to the light transmitted through the object.

When the membrane is slipped beneath the objective, the wavefront gets deformed. An exemplary phase distribution is shown in Figure 4.19a. As the phase is obtained by means of an inverse tangent operation, the phase values are limited to the range [-π,π], i.e. the phase is wrapped. In order to unwrap it, there are specific algorithms. A general problem of these algorithms is to specify an initial value of the phase, where the code starts to unwrap. As a result, different unwrapped phases might differ by phase offsets, see Figure 4.19b.

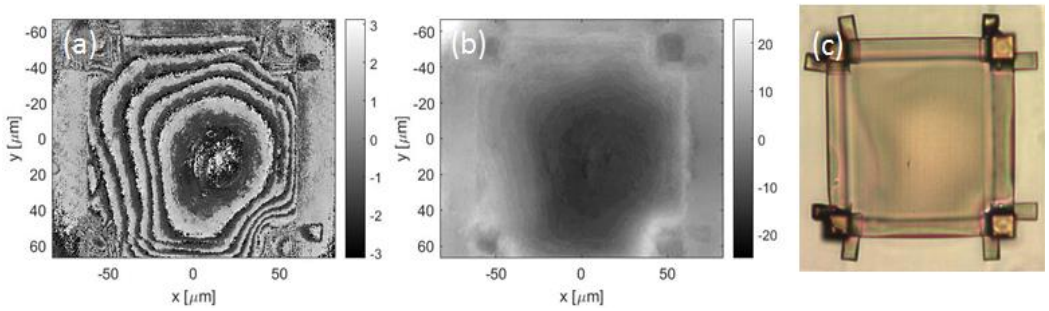

Figure 4.19: (a) wrapped and (b) unwrapped phase distribution (in radiant) of light transmitted through a 120 μm x 120 μm membrane (nominal thickness 4 μm); (c) phase contrast image revealing a membrane inhomogeneity according to the phase distribution as measured by the interferometer.

At first, we observed upon irradiation an expansion of the membrane. This is a rather typical behavior we found also on similar systems, including macro-membranes (few hundreds of micron thick) obtained by PDMS stamping and UV crosslinking (see Figure 4.12). If the membranes expand, the optical interferometer (operating in transmission) should detect an increase of thickness of the membrane. If the refractive index of the membrane would stay constant, the expansion would result in an increase of the phase delay accumulated by the light travelling through the membrane. Instead, we observe the opposite result (Figure 4.20).

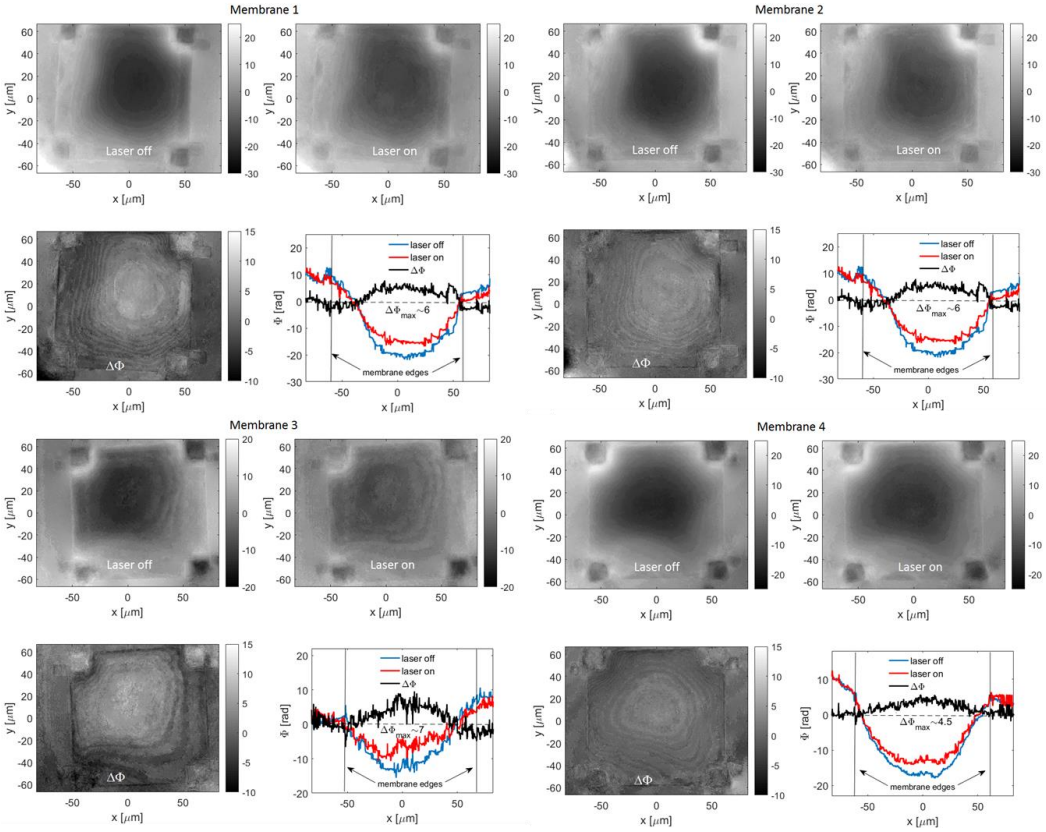

Figure 4.20: Unwrapped phases of four samples when the laser is on and off. The phase profile relates to a horizontal cross section passing through the center of the membrane.

Two important observations can be made: (1) the membranes are inhomogeneous in thickness. From the phase profiles measured in the laser-off condition, it is possible to evaluate the thickness variation from the external boundaries to the center. The range can be evaluated for instance from the profiles in Figure 4.20 by using the following formula:

$$\Delta t = \left| t_c - t_b \right| = \left| \Phi_c - \Phi_b \right| \cdot \frac{\lambda}{2\pi} \cdot \frac{1}{n_p - 1}$$

where n_p is the membrane refractive index (n_p=1.53) and λ=633 nm is the interferometer laser wavelength. This is confirmed by SEM images, as shown in Figure 4.21.

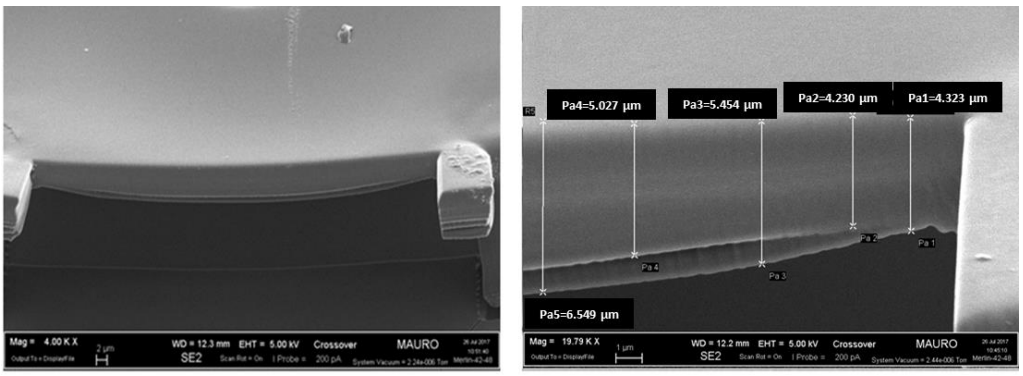

Figure 4.21: SEM images of membranes, and corresponding evaluation of thickness at the boundaries.

(2) When the laser is switched on, the unwrapped phase delay measured in the center (where the laser spot is hitting the sample) decreases, meaning that the optical path of light has reduced. This observation is in contrast to the hypothesis of a pure expansion of the membrane under laser irradiation. Therefore, such an expansion must be accompanied by a decrease of the membrane refractive index.

The phase difference ($\Delta\Phi$) as measured from the laser-off to the laser-on state depends upon both parameters, i.e. the polymer expansion and the refractive index change and it is not possible to decouple them without any additional measurements. Therefore, the observed $\Delta\Phi$ can be expressed in the following way:

$$\Delta\Phi(x,y)=\Phi_{ON}(x,y)-\Phi_{OFF}(x,y)=\frac{2\pi}{\lambda}\cdot(n_p-\Delta n-1)\cdot\left(1+\frac{\Delta t(x,y)}{t(x,y)}\right)t(x,y)$$

For simplicity, we restrict our analysis to the membrane location where the maximum phase variation occurs, such that

$$\Delta\Phi_{MAX}=\Phi_{ON}-\Phi_{OFF}=\frac{2\pi}{\lambda}\cdot(n_p-\Delta n-1)\cdot\left(1+\frac{\Delta t}{t}\right)t$$

In order to evaluate Δn and Δt, it is also required an estimation of t, i.e. the thickness in the location corresponding to $\Delta\Phi_{MAX}$. This is done by assuming that the actual thickness of the membranes is described by the phase profile Φ_{OFF} (x,y)

as measured in the laser-off state. Therefore, assuming a thickness value t_0=4 μm at the membrane edges (from design and SEM images, see Figure 4.21), we obtain:

$$t(x,y) = t_0 + \Delta\Phi_{shape}\frac{\lambda}{2\pi}\cdot\frac{1}{n_p - 1}$$

where $\Delta\Phi_{shape}$ is the phase variation from the edge of the membrane to the point where $\Delta\Phi_{MAX}$ occurs during laser irradiation (i.e. close to the membrane center).

With this assumption, the expression for to $\Delta\Phi_{MAX}$ depends upon Δn and Δt/t, both unknown. That means that there are several combinations of Δn and Δt/t resulting in the very same value for measured $\Delta\Phi_{MAX}$, as shown in Figure 4.22.

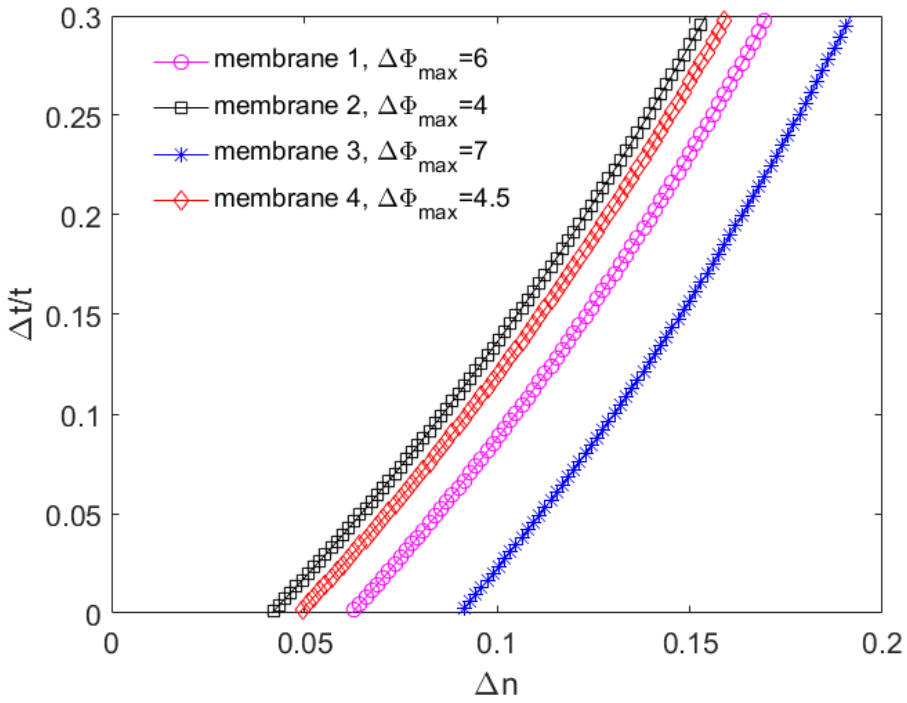

Figure 4.22: Curves Δt/t(Δn) for each one of the 4 considered membranes. Along each curve, the observed $\Delta\Phi_{MAX}$ during laser irradiation is constant.

From Figure 4.22, we can readily see that it would not be possible to have any positive value of $\Delta\Phi_{MAX}$ by invoking an expansion only (and no decrease of the refractive index). Furthermore, it is noticeable that the more the extent of the expansion is, the more the refractive index drops.

It is indeed possible to separately evaluate the polymer expansion by looking at edge displacement during irradiation. An accurate image analysis allows to evaluate the amount of such a displacement, as shown in Figure 4.23.

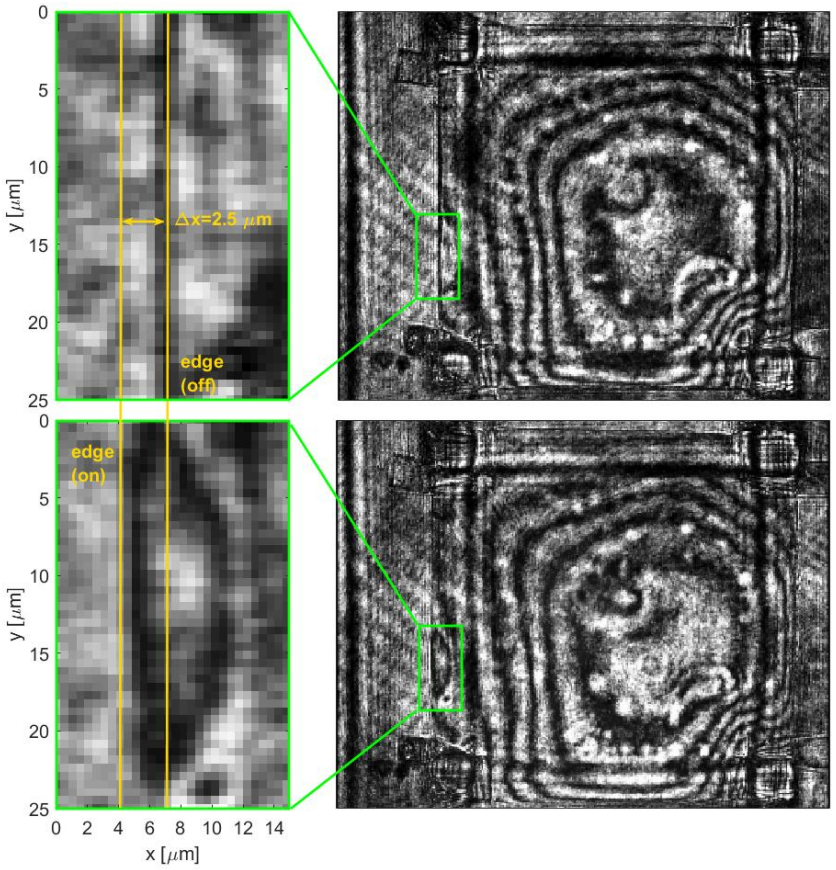

Figure 4.23: Evaluation of the right edge displacement of membrane 1 during laser irradiation based on interferograms analysis.

As the expansion is isotropic and certainly symmetrical over the membrane plane, a total expansion $\Delta t = 2 \cdot 2.5\ \mu m = 5\ \mu m$ is observed when the laser is switched on. In order to infer an intensive $\Delta t/t$ (i.e. the amount of linear expansion divided by the total length affected by expansion) it is indeed necessary to have a knowledge of the surface extension of the laser beam hitting the membrane. To this end, it is useful to evaluate the white light image presented in Figure 4.24.

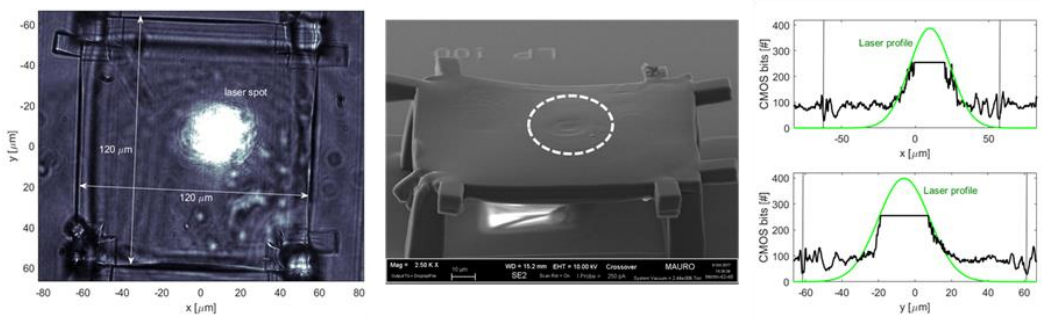

Figure 4.24: White light image and corresponding SEM of a membrane and the illuminating area. Because of the camera saturation, it is not possible to explicitly appreciate the laser intensity profile. However, since the laser is a focused Gaussian beam, we can infer the actual shape of the laser as the Gaussian profile g(x) plotted as a solid green line.

The Gaussian intensity of the laser g(x) provides a sort of weighting function for all the polymer portions of the membrane participating to the light-induced expansion. By neglecting the thickness of the membrane here, we can built a model whereby, for a given maximum value of Δt/t, the overall deformation Δt along one direction is simply given by:

$$\Delta t = \int g(x) \cdot \frac{\Delta t}{t} dx$$

meaning that all the points irradiated by the Gaussian beam are expanding according to the function g(x)·Δt/t. The integral above can be easily calculated for several values of Δt/t. The corresponding Δt is shown in Figure 4.25, below. It is possible to see that in order to obtain an overall linear expansion of 5 μm (as estimated from Figure 4.23), a Δt/t=0.141 is required, see Figure 4.25.

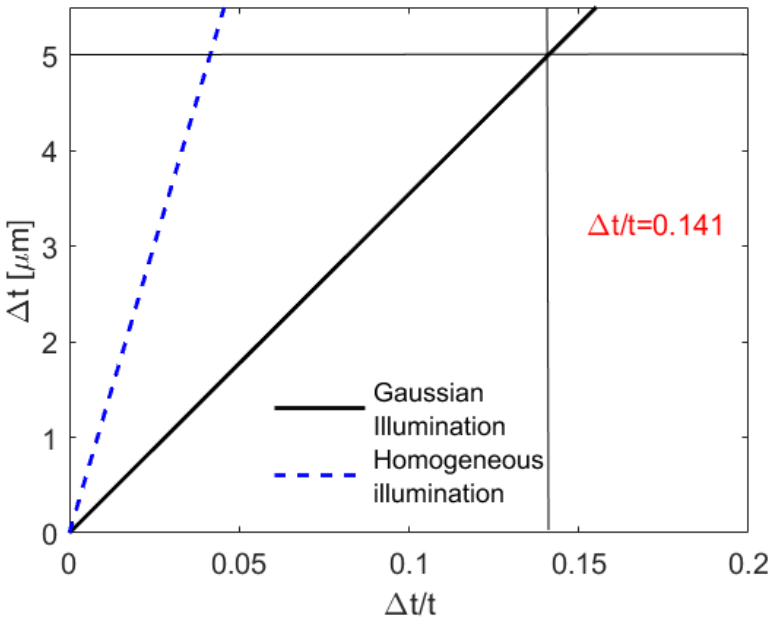

Figure 4.25: Linear (lateral) expansion Δt of the membrane upon homogeneous of Gaussian illumination as a function of Δt/t.

To conclude, the value for Δt/t=0.141 refers to membrane 1 only (see Figure 4.19). However, by going back to Figure 4.22, it is now possible to provide a separate estimate also for the refractive index variation Δn, resulting in Δn=0.12. So, the light-induced photo-transduction is studied starting from the isotropic expansion of the membrane's edge. Therefore, we deduced the amount of linear expansion divided by the total length affected by the expansion and also the refractive index variation induced by light is estimated.

5

Azopolymeric platform for cell conditioning

Azobenzene-containing polymers offer numerous advantages and opportunities over other stimuli-responsive materials to interface with biology. Understanding cellular reaction and response to the external environment is a central aspect in diverse biomedical, bioengineering, and clinical applications. It is well-known that cell functions and fate are largely dependent on a surrounding microenvironment consisting of other cells, extracellular matrix (ECM), soluble factors, growth factors and cytokines [161]. The effect of the ECM on cells is the most challenging phenomenon to study as the ECM is a dynamic and complex protein meshwork. Research in this field suggests that composition [162,163], pore size [164], stiffness [165,166] and nano- and micro-topography [167,168] of a material surrounding can affect the cell behavior. Cells can sense these ECM cues and the cells' behavior in sense of adhesion, polarization, proliferation, differentiation, migration, etc. can be influenced. The interaction of the ECM with cells was widely studied in the past two decades through two-dimensional (2D) or three-dimensional (3D) nano- and micro-patterning of materials and recently also dynamic platforms for cell-material interaction have attracted significant interest [169,170]. The goal is to mimic the interplay between a cell and surrounding environment taking place in vivo, where the ECM continuously changes its biochemical and biophysical features due to ageing, morphogenetic events or diseases [171]. A simulation of natural processes happening in the ECM, can be realized with the help of biocompatible stimuli-responsive materials [172]. Artificial scaffolds created from such materials can serve as platforms for dynamic in situ modifications and thus enable live observation of cell-material interactions.

Exploiting the photoresponsive behavior of an azopolymeric substrate we emphasize the high sensitivity that cells display toward the chemical and physical features of the platform to which they are connected. In particular, such features proved to affect different aspects of cell behavior like attachment, spreading, differentiation, and ultimately cell fate [173,174]. These cell actions can be

influenced by different types of signals displayed by the material substrate, such as biochemical, mechanical, and topographical signals [175,176]. Topographic cues are known ply a potent influence on cell fate and functions, and many techniques were developed to fabricate micro- and nanogrooved materials to study contact guidance and mechanotransduction phenomena. The pioneering work in this area showed a cell spreading over a micro-patterned surface and concluded the importance of a contact area between the cell and the ECM for cell growth and apoptosis (programmed cell death) [177]. Ever since, more studies concerning the cellular response to micro- as well as nanopatterned surfaces are carried out, with the most investigated patterns being grooves, grids and pillars [178,179].

The micro-sized ridge and groove patterns are reported to induce cell alignment, migration velocity, stretching and differentiation [180]. Figure 5.1 shows human umbilical vein endothelial cells (HUVECs) elongated according to the groove direction of a linearly grated structure. Majority of the cell types tend to align along with the major axis of the pattern and exhibit increase in their migration velocity. The velocity also tends to increase with the decreasing groove spacing [181]. The speed of the cell migration is also shown to increase in the case of interaction with the grid structures [182,183].

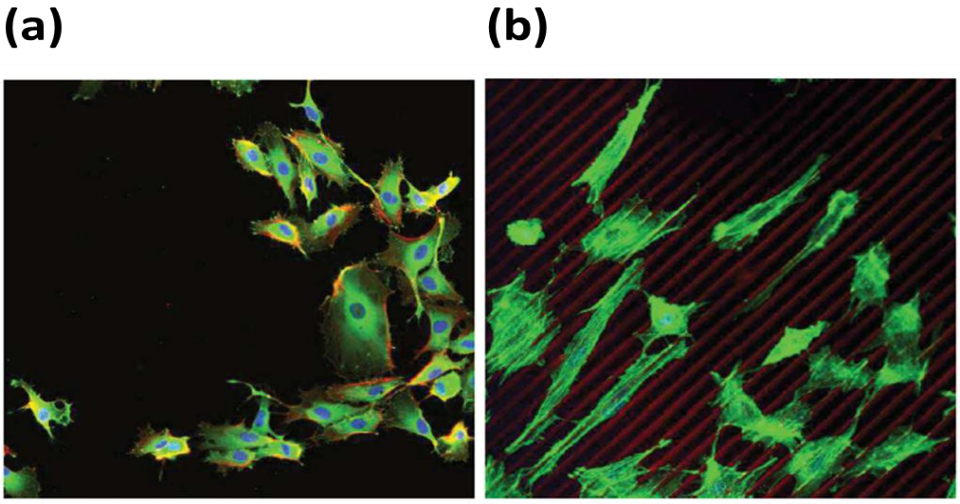

Figure 5.1: Human umbilical vein endothelial cells (HUVECs). (a) The cells on the flat surface exhibit random orientation of the elongation; (b) The cells on the linearly grated structure are elongated according to the groove direction.

Here we propose, a light-responsive poly(disperse red 1 methacrylate) (pDR1M) azopolymeric pillars-like pattern as an active and biocompatible platform

for dynamic material-cell interaction observation in 2D environment. After a proper cell seeding, a pattern deformation in different shape (linear, circular, azimuthal and so on) are performed by a holographic optical conditioning by means a Spatial Light Modulator (SLM). The aim of the experiments is to observe by time-lapse acquisitions and by a proper cell-tracking, how the cell behaves according to the modification of the surrounding environments.

pDR1M dissolved at 2 wt.% in N,N-Dimethylformamide (DMF) is firstly structured in an array of micro-pillars by soft imprinting lithography following the same procedure described in the subsection 3.2.1, by means of a PDMS stamp from the Si master drawn in Figure 3.4. The fabricated micro-pillar structure presents various period (λ) between the four arrays, respectively 5 µm (a1), 7 µm (b1), 9 µm (a2) and 11 µm (b2). In the experiments, the most used microstructures corresponding to the a2 array, see Figure 5.2.

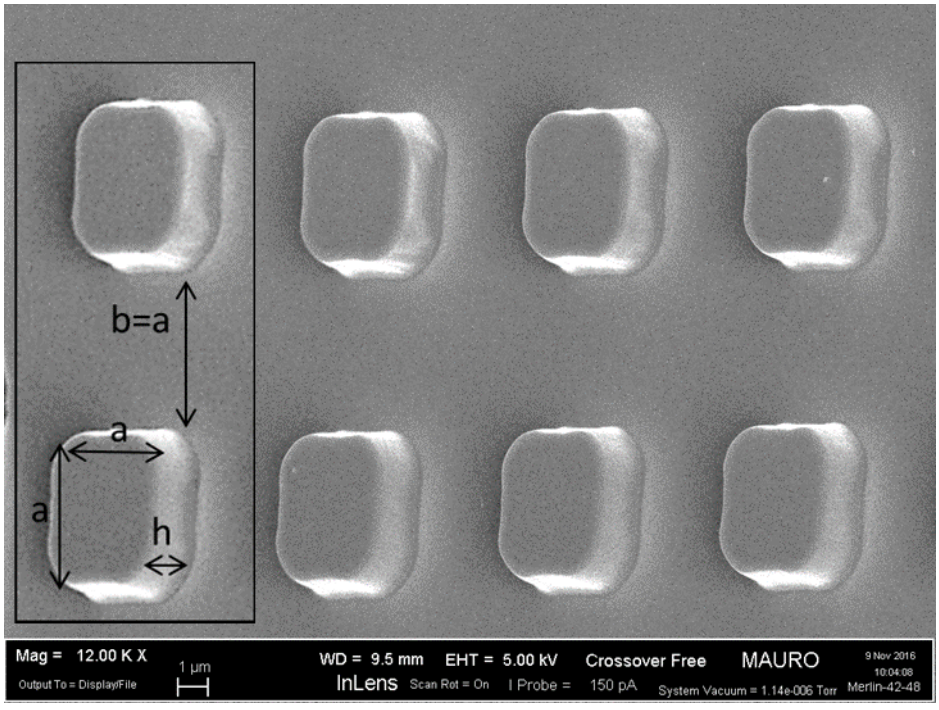

Figure 5.2: SEM images of the 2 micro-pillar structure array from pDR1M fabricated on a glass cover slip, where a=b= 4.5µm, h=1 µm (a=pillar side, h=pillar height and b=pillars interdistance).

The azopolymeric microstructures are modified by linearly polarized laser beam. For dynamic topographic modification experiments, an optical setup is designed and constructed, including a software for a direct laser irradiation control, an image acquisition and a subsequent image processing. The optical setup is capable of an adaptive illumination with a linearly polarized laser beam, which intensity pattern is modified to fit a geometry of a specific cell attached to the substrate. The optical setup with all the software should serve as a 2D system for observation of a directed migration of cells attached to micro-patterned light responsive materials while exposed to various dynamic topographic modifications. The technique proposed in this study enables the development of synthetic platforms that finely control cell orientation and migration both in time and space by polarized-light irradiation in situ during cell culture.

5.1 Primary cell line and subculturing on azopolymeric substrates

A primary cell line corresponds to the one extracted directly from a living tissue and established to growth in vitro for a period of time, which is always limited with cells dying after several cycles of cell subculturing. Subculturing (or passaging) of adherent cells refers to a removal of medium, detachment of the cells from a previous container and transferring part of the cell population to a new container (flask/Petri dish) with an addition of fresh growth medium. Passaging the cells according to a strict schedule is vital for maintaining a healthy cell line with a reproducible behavior. Cells in a culture undergo different live phases (see Figure 5.3a), from the lag phase to the log phase, where proliferation of the cells is exponential. In this phase, the cells should be passaged (before entering the stationary phase) to ensure enough of free space and medium nutrients for further proliferation and growth of the cells [184]. The first human cell line ever established was the HeLa in 1952 followed by breast cancer cell line BT-20 in 1958. Ever since more breast cancer cell lines were established with the MCF-7 type being the most widely used [185]. The cell line used for the experiments in the present work is a culture of primary breast cancer cells MDA-MB-231 obtained directly at Candiolo Cancer Institute (IRCCS), where also the cell culturing procedures are carried out. MDA-MB-231 cell line was established in 1973 [186], and is a metastatic adherent cell type, which is reported to grow rapidly in vitro forming loose networks of spindle-shaped cells (see Figure 5.3b). Is must be transferred every 5-8 days with

dilution rates around 1:10. The cell line of adherent human breast cancer cells (MDA-MB-231) used for the experiments is handled according to the standard protocols as described in Cell Culture Basics Handbook published by Thermo Fisher Scientific [187] to successfully preserve the cell line throughout the whole period of the project work.

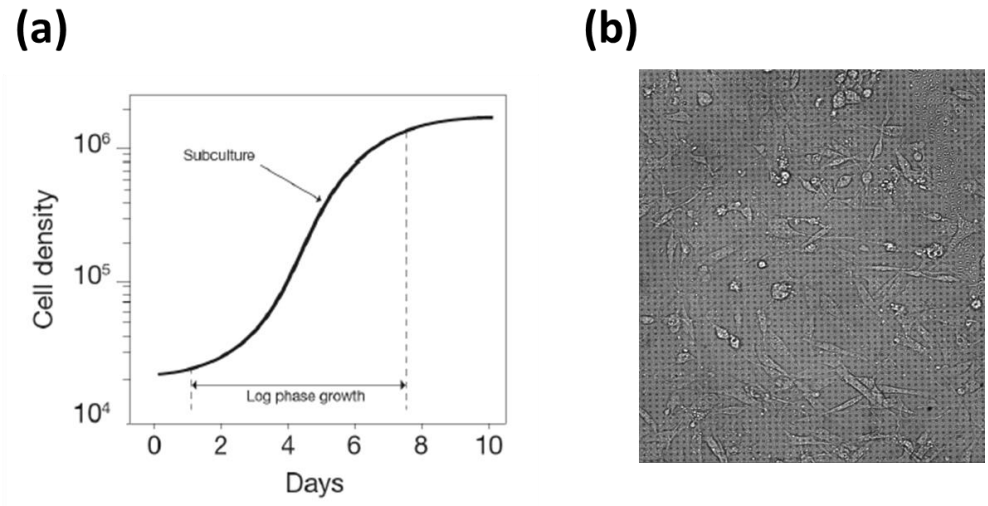

Figure 5.3: (a) Semi-logarithmic plot showing cell density of a cell culture versus time. After the initial lag phase when the cells are adjusting to a new environment, fast growth and proliferation (exponential) begins; (b) Human breast cancer cells MDA-MB-231.

450 ml of the Dulbecco's Modified Eagle's Medium mixed with 50 ml of Fetal Bovine Serum, 5 ml of L-Glutamine solution and 10 ml of Penicillin-Streptomycin are used as solution medium for cell growth.

The aim of the work is to test the deformability of the substrate and its effectiveness in altering the adhesion and migration of prototype cells. So MDA-MB-231 are extremely aggressive cells, with classical mutations from metastatic tumor resistant to the treatments, and above all mesenchymal, they behave in individual way, so every cell is per se. The type of migration is a classified as mesenchymal / individual migration. In addition to this, breast cancer is an example in which the invasiveness and the ability to migrate is relevant from a clinical point of view. The work dealing with the cells cultures consisted of two main tasks, regular cell passaging of the cell line and seeding of the cells on the prepared samples with micro-pillar structures from pDR1M.

5.1.1 Subculturing (Passaging) of the MDA-MB-231 Cells

The MDA-MB-231 cell line is passaged once a week with different split ratios, according to the actual requirements. The cell culture is always stored in a Petri dish (100 mm diameter) placed into an incubator to maintain the optimal cell growth conditions (37°C; 5% CO2; 95% humidity). In the first step of a cell passaging procedure, the cell culture is removed from the incubator and its viability was checked by means of an optical microscope. Possible traces of contamination are checked and the splitting ratio was determined by analyzing the surface percentage covered by the cells. For a higher coverage, a higher splitting ratio of the cell passaging is used. The ratio of the number of cells in the dish after and before the passaging varied between 1:3 and 1:12. After the splitting ratio is determined, the total volume of the growth medium is aspirated from the dish and the cell culture is washed two times with 5 ml of Phosphate Buffered Saline (PBS) and finally 1 ml of trypsin solution was added. Trypsin caused detachment of the strongly adherent MDA-MB-231 cells by enzymatic dissociation of the cells from the substrate. After 5 min of incubation, the Petri is removed and gently shaked to further stimulate the detachment of still adhered cells and splitting of cell clusters. The process of proteolysis, activated by the trypsin, is stopped by addition of the fresh growth medium according to the previously determined splitting ratio. Sterile Petri dishes are filled with 8 ml of a solution formed by the passaged cells and fresh growth medium.

5.1.2 Seeding of the MDA-MB-231 Cells on the pDR1M micro-pillars

For the experiments studying cell behavior on structured surface, the micro-pillar structures from pDR1M are fabricated directly on a Petri dish with a glass bottom. Before cells seeding, the Petri dish is sterilized for 5 min in 75% ethanol and then washed two times with PBS. To obtain detached cells for further seeding, an experimental procedure identical to the cell passaging is carried out at first. Once the cells are detached from the original Petri dish, Bürker counting chamber is used to measure the number of cells per ml. After couple of experiments, 5.10^4 of cells per one Petri dish (diameter 30 mm) showed to be an appropriate density of the cells for further observations of a cell behavior on a structured surface. The volume of the solution containing 5.10^4 of cells is calculated and seeded in the Petri dish with the fabricated micro-pillar structure and then it is topped up with fresh growth medium to the total volume of 5 ml. The Petri dish with the seeded cells is placed

into an incubator for 48 hours to ensure that the cells would adhere to the surface strongly enough to survive the transport and in the next days. Just before the transport, 0.5 M HEPES solution is added to the sample (1:20 dilution rate) to stabilize pH of the solution. Then, the sample is placed into an incubator for another 24 hours to restore the cell attachment to the surface, in order to have the pDR1M micro-pillar structures with seeded MDA-MB-231 cells prepared for further experiments.

5.1.3 Preliminary test on the linear elongated micro-pillars structure

As initial test, we first assessed the capability of cells to recognize and respond to a different type of the pattern, by first deforming the substrate and then we seeded the cells on the elongated substrate. So, pDR1M micro-pillar structured surface is illuminated with the linearly polarized laser beam (half of the sample region, see Figure 5.4) in order to obtain an elongation of the pillars according to the direction of the polarization. As second step, the whole substrate (both the deformed and not-deformed area, related to micro-pillar array a1 with 9 μm periodicity), is then seeded with the MDA-MB-231 cells (described in the Chapter 6.1.2). Initially, cells are randomly oriented and displayed a broad distribution of orientations on both patterns (deformed and not deformed).

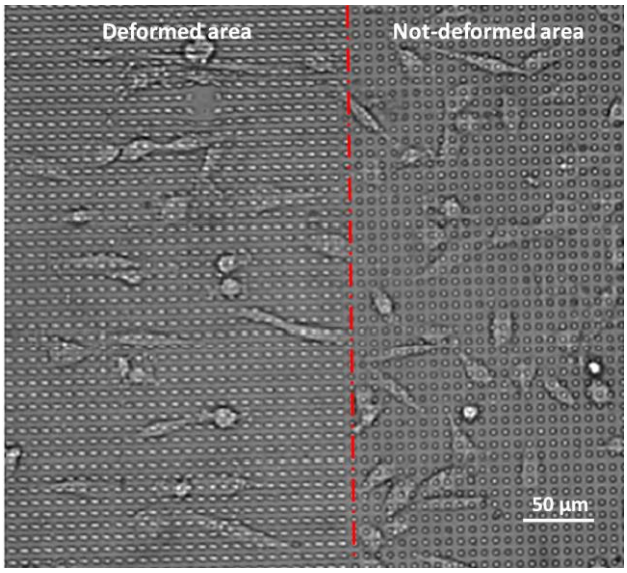

Figure 5.4: Micropillar structured pDR1M surface with the seeded MDA-MB-231 cells. Half of the sample area (left) is elongated by linearly polarized laser beam, prior to the cell seeding.

After 18 hours, what we observed was that the cells in the deformed area, acquired a higher level of elongation respect the others in the non-deformed area, showing an isotropic alignment along the patterns direction of the shape modification. The cells migrated randomly on the surface with the not elongated micro-pillars, while on the surface with the deformed micro-pillars, cells tended to move along the main axis of the elongation, see Figure 5.4.

5.1.4 Analysis with a Spinning Disk Confocal Microscope

A spinning disk confocal microscope (Nikon Eclipse Ti Spinning Disk) is used to observed the elongated shape of the MDA-MB-231 cells attached on the structured pDR1M substrate. The cells are stained with Phalloidin and 4',6-Diamidine-2'-phenylindole Dihydrochloride (DAPI), according to the following procedure. Firstly, all amount of the growth medium in the structured Petri dish is aspirated and 1 ml of a paraformaldehyde solution (4% in PBS) is then added to the dish and left for 10 min at room temperature. Afterwards, the solution is removed and the sample is washed two times with PBS. In the second step, 1 ml of 50 mM ammonium chloride solution is added to remove the residual aldehydes from the sample and then the dish is again washed two times with PBS. Then, 1 ml of the solution of triton (0.2% in PBS) is added to the Petri dish, to allow phalloidin and DAPI to penetrate into the cells. The solution is removed after 10 min followed by further washing with PBS (two times). Finally, 2 ml of a solution of phalloidin in PBS (100x dilution) is added to the dish (staining of the cell structure). After 15 min, the phalloidin solution is aspirated and 2 ml of a solution of DAPI in PBS (1000x diluted) is added (staining of the cell nucleus). After 5 min the solution is then removed and the sample is washed with PBS for two times. After that, the dish is filled with PBS and stored in refrigerator before the investigation under the confocal microscope. Figure 5.5, shows a 3D visualization of the cell attached to the linear elongated micropillar structure (period of the pillars 5 μm).

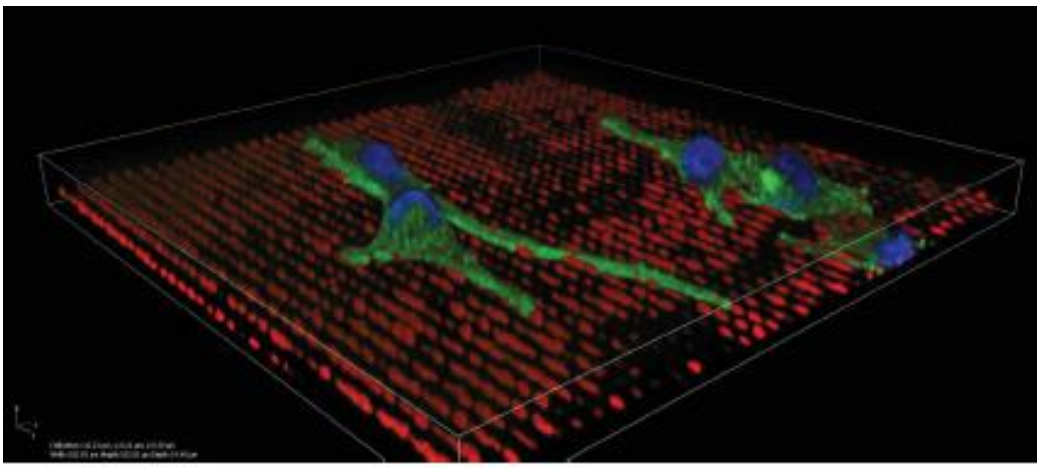

Figure 5.5: 3D visualization with a spinning disk confocal microscope of the MDA-MB-231 cells (green body of the cell, blue nucleus) attached to an elongated micro-pillar structure made of pDR1M (red). The spacing of the pillars is 5 μm.

Some of the filopodia of the cells are highly stretched in the direction of the micro-pillar elongation. It shows the cell intention to move in direction of the micro-pillar elongation.

5.2 Optical conditioning system for the *in situ* adaptive laser irradiation

The main challenge of this work was to study how the cells behave in response to topographic changes of the underlying substrate. To this aim, we built an optical system able to perform a dynamic and tunable topographic modification of the azopolymeric pattern with cells on board, and it is capable of direct irradiated the sample with a linearly polarized laser beam projecting an intensity image with a micro-scale resolution. The idea is to "adapt" the irradiation according to the cell shape, in such a way that we are able to irradiated only close to the cell, preserving the cell during the deformation process of the surrounding pillars. According to this approach, irradiating by using a suitable illumination mask, we want to "capture" the cell by deforming only the area around the cell, and the outcome is to study migration and behavior of the cell from the not-deformed area to the deformed pillars. We want to demonstrated that cell morphology and trajectory can be both

controlled in vivo and remotely with a laser light, simply by playing with optical intensity, polarization and projected cell shape-like pattern. Such a system enables to specifically deform a cells environment by projecting a doughnut-shaped intensity pattern precisely centered on the selected cell and testing how the cell behave according the surrounding modifications. The optical conditioning setup is shown in Figure5.6

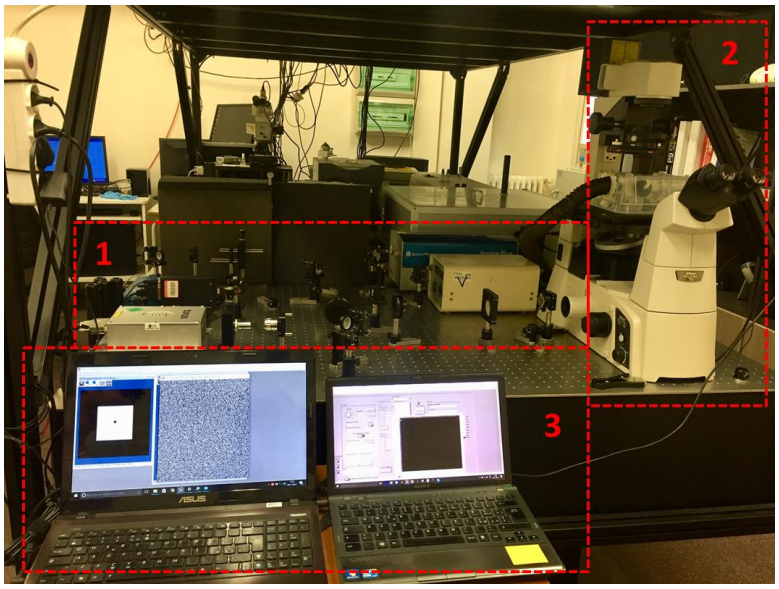

Figure 5.6: Holographic optical conditioning built up in our laboratory.

It consists of three main modules: (1) optical setup for beam shaping (intensity image), (2) acquisition system, coupling the optical setup with an inverted microscope (live observation of the sample) and (3) control algorithms (beam shaping, live and time-lapse image acquisition), as shown in Figure 5.6.

The home-made setup for an *in situ* deformation of pre-patterned micro-pillar structures with presence of living cells on its surface is shown in Figure 5.7.

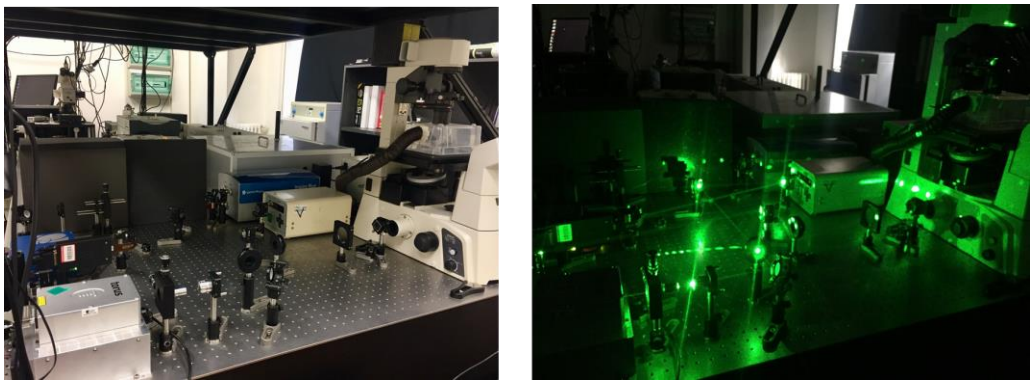

Figure 5.7: Home-made setup for an *in situ* deformation.

A conventional inverted microscope is employed for time-lapse observations in bright field. A laser pattern is input in the microscopy through a lateral port, then projected onto the azopolymeric structure on the bottom of the Petri dish by means of the collection objective (either 10x or 20x magnification). The laser pattern is obtained by illuminating a Spatial Light Modulator (SLM) with a well-collimated expanded TEM_{00} beam from a Nd:YAG doubled frequency source (Torus, Laser Quantum). The SLM (SLM – Pluto VIS006c, Holoeye) is able to provide arbitrary wavefront shaping of light at the first order of diffraction [189], according a user-defined phase distribution. The phase distribution can be calculated from any grayscale images by means of well-known algorithms from Computer Generated Holograms technology (e.g. the Gerchberg–Saxton algorithm) [190]. In such a way, arbitrary intensity distributions can be obtained as illumination patterns of the azopolymeric structures.

The acquisition system, illustrated in Figure 5.8, is constituted by an inverted microscope (Nikon Eclipse Ti-S), 24-bit CCD camera (Apogee Ascent) connected to a computer and self-made incubator ensuring the temperature control of the sample with living cells.

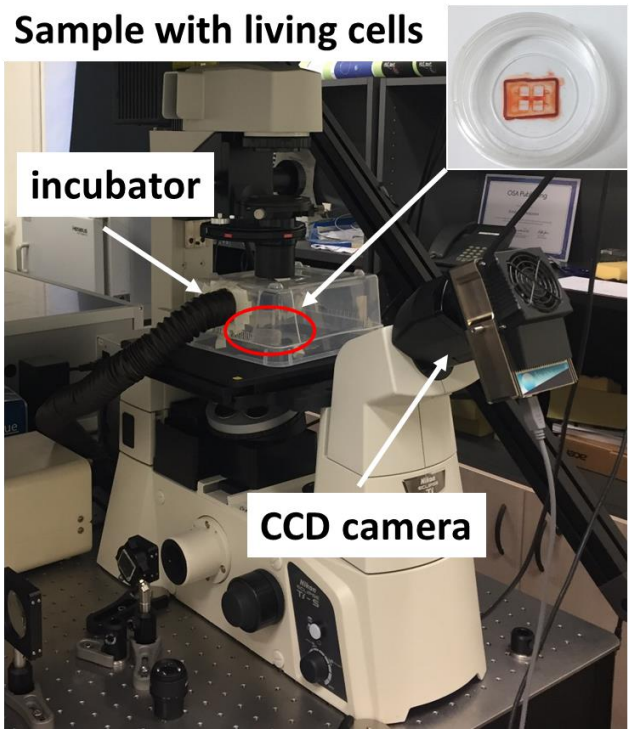

Figure 5.8: Acquisition system.

The control program, see Figure 5.9, for beam shaping and acquisition functions (live image acquisition and time-lapse experiment) was home- made designed in LabVIEW software (National Instruments).

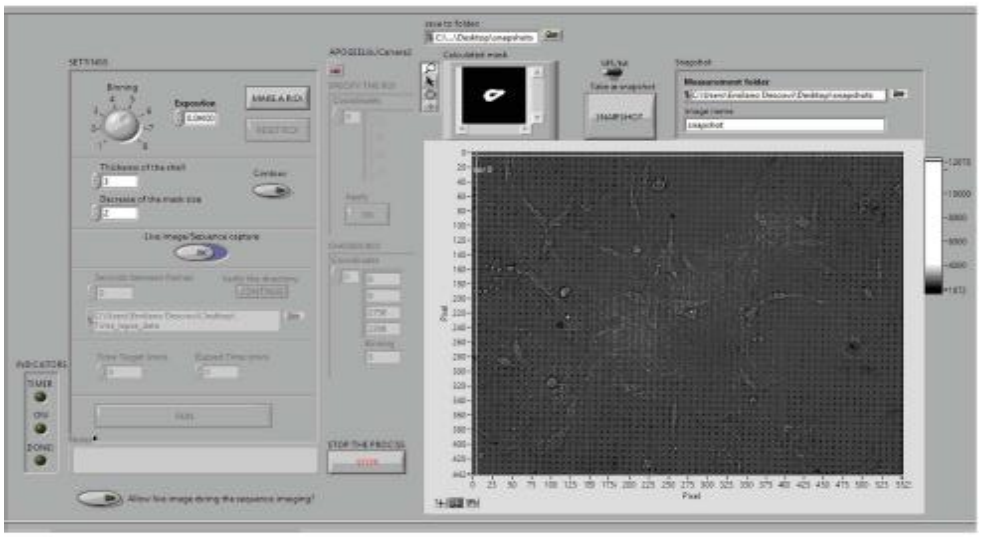

Figure 5.9: The front panel of the main program developed in the LabVIEW software responsible for the adaptive mask creation, the image acquisition and the phase image calculation.

A Petri dish with MDA-MB-231 cells seeded on the micro-pillar structured pDR1M surface (fabricated on the bottom of the dish) is placed under the microscope and covered with the self-made incubator for the temperature control set at 37°C. The LabVIEW program provide the live acquisition mode, a proper adjustments of exposition, binning and ROI (Region of Interest) selection. A single cell, fully attached to the sample surface (preferentially with no other cells in its proximity), is chosen and positioned to the middle of the cameras field of view. The mask creation function is activated and a contour can manually draw around the selected cell. The phase image for the SLM is automatically calculated and the laser beam is shaped by the SLM, in order to accurately project the intensity image around the selected cell, by eventually introducing an additional vertical, horizontal or axial tilt to the phase image on the display of the SLM. Once the laser beam was successfully shaped into the predefined shape and size, the illumination with the higher intensity for the specific deformation of the micro-pillars forming the sample is carried out. Illumination time and laser intensity are adjusted depending on the region on the sample and the desired degree of the pillar deformation (illumination time 5 min, laser intensity 100 % of the maximum laser power (750 mW)).

The irradiation process is considered to be successful when pillars in the vicinity of the selected cell were regularly elongated and it is possible to differentiate between the elongated and non-deformed regions. After the deformation, a time-lapse experiment is performed (20 hours, image acquisition every 2 minutes). Figure 5.10 shows two steps of the adaptive illumination procedure: the alignment of the laser intensity image with the selected cell and a region of deformed micro-pillars around the cell after the illumination process. The goal is to finely tune the specific deformation of the sample surface. The shape formed by the elongated micro-pillars on the sample surface should as closely as possible resemble the shape of the mask created from the drawn cell contour. The deformation of the elongated micro-pillars is required to be in the desired direction (corresponding to the laser beam polarization) and clear border between the elongated and non-elongated micro-pillar area is also required.

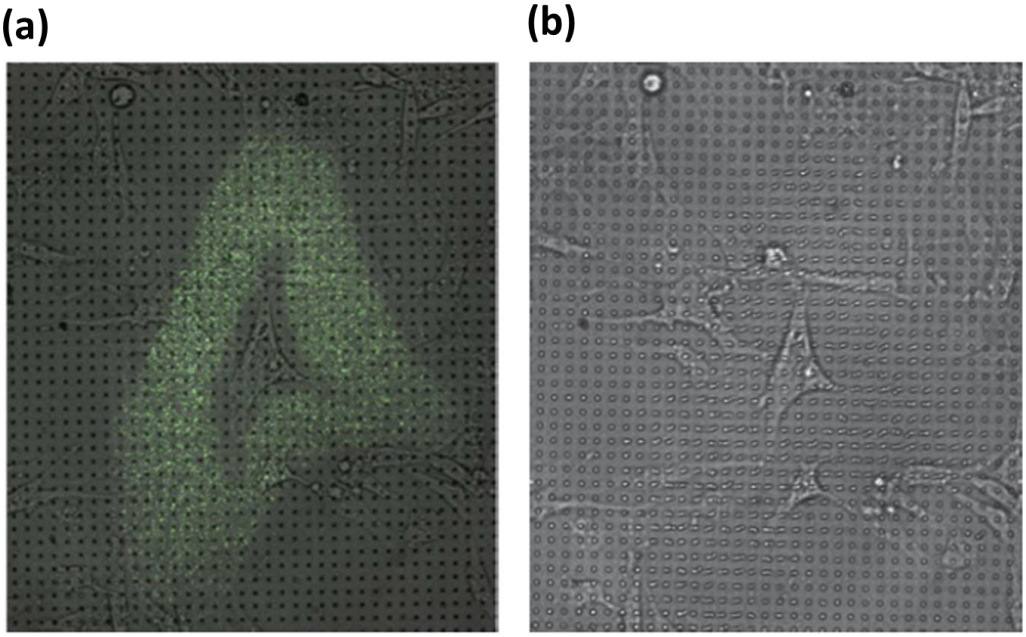

Figure 5.10: Steps of the adaptive illumination with the linearly polarized laser beam of the pDR1m micropillar structured sample and seeded with MDA-MB- 231 cells. (a) The image of the original, non-deformed, sample overlaid with an image of the shaped laser beam to clarify the illumination procedure, (b) sample surface after the laser illumination causing an oriented deformation of the micro-pillars surrounding the cell, according to the projected pattern.

Figure 5.11 shows how an azimuthal grating can be inscribed in presence of living cells. The azimuthal deformation is obtained by means of a proper Liquid Crystal cell, able to convert a linearly polarized beam into either a radially or azimuthally polarized beam, based on a well-known technology (see e.g. Arcoptix, Neuchatel, CH).

As shown in this example, exposure to laser light did not affect cell viability and motility. In fact, after 20-hours time-lapse experiments, as shown in the last frames of image sequences, the cells migrate towards the deformed pattern assuming a semicircular spreading, following the elongation of the grating.

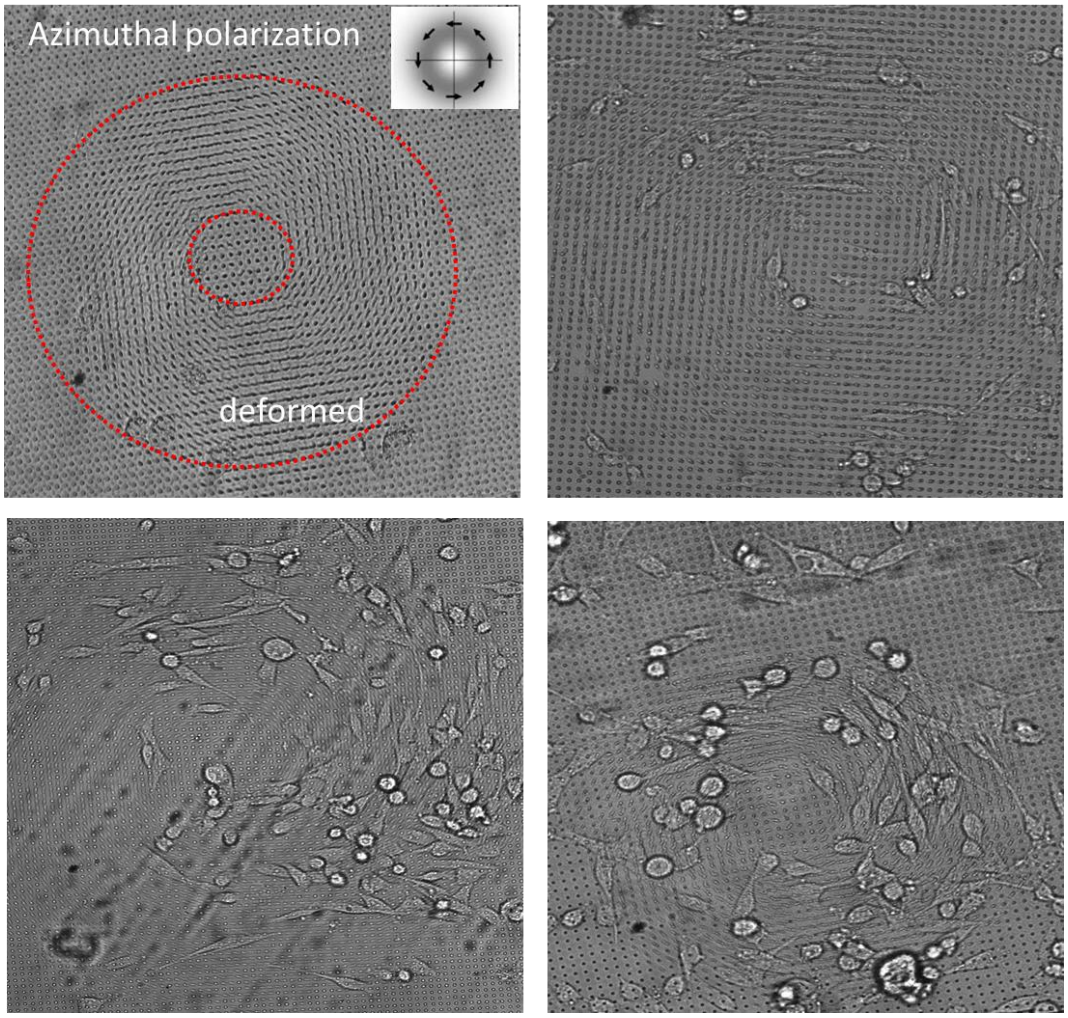

Figure 5.11: Optical microscope images of the adaptive pattern and subsequent cells migration according the deforming pattern after 20-hours-time lapse image acquisition.

In order to quantify the overall movement of the cells on the structured surface and to track the cells displacements, an image-sequence evaluation program is necessary to be developed. There are, however, some issues during the automatic analysis of the cell movement. The most significant one is the contrast - in many cases the contrast is higher on the edges of the micro-pillars rather than on the cell borders, and is difficult to distinguish the cells from the pillars. Thus, tracking of some of the cells is not always successful. Other problems arise when few cells overlapped and when cell detached from the surface or go in apoptosis. The idea is to implemented the tracking process in order to overcame such issues. As very

preliminary tests, the first results from tracking the cell behaviors related to different patterns and light polarization are shown in Figure 5.12.

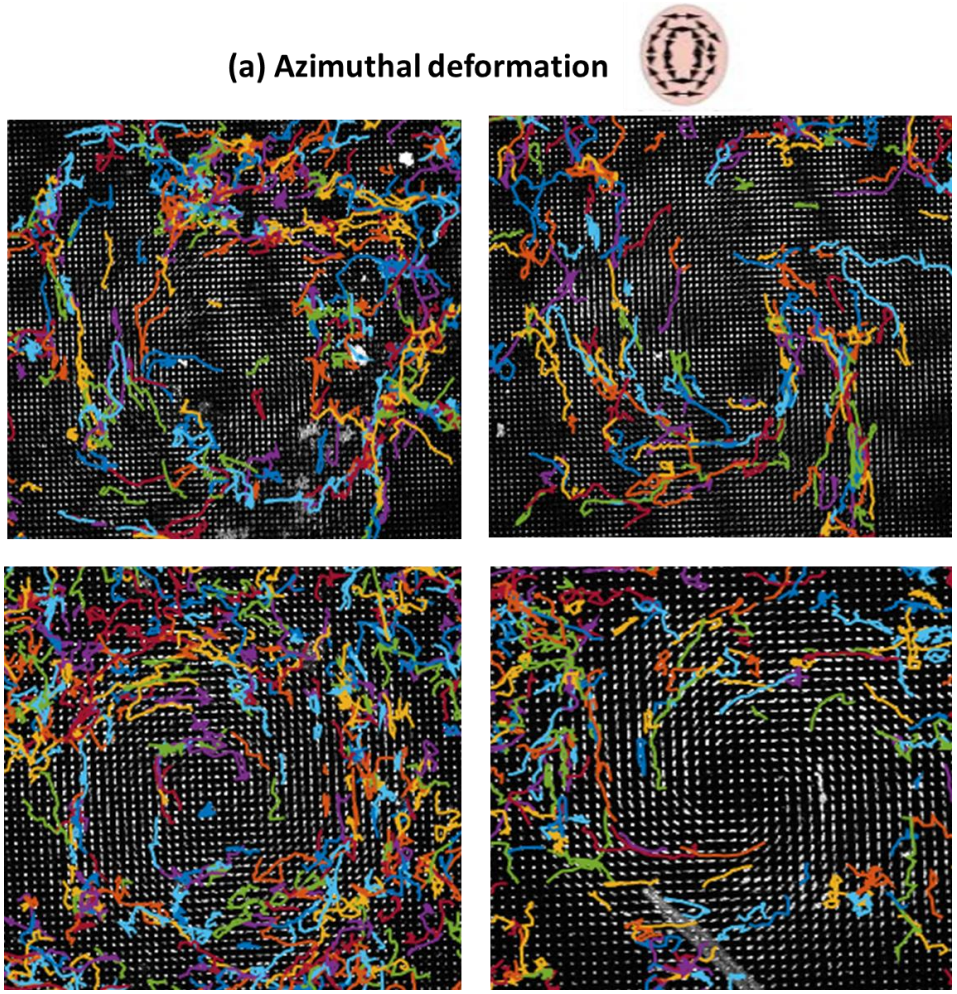

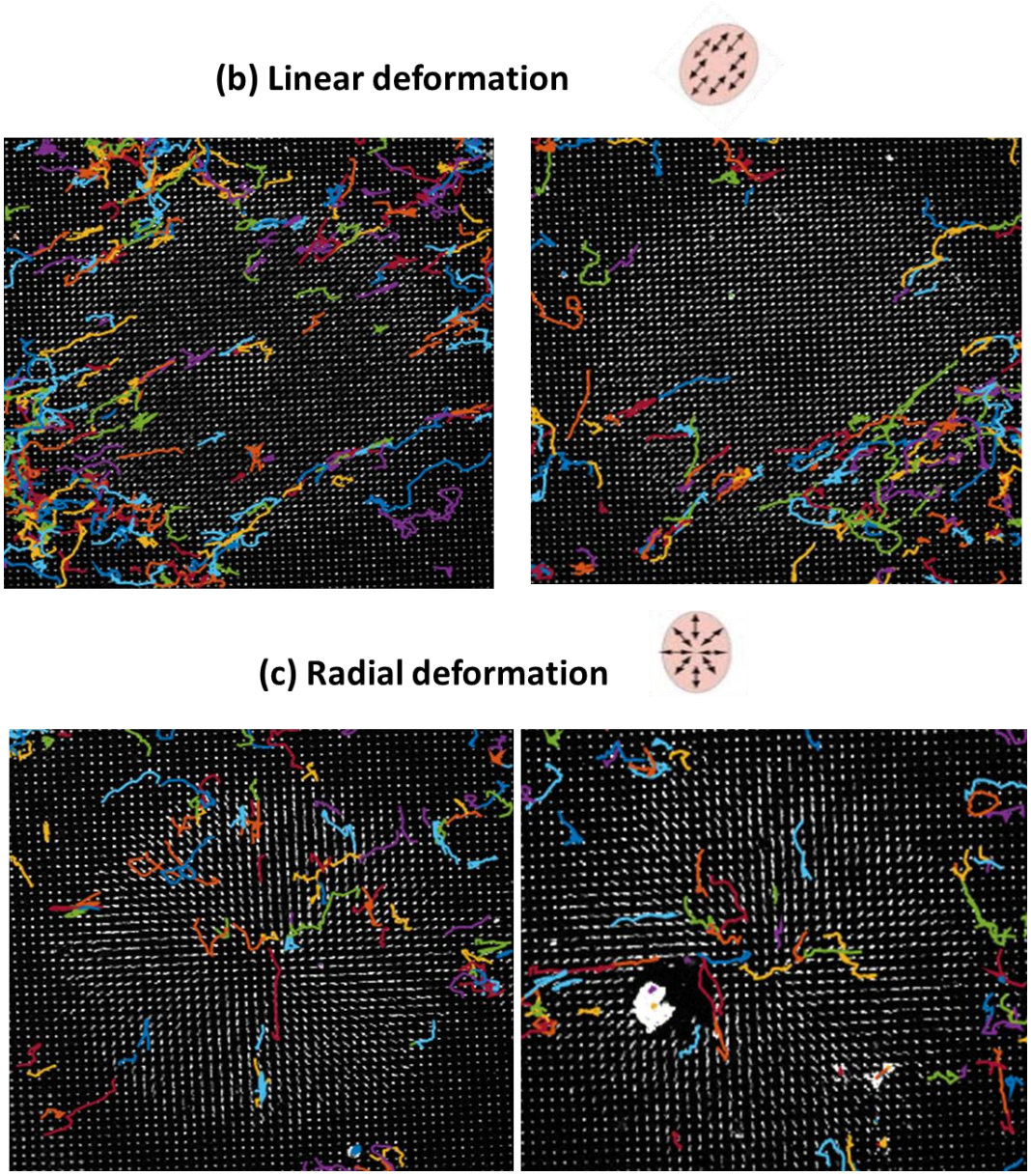

Figure 5.12: Cells displacements tracking of migration according different deforming pattern (a) azimuthal, (b) linear and (c) radial.

Figure 5.12 shows the overlay of the individual cells paths after the 20-hours-time lapse image acquisition. Each cells path is depicted with a different color to distinguish between two close cell paths. It is clearly visible that for both situations, the cell trajectories tend to follow the orientation of the deformation. So, it seems

that the distribution of the cell motion responds successfully to the modification of the surrounding environment. For example, the projection of the azimuthally polarized doughnut beam gave to the substrate the ability to drive efficaciously the living cells along a circular pathway on the sub-millimeter scale leaving the central not deformed area. The work is still in progress, the idea is to optimize the identification of the cells movements in a successful and automated way.

6

Conclusions and Outlook

The work presented in this thesis has dealt with smart responsive polymeric nano- and micro-structures. Micro and nanotechnologies essentially rely on the development of static tiny devices whose intrinsic properties are fixed by their fabrication processes. Modifying these properties dynamically after device fabrication remains an extraordinary challenge, and represents nowadays high scientific and economic perspectives. This is especially critical in optics, where both system miniaturization and dynamic control of light are of crucial importance in a large panel of applications, ranging from telecommunication to biology and security. The manipulation levers on light are usually relying on diffraction and refraction phenomena. They involve the refractive index and shape of a structured material as means to control the light intrinsic properties and trajectories. So far, the dynamic control of light has been reported via the dynamic tunability of the refractive index. The development of deformable materials under external control represents another appealing opportunity. Although it represents an important new degree of freedom in the manipulation of light, it stretches the actual limits of material science, and thus remains extraordinarily challenging. The present thesis contributes to this subject. It explores a connected set of topics related to the investigation of smart materials, i.e., materials capable of reversibly modifying their surface shape under external stimuli, such as temperature or light. It addresses the processing and patterning of thermo-responsive and light-responsive polymers, their integration in highly innovative ultra-compact architectures, the monitoring of their reconfigurable properties in real-time, and the achievement of new functionalities out of their tunable morphological and optical responses.

The first finding of the present work, is developed during a visiting period at Austrian Institute of Technology in Wien, within a collaboration with the Dostalek's Biosensor group. We propose a new method for *in situ* observation of highly swollen hydrogel nanostructures, applied for the investigation of unusual properties of arrays of thermos-responsive hydrogel nanopillars. These structures

are prepared from a photo-crosslinkable pNIPAAm-based polymer by nanoimprint lithography. Specifically, the swelling and collapsing of periodic arrays of imprinted pNIPAAm nanopillars are observed by a combination of diffraction measurements and optical waveguide spectroscopy in comparison to the AFM results. In situ AFM (under water) is capable to capture the topographic features of the nanopillars in direct contact with water only at temperatures above the LCST where the structures are collapsed and sufficiently rigid. However, measurement of the optical waveguide-enhanced diffraction allowed observation of swelling above as well as below LCST. With the aid of an appropriate model the key characteristics could be determined from the optical measurements and these results are found to be fully consistent with the AFM observations. Interestingly, the obtained results indicate that the swelling ratio of nanopillars (allowed to expand and contract in 3D) is similar to that of a tethered thin pNIPAAm hydrogel film (which swells and collapses predominantly in 1D). The temperature-induced collapsing of pNIPAAm leads to the preservation of the nanopillar structure during drying. Bending of these structures is observed when the temperature is raised above the LCST, which is explained by the attractive hydrophobic interaction with the underneath hydrogel surface. The structure can be reversibly erased by drying at temperatures below the LCST and recovered by swelling at temperature below LCST and drying at elevated temperatures above the LCST. Respect previous works [82] [188], the presented approach provides versatile platform for *in situ* observation of low refractive index contrast nanostructures from materials like highly swollen hydrogels. The investigated thermo-responsive material can find its applications in areas such as sensing (e.g., humidity sensor in food packaging with naked eye readout of diffraction) or security features, which will be subject to following research.

The main focus is set towards azobenzene-containing materials and their fascinating photoinduced phenomena. We prove once again the peculiar characteristics of azopolymers in terms of micro- and nanofabrications. A standard photoresist responds to the illuminating light by means of a photoconversion that reflects the incident light intensity pattern. Here, azo-based polymers instead respond to both the light intensity and the light polarization status. In particular, we demonstrated that the mixture of an azopolymer with a passive component such as PMMA can improve the mechanical characteristics of individual micro-objects suitable for deformation using light. As an exemplary micro-structure, we considered micrometer-sized pillars that can be reversibly elongated and rotated with a rather good degree of control, upon optimal choice of the radiation wavelength and polarization, as the elongation and restoration experiments confirm.

Moreover, to the best of our knowledge, as an extension of the state of the art [110], we demonstrate for the first time the possibility to restore the deformed shape in its initial configuration just by rotating the polarization direction of the incident laser beam. While micro-pillars have been chosen in order to allow a quick and statistically meaningful optical characterization, an analogous mechanical light-responsivity is expected to occur also in nano-sized objects. The same approach is successful applied to other structure like micro-pores. The findings, here presented are promising in useful applications such as tunable smart architectures including, e.g. photonic crystals and optical metamaterials and dynamically wettable surfaces, since we provide a responsive platform able to undergo *in situ* deformation and restoration of its pristine shape.

Thanks to this precise spatio-temporal control of the light-induced deformation of the azopolymeric microstructure, we have demonstrated the ability to alter its surface wettability. By exploiting the anisotropic topography obtained by making the pDR1M-pillars elongated according to the polarization direction of an illumination laser, we studied the correlated surface properties. In this work we managed to vary the contact angle of a water droplet on the structure by more than 30 degrees. This process can be partially reversed provided that the pillar elongation is kept within a roundness larger than about 0.5. However, other azopolymeric compounds can be used to improve reversibility of deformation. The ability to tune and recover the surface hydrophobicity along specific directions may open up future promising applications, including functional biomimetic surfaces and tunable smart material architectures for cell cultures, wherein azo-compounds can provide additional chemical functionalities.

We further showed that properly polarized light can induce birefringence in either a flat or structured polymeric film containing azo-polymers. The induced birefringence can be reversibly actuated by rotating the incident laser polarization and its slow decay time allows for creating transmissive patterns. The same effect can be observed on structured surfaces, where the transmittance of individual micro-pillars can be addressed. The fabrication of surface structures on large area where the optical response of individual elements can be addressed may find application in holographic applications as well as in actively driven dielectric metasurfaces.

Additionally, we were particularly interested to observe the optical response and potential applications provided by azobenzene molecules, doping diverse host materials with different properties. Such studies involved azo compounds

incorporated into either a soft elastomeric matrix and in a rigid photocurable commercial polymeric resin. In both experimental studies we obtained homogenous and transparent solution in which the azocompound is completely dissolved. So the first novel azopolymeric optical systems developed is a light-responsive elastomeric material, whose Optical Transfer Function (OTF) can be reversible engineered by a proper laser irradiation. Differently from most of the state-of-the-art tunable optical devices, wherein different optical functionalities are obtained by means of a pre-patterning or a pixelization of the device, a continuous light-controlled graded refractive index (GRIN) distribution can be induced here by a simple projection of a desired pattern, similarly to Optically Addressed Spatial Light Modulators. However, the resulting transmission function is phase-only, polarization insensitive and broadband, leading to a much wider range of opportunities for applications. The reversibility due to the elastomeric matrix allows a fast reshape of the refractive index distribution in a dynamic way. As illustrative examples, a lens-like transmission functions has been presented in this work as potential applications. GRIN elements are very useful for their ability to eliminate spherical aberrations typical of standard optics [189], and the flatness of their surface facilitates their integration in complex optical microsystems [190]. The results presented here pave the way to optically driven adaptive GRIN elements that can serve for a dynamic correction of focal length or aberrations in imaging systems, as well as in applications requiring dynamically adjustable wavefront engineering.

The second novel material developed consists in a DR1M azopolymer embedded a commercial photocurable acrylic resin. Besides its optical and responsive properties, the potential of this new responsive resin is that it can be used as resist in two photon polymerization lithography. DR1M absorbs very strongly in the spectral region 400- 550 nm and is completely transparent at 600-2100 nm and it has a window of transparency in the spectral region 300-400 nm. These properties make DR1M ideal for two photon polymerization using Ti:Sapphire laser femtosecond laser (780nm). The IR transparency allows focusing of the laser within the volume of the material, while the relatively high UV transparency means that there will be two-photon absorption mostly by the photoinitiator and not by the azo compound. The main findings obtained from this study is to successfully load photopolymerizable resin formulations with azo compounds and the consequent fabrication of light responsive 3D suspended micro sized membranes by means of two-photon lithography technique, aiming at giving new opportunities for optomechanical transduction. Various characterization,

including Raman and Interferometric measurements, are conducted in order to analyze and study the behavior under laser illumination of such membranes. The fabrication part is carried during a visiting period at King Abdullah University of Science and Technology in Saudi Arabia. The light-induced mechanical transduction is observed by means of an interferometric set up. We demonstrate that the membrane if irradiated, expand, and we also provide an estimation of this expansion of about 5μm. This expansion effect, is still under study, and many future applications are possible, for example in the biological field. An investigation on the biocompatibility of the novel material could be done, in order to fabricate 3D scaffold by two photon lithographic process for cell culture. In a properly customized optical microscope, the fabricated scaffolds could be light-triggered for tuning their morphology and/or mechanical properties with cells on board, in order to study the cell response and fate.

A preliminary study of the cell behavior, in terms of adhesion, migration, elongation and differentiation, in response to external signals, is carried out on pDR1M micro-pillars platform. By exploited the ability to deform the azopolymeric pattern with cell on board by light triggers, the main finding in this part, is the dynamic material-cell interaction in response to modification of surface topography; we have demonstrated that the cell tends to elongated according to the modification of the surrounding environments. Human breast cancer cells (MDA-MB-231) are successfully shown to adhere to the micro-patterned surfaces made from pDR1M and were seeded on a variety of the samples prepared from pDR1m. The cells are regularly passaged to maintain the cell line. Staining of the MDA-MB-231 cells seeded on a previously elongated micro-pillar structure are analyzed with a spinning disk confocal microscopy and highly oriented elongation of the cells in the pillar-elongation direction was observed. An optical holographic conditioning system, as a platform to study dynamic cell-material interactions in a two-dimensional (2D) environment is successfully implemented. The system consists of an optical setup with a home-made incubator and a control program capable of precise shaping of the laser beam and thus creating precise topographical patters (micrometers resolution) on the sample surface by a holographic projected pattern by means of a spatial light modulator. The designed system can perform time-lapse experiments to analyze the cell response to the dynamic topographical cues. Some experiments with a micro-pillar structure from pDR1M seeded with the MDA-MB-231 cell are carried out to test the functionality of the system. A successful spatially accurate topographical modification of the micro-structure performed with a shaped linearly polarized laser beam is performed, modifying

only an imminent surrounding of a selected cell attached to the sample surface. A time-lapse experiment is set to demonstrate the full functionality of the system. The experiment is considered successful, since demonstrating the functionality of highly innovative optical conditioning system and cells mentioned to be sensitive to the surrounding topological modification. The next step will be the implementation of a real-time tracking process in order to optimize the identification of the cells movements in a successful and automated way.

Overall, this thesis has presented new ways to investigated and to exploit the intrinsic light-induced effect of azobenzene- containing materials. One of the most key factors that limit the practical utilization of the laser-triggered mass movements is that the foundamental physical explanation is still under debate. Improving our understanding and knowledge on the directionality, photosoftening and restoring of azo-materials structures will increase the employment of this phenomenon in our modern civilization, towards a real use in existing or yet unknown application area.

References

[1] M. Geissler and Y. Xia, “Patterning: Principles and some new developments,” *Advanced Materials*, vol. 16, no. 15 SPEC. ISS. pp. 1249–1269, 2004.

[2] A. Biswas, I. S. Bayer, A. S. Biris, T. Wang, E. Dervishi, and F. Faupel, “Advances in top-down and bottom-up surface nanofabrication: Techniques, applications & future prospects,” *Adv. Colloid Interface Sci.*, vol. 170, no. 1–2, pp. 2–27, 2012.

[3] M. Kaholek, W. K. Lee, B. LaMattina, K. C. Caster, and S. Zauscher, “Fabrication of Stimulus-Responsive Nanopatterned Polymer Brushes by Scanning-Probe Lithography,” *Nano Lett.*, vol. 4, no. 2, pp. 373–376, 2004.

[4] D. J. Lipomi, R. C. Chiechi, M. D. Dickey, and G. M. Whitesides, “Fabrication of conjugated polymer nanowires by edge lithography,” *Nano Lett.*, vol. 8, no. 7, pp. 2100–2105, 2008.

[5] B. D. Gates, Q. Xu, M. Stewart, D. Ryan, C. G. Willson, and G. M. Whitesides, “New approaches to nanofabrication: Molding, printing, and other techniques,” *Chem. Rev.*, vol. 105, no. 4, pp. 1171–1196, 2005.

[6] H. Becker and U. Heim, “Hot embossing as a method for the fabrication of polymer high aspect ratio structures,” *Sensors Actuators, A Phys.*, vol. 83, no. 1, pp. 130–135, 2000.

[7] G. M. Whitesides, “Self-Assembly at All Scales,” *Science*, vol. 295, no. 5564, pp. 2418–2421, 2002.

[8] M.A.C. Stuart, W.T.S. Huck, J. Genzer, M. Müller, C. Ober, M. Stamm, G.B. Sukhorukov, I. Szleifer, V.V. Tsukruk, M. Urban, et al “Emerging applications of stimuli-responsive polymer materials.,” *Nat. Mater.*, vol. 9, no. 2, pp. 101–113, 2010.

[9] D. Roy, J. N. Cambre, and B. S. Sumerlin, "Future perspectives and recent advances in stimuli-responsive materials," *Prog. Polym. Sci.*, vol. 35, no. 1–2, pp. 278–301, 2010.

[10] S. Kamila, "Introduction, classification and applications of smart materials: An overview," *Am. J. Appl. Sci.*, vol. 10, no. 8, pp. 876–880, 2013.

[11] E. Cabane, X. Zhang, K. Langowska, C. G. Palivan, and W. Meier, "Stimuli-responsive polymers and their applications in nanomedicine," *Biointerphases*, vol. 7, no. 1–4, pp. 1–27, 2012.

[12] M. Hosseini and A. S. Hamdy Makhlouf, "Industrial applications for intelligent polymers and coatings," *Ind. Appl. Intell. Polym. Coatings*, pp. 1–710, 2016.

[13] F. D. Jochum and P. Theato, "Temperature- and light-responsive smart polymer materials," *Chem. Soc. Rev.*, vol. 42, no. 17, pp. 7468–7483, 2013.

[14] J. Zhang, M. Zhang, K. Tang, F. Verpoort, and T. Sun, "Polymer-based stimuli-responsive recyclable catalytic systems for organic synthesis," *Small*, vol. 10, no. 1, pp. 32–46, 2014.

[15] S. I. Yusa, S. Yamago, M. Sugahara, S. Morikawa, T. Yamamoto, and Y. Morishima, "Thermo-responsive diblock copolymers of poly(N-isopropylacrylamide) and poly(N-vinyl-2-pyrroridone) synthesized via organotellurium-mediated controlled radical polymerization (TERP)," *Macromolecules*, vol. 40, no. 16, pp. 5907–5915, 2007.

[16] M. A. Ward and T. K. Georgiou, "Thermoresponsive polymers for biomedical applications," *Polymers*, vol. 3, no. 3, pp. 1215–1242, 2011.

[17] L. D. Taylor and L. D. Cerankowski, "Preparation of Films Exhibiting a Balanced Solutions-A Study of Lower Consolute Behavior," *J. Polym. Sci.*, vol. 13, pp. 2551–2570, 1975.

[18] C. Boutris, E. G. Chatzi, and C. Kiparissides, "Characterization of the LCST behaviour of aqueous poly(N-isopropylacrylamide) solutions by thermal and cloud point techniques," *Polymer*, vol. 38, no. 10, pp. 2567–2570, 1997.

[19] N. T. Southall, K. A. Dill, and A. D. J. Haymet, "A view of the hydrophobic effect," *J. Phys. Chem. B*, vol. 106, no. 3, pp. 521–533, 2002.

[20] A. K. Tucker and M. J. Stevens, "Study of the Polymer Length Dependence of the Single Chain Transition Temperature in Syndiotactic Poly(N-isopropylacrylamide) Oligomers in Water," *Macromolecules*, vol. 45, no. 16, pp. 6697–6703, 2012.

[21] H. G. Schild, "Poly (N-Isopropylacrylamide): Experiment , Theory and Application," *Prog. Polym. Sci.*, vol. 17, pp. 163–249, 1992.

[22] M. C. Hacker, L. Klouda, B. B. Ma, J. D. Kretlow, and A. G. Mikos, "Synthesis and characterization of injectable, thermally and chemically gelable, amphiphilic poly(N-isopropylacrylamide)-based macromers," *Biomacromolecules*, vol. 9, no. 6, pp. 1558–1570, 2008.

[23] P. Kujawa, F. Segui, S. Shaban, C. Diab, Y. Okada, F. Tanaka, and F.M. Winnik, "Impact of end-group association and main-chain hydration on the thermosensitive properties of hydrophobically modified telechelic poly(N-isopropylacrylamides) in water," *Macromolecules*, vol. 39, no. 1, pp. 341–348, 2006.

[24] B. V. K. J. Schmidt, M. Hetzer, H. Ritter, and C. Barner-Kowollik, "Modulation of the thermoresponsive behavior of poly(N,N-diethylacrylamide) via cyclodextrin host/guest interactions," *Macromol. Rapid Commun.*, vol. 34, no. 16, pp. 1306–1311, 2013.

[25] H. Vihola, A. Laukkanen, L. Valtola, H. Tenhu, and J. Hirvonen, "Cytotoxicity of thermosensitive polymers poly(N-isopropylacrylamide), poly(N-vinylcaprolactam) and amphiphilically modified poly(N-vinylcaprolactam)," *Biomaterials*, vol. 26, no. 16, pp. 3055–3064, 2005.

[26] F. A. Plamper, M. Ruppel, A. Schmalz, O. Borisov, M. Ballauff, and A. H. E. Müller, "Tuning the Thermoresponsive Properties of Weak Polyelectrolytes: Aqueous Solutions of Star-Shaped and Linear Poly(N,N -dimethylaminoethyl Methacrylate)," *Macromolecules*, vol. 40, no. 23, pp. 8361–8366, 2007.

[27] R. Hoogenboom, H. M. L. Thijs, M. J. H. C. Jochems, B. M. van Lankvelt, M. W. M. Fijten, and U. S. Schubert, "Tuning the LCST of poly(2-oxazoline)s by varying composition and molecular weight: alternatives to poly(N-isopropylacrylamide)?," *Chem. Commun. (Camb).*, no. 44, pp. 5758–5760, 2008.

[28] G. Vancoillie, D. Frank, and R. Hoogenboom, "Thermoresponsive poly(oligo ethylene glycol acrylates)," *Prog. Polym. Sci.*, vol. 39, no. 6, pp. 1074–1095, 2014.

[29] F. Dai, P. Wang, Y. Wang, L. Tang, J. Yang, W. Liu, H. Li, and G. Wang, "Double thermoresponsive polybetaine-based ABA triblock copolymers with capability to condense DNA," *Polymer,* vol. 49, no. 24, pp. 5322–5328, 2008.

[30] X. Huang, F. Du, R. Ju, and Z. Li, "Novel acid-labile, thermoresponsive poly(methacrylamide)s with pendent ortho ester moieties," *Macromol. Rapid Commun.*, vol. 28, no. 5, pp. 597–603, 2007.

[31] N. Shimada, M. Nakayama, A. Kano, and A. Maruyama, "Design of UCST polymers for chilling capture of proteins," *Biomacromolecules*, vol. 14, no. 5, pp. 1452–1457, 2013.

[32] L. Chen, Y. Honma, T. Mizutani, D. J. Liaw, J. P. Gong, and Y. Osada, "Effects of polyelectrolyte complexation on the UCST of zwitterionic polymer," *Polymer,* vol. 41, no. 1, pp. 141–147, 2000.

[33] F. Liu and S. Agarwal, "Thermoresponsive gold nanoparticles with positive UCST-type thermoresponsivity," *Macromol. Chem. Phys.*, vol. 216, no. 4, pp. 460–465, 2015.

[34] F. A. Plamper, A. Schmalz, M. Ballauff, and A. H. E. Müller, "Tuning the thermoresponsiveness of weak polyelectrolytes by pH and light: Lower and upper critical-solution temperature of poly(N,N-dimethylaminoethyl methacrylate)," *J. Am. Chem. Soc.*, vol. 129, no. 47, pp. 14538–14539, 2007.

[35] B. Hammouda, D. L. Ho, and S. Kline, "Insight into Clustering in Poly (ethylene oxide) Solutions," *Macromolecules*, pp. 6932–6937, 2004.

[36] K. Van Durme, G. Van Assche, E. Nies, and B. Van Mele, "Phase transformations in aqueous low molar mass poly(vinyl methyl ether) solutions:

Theoretical prediction and experimental validation of the peculiar solvent melting line, bimodal LCST, and (adjacent) UCST miscibility gaps," *J. Phys. Chem. B*, vol. 111, no. 6, pp. 1288–1295, 2007.

[37] J.V.M. Weaver, I. Bannister, K.L. Robinson, X. Bories-Azeau, S.P. Armes, M. Smallridge, and P. McKenna, "Stimulus-Responsive Water-Soluble Polymers Based on 2-Hydroxyethyl Methacrylate," *Macromolecules*, vol. 37, no. 7, pp. 2395–2403, 2004.

[38] F. Ercole, T. P. Davis, and R. A. Evans, "Photo-responsive systems and biomaterials: photochromic polymers, light-triggered self-assembly, surface modification, fluorescence modulation and beyond," *Polym. Chem.*, vol. 1, no. 1, pp. 37–54, 2010.

[39] F. P. Nicoletta, D. Cupelli, P. Formoso, G. de Filpo, V. Colella, and A. Gugliuzza, "Light responsive polymer membranes: A review," *Membranes ,* vol. 2, no. 1, pp. 134–197, 2012.

[40] T. Kinoshita, "Biomembrane mimetic systems," *Prog. Polym. Sci.*, vol. 20, no. 3, pp. 527–583, 1995.

[41] A. Natansohn and P. Rochon, "Photoinduced motions in azo-containing polymers," *Chem. Rev.*, vol. 102, no. 11, pp. 4139–4175, 2002.

[42] E. M. Ahmed, "Hydrogel: Preparation, characterization, and applications: A review," *J. Adv. Res.*, vol. 6, no. 2, pp. 105–121, 2015.

[43] F. Ullah, M. B. H. Othman, F. Javed, Z. Ahmad, and H. M. Akil, "Classification, processing and application of hydrogels: A review," *Mater. Sci. Eng. C*, vol. 57, pp. 414–433, 2015.

[44] A. Sidorenko, T. Krupenkin, A. Taylor, P. Fratzl, and J. Aizenberg, "Reversible Switching of Hydrogel-Actuated Nanostructures into Complex Micropatterns," *Science.*, vol. 315, no. 5811, pp. 487–490, 2007.

[45] M. E. Harmon, D. Kuckling, P. Pareek, and C. W. Frank, "Photo-cross-linkable PNIPAAm copolymers. 4. Effects of copolymerization and cross-linking on the

volume-phase transition in constrained hydrogel layers," *Langmuir*, vol. 19, no. 26, pp. 10947–10956, 2003.

[46] H. J. van der Linden, S. Herber, W. Olthuis, and P. Bergveld, "Stimulus-sensitive hydrogels and their applications in chemical (micro)analysis," *Analyst*, vol. 128, no. 4, pp. 325–331, 2003.

[47] D. Kuckling, M. E. Harmon, C. W. Frank, D. Kuckling, M. E. Harmon, and C. W. Frank, "Photo-cross-linkable PNIPAAm copolymers. 1. Synthesis and characterization of constrained temperature-responsive hydrogel layers," *Macromolecules*, vol. 35, no. 16, pp 6377–6383, 2002.

[48] K. Y. Lee and D. J. Mooney, "Hydrogels for tissue engineering," *Chem. Rev.*, vol. 101, no. 7, pp. 1869–1879, 2001.

[49] Y. Qiu and K. Park, "Environment-sensitive hydrogels for drug delivery," *Adv. Drug Deliv. Rev.*, vol. 64, no. SUPPL., pp. 49–60, 2012.

[50] M. E. Harmon, M. Tang, and C. W. Frank, "A microfluidic actuator based on thermoresponsive hydrogels," *Polymer,* vol. 44, no. 16, pp. 4547–4556, 2003.

[51] C. Fenzl, S. Wilhelm, T. Hirsch, and O. S. Wolfbeis, "Optical sensing of the ionic strength using photonic crystals in a hydrogel matrix.," *ACS Appl. Mater. Interfaces*, vol. 5, no. 1, pp. 173–178, 2013.

[52] K. Schuh, O. Prucker, and J. Rühe, "Surface attached polymer networks through thermally induced cross-linking of sulfonyl azide group containing polymers," *Macromolecules*, vol. 41, no. 23, pp. 9284–9289, 2008.

[53] R. Toomey, D. Freidank, and J. Rühe, "Swelling Behavior of Thin, Surface-Attached Polymer Networks," *Macromolecules*, vol. 37, no. 3, pp. 882–887, 2004.

[54] A. Suzuki, X. R. Wu, M. Kuroda, E. Ishiyama, and D. Kanama, "Swelling properties of thin-plate hydrogels under mechanical constraint," *Japanese J. Appl. Physics, Part 1 Regul. Pap. Short Notes Rev. Pap.*, vol. 42, no. 2 A, pp. 564–569, 2003.

[55] M. E. Harmon, T. A. M. Jakob, W. Knoll, and C. W. Frank, "A Surface Plasmon Resonance Study of Volume Phase Transitions in N -Isopropylacrylamide Gel Films," *Macromolecules*, vol. 35, no. 15, pp. 5999–6004, 2002.

[56] D. Schmaljohann, M. Nitschke, R. Schulze, A. Eing, C. Werner, and K. J. Eichhorn, "In situ study of the thermoresponsive behavior of micropatterned hydrogel films by imaging ellipsometry," *Langmuir*, vol. 21, no. 6, pp. 2317–2322, 2005.

[57] E. Wijaya, C. Lenaerts, S. Maricot, J. Hastanin, S. Habraken, J.P. Vilcot, R. Boukherroub, and S. Szunerits,"Surface plasmon resonance-based biosensors: From the development of different SPR structures to novel surface functionalization strategies," *Curr. Opin. Solid State Mater. Sci.*, vol. 15, no. 5, pp. 208–224, 2011.

[58] A. Aulasevich, R. F. Roskamp, U. Jonas, B. Menges, J. Dostálek, and W. Knoll, "Optical waveguide spectroscopy for the investigation of protein-functionalized hydrogel films," *Macromol. Rapid Commun.*, vol. 30, no. 9–10, pp. 872–877, 2009.

[59] M. J. N. Junk, R. Berger, and U. Jonas, "Atomic force spectroscopy of thermoresponsive photo-cross-linked hydrogel films," *Langmuir*, vol. 26, no. 10, pp. 7262–7269, 2010.

[60] M. Zourob, S. Mohr, P. R. Fielden, and N. J. Goddard, "An integrated disposable dye clad leaky waveguide sensor for micro-TAS applications.," *Lab Chip*, vol. 5, no. 7, pp. 772–777, 2005.

[61] R. G. Heideman and P.V. Lambeck, "Chemical Remote opto-chemical sensing with extreme sensitivity: design , fabrication and performance of a pigtailed integrated optical phase- modulated Mach – Zehnder interferometer system," *Sensor and Actuactors B*, vol. 61, no. 1-3, pp. 100-127, 1999.

[62] Z. Nie and E. Kumacheva, "Patterning surfaces with functional polymers," *Nat. Mater.*, vol. 7, no. 4, pp. 277–290, 2008.

[63] Y. Ofir, I. W. Moran, C. Subramani, K. R. Carter, and V. M. Rotello, "Nanoimprint lithography for functional three-dimensional patterns," *Adv. Mater.*, vol. 22, no. 32, pp. 3608–3614, 2010.

[64] G. M. Burrowg and T. K. Gaylord, “Multi-beam interference advances and applications: Nano-electronics, photonic crystals, metamaterials, subwavelength structures, optical trapping, and biomedical structures,” *Micromachines*, vol. 2, no. 2, pp. 221–257, 2011.

[65] D. Xia, Z. Ku, S. C. Lee, and S. R. J. Brueck, “Nanostructures and functional materials fabricated by interferometric lithography,” *Adv. Mater.*, vol. 23, no. 2, pp. 147–179, 2011.

[66] F. Huo, G. Zheng, X. Liao, L.R. Giam, J. Chai, X. Chen, W. Shim, and C.A Mirkin , “Beam pen lithography,” *Nat. Nanotechnol.*, vol. 5, no. 9, pp. 637–640, 2010.

[67] D. Ho, J. Zou, B. Zdyrko, K. S. Iyer, and I. Luzinov, “Capillary force lithography: the versatility of this facile approach in developing nanoscale applications.,” *Nanoscale*, vol. 7, no. 2, pp. 401–14, 2014.

[68] F. Di Benedetto, A. Biasco, D. Pisignano, and R. Cingolani, “Patterning polyacrylamide hydrogels by soft lithography,” *Nanotechnology*, vol. 16, no. 5, pp. S165–S170, 2005.

[69] H. Lan and H. Liu, “UV-Nanoimprint Lithography: Structure, Materials and Fabrication of Flexible Molds,” *J. Nanosci. Nanotechnol.*, vol. 13, no. 5, pp. 3145–3172, 2013.

[70] W. Knoll, M. Zizlsperger, T. Liebermann, S. Arnold, A. Badia, M. Liley, D. Piscevic, F.J. Schmitt, and J. Spinke, “Streptavidin arrays as supramolecular architectures in surface-plasmon optical sensor formats,” *Colloids Surfaces A Physicochem. Eng. Asp.*, vol. 161, no. 1, pp. 115–137, 2000.

[71] T. J. Davis, “Surface plasmon modes in multi-layer thin-films,” *Opt. Commun.*, vol. 282, no. 1, pp. 135–140, 2009.

[72] J. Homola and M. Piliarik, *Surface plasmon resonance (SPR) sensors*. 2006.

[73] J. Homola, S. S. Yee, and G. Gauglitz, “Surface plasmon resonance sensors: review,” *Sensors Actuators B Chem.*, vol. 54, no. 1, pp. 3–15, 1999.

[74] M. Born and E. Wolf, “Principles of optics: Electromagnetic Theory of

Propagation, Interference and Diffraction of Light," *Pergamon Press*, pp. 1–952, 1994.

[75] M. G. Moharam and T. K. Gaylord, "Rigorous coupled-wave analysis of metallic surface-relief gratings," *J. Opt. Soc. Am. A*, vol. 3, no. 11, p. 1780, 1986.

[76] A. N. Grigorenko, P. I. Nikitin, and A. V. Kabashin, "Phase jumps and interferometric surface plasmon resonance imaging," *Appl. Phys. Lett.*, vol. 75, no. 25, pp. 3917–3919, 1999.

[77] J. Homola, J. Ctyroky, M. Skalky, J. Hradiliva, and P. Kolarova, "A surface plasmon resonance based integrated optical sensor," *Sensors Actuators B Chem.*, vol. 38–39, pp. 286–290, 1997.

[78] E. Kretschmann and H. Raether, "Radiative Decay of Non Radiative Surface Plasmons Excited by Light," *Zeitschrift fur Naturforsch. - Sect. A J. Phys. Sci.*, vol. 23, no. 12, pp. 2135–2136, 1968.

[79] K. Kurihara and K. Suzuki, "Theoretical Understanding of an Absorption-Based Surface Plasmon Resonance Sensor Based on Kretchmann ' s Theory," *Anal. Chem.*, vol. 74, no. 3, pp. 696–701, 2002.

[80] S. Ekgasit, C. Thammacharoen, and W. Knoll, "Surface Plasmon Resonance Spectroscopy Based on Evanescent Field Treatment," *Anal. Chem.*, vol. 76, no. 3, pp. 561–568, 2004.

[81] A. Shalabney and I. Abdulhalim, "Electromagnetic fields distribution in multilayer thin film structures and the origin of sensitivity enhancement in surface plasmon resonance sensors," *Sensors Actuators, A Phys.*, vol. 159, no. 1, pp. 24–32, 2010.

[82] M. Toma, U. Jonas, A. Mateescu, W. Knoll, and J. Dostalek, "Active control of SPR by thermoresponsive hydrogels for biosensor applications," *J. Phys. Chem. C*, vol. 117, no. 22, pp. 11705–11712, 2013.

[83] P. W. Beines, I. Klosterkamp, B. Menges, U. Jonas, and W. Knoll, "Responsive thin hydrogel layers from photo-cross-linkable poly(N-isopropylacrylamide) terpolymers," *Langmuir*, vol. 23, no. 4, pp. 2231–2238, 2007.

[84] F. Pirani, N. Sharma, A. Moreno-Cencerrado, S. Fossati, C. Petri, E. Descrovi, J.L. Toca-Herrera, U. Jonas, and J. Dostalek, "Optical Waveguide-Enhanced Diffraction for Observation of Responsive Hydrogel Nanostructures," *Macromol. Chem. Phys.*, vol. 218, no. 6, pp. 1–10, 2017.

[85] A. Mourran, Y. Wu, R.A. Gumerov, A.A. Rudov, I.I. Potemkin, A. Pich, M. Möller., "When Colloidal Particles Become Polymer Coils," *Langmuir*, vol. 32, no. 3, pp. 723–730, 2016.

[86] M. M. Braun and L. Pilon, "Effective optical properties of non-absorbing nanoporous thin films," *Thin Solid Films*, vol. 496, no. 2, pp. 505–514, 2006.

[87] G. M. Hale and M. R. Querry, "Optical Constants of Water in the 200-nm to 200-microm Wavelength Region.," *Appl. Opt.*, vol. 12, no. 3, pp. 555–563, 1973.

[88] M. Guvendiren, S. Yang, and J. A. Burdick, "Swelling-Induced surface patterns in hydrogels with gradient crosslinking density," *Adv. Funct. Mater.*, vol. 19, no. 19, pp. 3038–3045, 2009.

[89] J. A. Delaire and K. Nakatani, "Linear and Nonlinear Optical Properties of Photochromic Molecules and Materials," *Chem. Rev.*, vol. 100, no. 5, pp. 1817–1846, 2000.

[90] M. M. Russew and S. Hecht, "Photoswitches: From molecules to materials," *Adv. Mater.*, vol. 22, no. 31, pp. 3348–3360, 2010.

[91] C. J. Barrett, J. Mamiya, K. G. Yager, and T. Ikeda, "Photo-mechanical effects in azobenzene-containing soft materials," *Soft Matter*, vol. 3, no. 10, p. 1249, 2007.

[92] C. Barrett, A. Natansohn, and P. Rochon, "Cis-Trans Thermal Isomerization Rates of Bound and Doped Azobenzenes in a Series of Polymers," *Chem. Mater.*, vol. 7, no. 5, pp. 899–903, 1995.

[93] G. S. Kumar and D. C. Neckers, "Photochemistry of Azobenzene-Containing Polymers," *Chem. Rev.*, vol. 89, no. 8, pp. 1915–1925, 1989.

[94] G. S. Kumar and D. C. Neckers, "Photochemistry of azobenzene-containing polymers," *Chem. Rev.*, vol. 89, no. 8, pp. 1915–1925, 1989.

[95] S. Monti, G. Orlandi, and P. Palmieri, “Features of the photochemically active state surfaces of azobenzene,” *Chem. Phys.*, vol. 71, no. 1, pp. 87–99, 1982.

[96] T. Naito, K. Horie, and I. Mita, “Photochemistry in Polymer Solids. 11. The Effects of the Size of Reaction Groups and the Mode of Photoisomerization on Photochromic Reactions in Polycarbonate Film,” *Macromolecules*, vol. 24, no. 10, pp. 2907–2911, 1991.

[97] G. C. Hampson and J. M. Robertson, “Bond Lengths and Resonance in the cis-Azobenzene Molecule,” *J. Chem. Soc.*, pp. 409–413, 1941.

[98] H. M. D. Bandara and S. C. Burdette, “Photoisomerization in different classes of azobenzene,” *Chem. Soc. Rev.*, vol. 41, no. 5, pp. 1809–1825, 2012.

[99] Z. Mahimwalla, K. G. Yager, J. Mamiya, A. Shishido, A. Priimagi, and C. J. Barrett, “Azobenzene photomechanics: prospects and potential applications”, *Polymer Bulletin,* vol. 69, no. 8, pp.967-1006, 2012.

[100] E. Fischer, M. Frankel, and R. Wolovsky, “Wavelength Dependence of Photoisomerization Equilibria in Azocompounds,” *J. Chem. Phys.*, vol. 23, no. 7, pp. 1367–1367, 1955.

[101] A. Priimagi and A. Shevchenko, “Azopolymer-based micro- and nanopatterning for photonic applications,” *J. Polym. Sci. Part B Polym. Phys.*, vol. 52, no. 3, pp. 163–182, 2014.

[102] N.K. Viswanathan, D.Y. Kim, S. Bian, J. Williams, W. Liu, L. Li, L. Samuelson, J. Kumar, and S.K Tripathy, “Surface relief structures on azo polymer films,” *J. Mater. Chem.*, vol. 9, no. 9, pp. 1941–1955, 1999.

[103] M. Dumont and A. El Osman, “On spontaneous and photoinduced orientational mobility of dye molecules in polymers,” *Chem. Phys.*, vol. 245, no. 1–3, pp. 437–462, 1999.

[104] Z. Sekkat, D. Yasumatsu, and S. Kawata, “Pure photoorientation of azo dye in polyurethanes and quantification of orientation of spectrally overlapping isomers,” *J. Phys. Chem. B*, vol. 106, no. 48, pp. 12407–12417, 2002.

[105] M.-S. Ho, A. Natansohn, C. Barrett, and P. Rochon, “Azo polymers for reversible optical storage. 8. The effect of polarity of the azobenzene groups,” *Can. J. Chem.*, vol. 73, no. 11, pp. 1773–1778, 1995.

[106] Y. Yu and T. Ikeda, “Alignment modulation of azobenzene-containing liquid crystal systems by photochemical reactions,” *J. Photochem. Photobiol. C Photochem. Rev.*, vol. 5, no. 3, pp. 247–265, 2004.

[107] P. Rochon, E. Batalla, and A. Natansohn, “Optically induced surface gratings on azoaromatic polymer films,” *Appl. Phys. Lett.*, vol. 66, no. 2, pp. 136–138, 1995.

[108] D. Y. Kim, S. K. Tripathy, L. Li, and J. Kumar, “Laser-induced holographic surface relief gratings on nonlinear optical polymer films,” *Appl. Phys. Lett.*, vol. 66, no. 10, pp. 1166–1168, 1995.

[109] J.E. Koskela, J. Vapaavuori, J.Hautala, A. Priimagi, C.F.J. Faul, M. Kaivola, and R.H.A. Ras, “Surface-relief gratings and stable birefringence inscribed using light of broad spectral range in supramolecular polymer-bisazobenzene complexes,” *J. Phys. Chem. C*, vol. 116, no. 3, pp. 2363–2370, 2012.

[110] S. Lee, H. S. Kang, and J. K. Park, “Directional photofluidization lithography: Micro/nanostructural evolution by photofluidic motions of azobenzene materials,” *Adv. Mater.*, vol. 24, no. 16, pp. 2069–2103, 2012.

[111] K. G. Yager and C. J. Barrett, “Temperature modeling of laser-irradiated azo-polymer thin films,” *J. Chem. Phys.*, vol. 120, no. 2, pp. 1089–1096, 2004.

[112] C. J. Barrett, A. L. Natansohn, and P. L. Rochon, “Mechanism of Optically Inscribed High-Efficiency Diffraction Gratings in Azo Polymer Films,” *J. Phys. Chem.*, vol. 100, no. 21, pp. 8836–8842, 1996.

[113] T. G. Pedersen, P. M. Johansen, N. C. R. Holme, P. S. Ramanujam, and S. Hvilsted, “Mean-Field Theory of Photoinduced Formation of Surface Reliefs in Side-Chain Azobenzene Polymers,” *Phys. Rev. Lett.*, vol. 80, no. 1, pp. 89–92, 1998.

[114] J. Kumar, L. Li, X. L. Jiang, D. Y. Kim, T. S. Lee, and S. Tripathy, "Gradient force: The mechanism for surface relief grating formation in azobenzene functionalized polymers," *Appl. Phys. Lett.*, vol. 72, no. 17, pp. 2096–2098, 1998.

[115] F. Lagugne´ Labarthet, J.-L. Bruneel, T. Buffeteau, C. Sourisseau, M.R. Huber, S.J. Zilker and T. Bieringer, "Photoinduced orientations of azobenzene chromophores in two distinct holographic diffraction gratings as studied by polarized Raman confocal microspectrometry," *Phys. Chem. Chem. Phys.*, vol. 2, no. 22, pp. 5154–5167, 2000.

[116] Y. Zhang, J.-H. Han, L. Zhu, M. a Shannon, and J. Yeom, "Soft lithographic printing and transfer of photosensitive polymers: facile fabrication of free-standing structures and patterning fragile and unconventional substrates," *J. Micromechanics Microengineering*, vol. 24, no. 11, p. 115019, 2014.

[117] F. Frascella, A. Angelini, S. Ricciardi, E. Descrovi and C.F. Pirri, "Surface-relief formation in azo-polyelectrolyte layers with a protective polymer coating," *Optical Materials Express,* vol. 6, no. 2, pp. 444–450, 2016.

[118] S. Lee, H. S. Kang, A. Ambrosio, J. Park, and L. Marrucci, "Directional Superficial Photofluidization for Deterministic Shaping of Complex 3D Architectures," *ACS Appl. Mater. Interfaces*, vol. 7, pp. 8209−8217 2015.

[119] F. Pirani, A. Angelini, F. Frascella, R. Rizzo, S. Ricciardi, and E. Descrovi, "Light-Driven Reversible Shaping of Individual Azopolymeric Micro-Pillars," *Sci. Rep.*, vol. 6, no. August, p. 31702, 2016.

[120] H. S. Kang, S. Lee, and J. K. Park, "Monolithic, hierarchical surface reliefs by holographic photofluidization of azopolymer arrays: Direct visualization of polymeric flows," *Adv. Funct. Mater.*, vol. 21, no. 23, pp. 4412–4422, 2011.

[121] X. Zhou, Y. Du, and X. Wang, "Azo Polymer Janus Particles and Their Photoinduced, Symmetry-Breaking Deformation," *ACS Macro Lett.*, vol. 5, no. 2, pp. 234–237, 2016.

[122] F. Pirani, A. Angelini, F. Frascella, and E. Descrovi, "Reversible Shaping of Microwells by Polarized Light Irradiation," *International Journal of Polymer*, vol. 2017, pp. 1–6, 2017.

[123] B. Xin and J. Hao, "Reversibly switchable wettability.," *Chem. Soc. Rev.*, vol. 39, no. 2, pp. 769–782, 2010.

[124] K. Ichimura, S.-K. Oh, and M. Nakagawa, "Light-Driven Motion of Liquids on a Photoresponsive Surface," *Science,* vol. 288, no. 5471, pp. 1624–1626, 2000.

[125] C. Radüge, G. Papastavrou, D. G. Kurth, and H. Motschmann, "Controlling wettability by light: Illuminating the molecular mechanism," *Eur. Phys. J. E*, vol. 10, no. 2, pp. 103–114, 2003.

[126] C.L. Feng, Y.J. Zhang, J. Jin, Y.L. Song, L.Y. Xie, G.R. Qu, L. Jiang, and D.B. Zhu, "Reversible wettability of photoresponsive fluorine-containing azobenzene polymer in langmuir-blodgett films," *Langmuir*, vol. 17, no. 15, pp. 4593–4597, 2001.

[127] N. Delorme, J.-F. Bardeau, A. Bulou, and F. Poncin-Epaillard, "Azobenzene-Containing Monolayer with Photoswitchable Wettability," *Langmuir*, vol. 21, no. 26, pp. 12278–12282, Dec. 2005.

[128] F. Pirani, A. Angelini, S. Ricciardi, F. Frascella, and E. Descrovi, "Laser-induced anisotropic wettability on azopolymeric micro-structures," *Appl. Phys. Lett.*, vol. 110, no. 10, 2017.

[129] J. T. Yang, Z. H. Yang, C. Y. Chen, and D. J. Yao, "Conversion of surface energy and manipulation of a single droplet across micropatterned surfaces," *Langmuir*, vol. 24, no. 17, pp. 9889–9897, 2008.

[130] T. Todorov, L. Nikolova, and N. Tomova, "Polarization holography. 1: A new high-efficiency organic material with reversible photoinduced birefringence.," *Appl. Opt.*, vol. 23, no. 23, pp. 4309–4312, 1984.

[131] L. Nikolova and T. Todorov, "Diffraction efficiency and selectivity of polarization holographic recording," *Opt. Acta (Lond).*, vol. 31, no. 5, pp. 579–588, 1984.

[132] P. Rochon, J. Gosselin, A. Natansohn, and S. Xie, "Optically induced and erased birefringence and dichroism in azoaromatic polymers," *Appl. Phys. Lett.*, vol. 60, no. 1, pp. 4–5, 1992.

[133] A. Natansohn, P. Rochon, J. Gosselin, and S. Xie, “Azo polymers for reversible optical storage. 1. Poly[4’-[[2-(acryloyloxy)ethyl]ethylamino]-4-nitroazobenzene],” *Macromolecules*, vol. 25, no. 8, pp. 2268–2273, 1992.

[134] K. Ichimura, “Photoalignment of Liquid-Crystal Systems,” *Chem. Rev.*, vol. 100, no. 5, pp. 1847–1874, 2000.

[135] T. Ikeda and O. Tsutsumi, “Optical Switching and Image Storage by Means of Azobenzene Liquid-Crystal Films,” *Science,* vol. 268, no. 5219, pp. 1873–1875, 1995.

[136] S. Wu, J. Shen, J. Huang, Y. Wu, Z. Zhang, Y. Hu, W. Wu, W. Huang, K. Wang, and Q. Zhang,“Ag nanoparticle/azopolymer nanocomposites: In situ synthesis, microstructure, rewritable optically induced birefringence and optical recording,” *Polymer*, vol. 51, no. 6, pp. 1395–1403, 2010.

[137] J. Cognard and T. H. Phan, “The Use of Azo Dyes in Guest-Host Displays,” *Mol. Cryst. Liq. Cryst.*, vol. 68, no. 1, pp. 207–229, 1981.

[138] K. D. Singer, M. G. Kuzyk, and J. E. Sohn, “Second-order nonlinear-optical processes in orientationally ordered materials: relationship between molecular and macroscopic properties,” *J. Opt. Soc. Am. B*, vol. 4, no. 6, p. 968, 1987.

[139] D. M. Burland, R. D. Miller, and C. A. Walsh, “Second-Order Nonlinearity in Poled-Polymer Systems,” *Chem. Rev.*, vol. 94, no. 1, pp. 31–75, 1994.

[140] A. Natansohn, P. Rochon, C. Barrett, and A. Hay, “Stability of Photoinduced Orientation of an Azo Compound into a High-Tg Polymer,” *Chem. Mater.*, vol. 7, no. 9, pp. 1612–1615, 1995.

[141] P. Carlberg, L. Montelius, and J. Tegenfeldt, “Nanoimprint in PDMS on glass with two-level hybrid stamp,” *Microelectronic Engineering*, vol. 85, no. 1 pp. 210–213, 2008.

[142] S. K. Sia and G. M. Whitesides, “Review Microfluidic devices fabricated in poly (dimethylsiloxane) for biological studies,” *Electrophoresis,* pp. 3563–3576, 2003.

[143] O. Buchnev, N. Podoliak, M. Kaczmarek, N.I. Zheludev, and V.A. Fedotov, "Electrically Controlled Nanostructured Metasurface Loaded with Liquid Crystal: Toward Multifunctional Photonic Switch" *Advanced Optical Materials,* vol. 3, no. 5, p. 2015, 2015.

[144] J. Kim, J. Kim, J.-H. Na, B. Lee, and S.-D. Lee, "Liquid crystal-based square lens array with tunable focal length," *Opt. Express*, vol. 22, no. 3, p. 3316, 2014.

[145] J.W. Park, P. Van Tuong, J.Y. Rhee, K.W. Kim, W.H. Jang, E.H. Choi, L.Y. Chen, and Y. Lee,"Multi-band metamaterial absorber based on the arrangement of donut-type resonators.," *Opt. Express*, vol. 21, no. 8, pp. 9691–702, 2013.

[146] D. Graham-Rowe, "Liquid lenses make a splash," *Nat. Photonics*, vol. sample, no. September, pp. 2–4, 2006.

[147] L. Dong, A. K. Agarwal, D. J. Beebe, and H. Jiang, "Variable-focus liquid microlenses and microlens arrays actuated by thermoresponsive hydrogels," *Adv. Mater.*, vol. 19, no. 3, pp. 401–405, 2007.

[148] D. C. Ghiglia and L. A. Romero, "Robust two-dimensional weighted and unweighted phase unwrapping that uses fast transforms and iterative methods," *J. Opt. Soc. Am. A*, vol. 11, no. 1, p. 107, 1994.

[149] O. M. Tanchak and C. J. Barrett, "Light-induced reversible volume changes in thin films of azo polymers: The photomechanical effect," *Macromolecules*, vol. 38, no. 25, pp. 10566–10570, 2005.

[150] B. Richerzhagen, "Interferometer for measuring the absolute refractive index of liquid water as a function of temperature at 1.064 μm.," *Appl. Opt.*, vol. 35, no. 10, pp. 1650–1653, 1996.

[151] L. Ionov, "Polymeric actuators," *Langmuir*, vol. 31, no. 18, pp. 5015–5024, 2015.

[152] H. Ko and A. Javey, "Smart Actuators and Adhesives for Reconfigurable Matter," *Acc. Chem. Res.*, vol. 50, no. 4, pp. 691–702, 2017.

[153] H. Zeng, P. Wasylczyk, C. Parmeggiani, D. Martella, M. Burresi, and D. S. Wiersma, "Light-Fueled Microscopic Walkers," *Adv. Mater.*, vol. 27, no. 26, pp. 3883–3887, 2015.

[154] T. Seki, "Mono- and multilayers of photoreactive polymers as collective and active supramolecular systems," *Supramol. Sci.*, vol. 3, no. 96, pp. 25–29, 1996.

[155] T. Ikeda, M. Nakano, Y. Yu, O. Tsutsumi, and A. Kanazawa, "Anisotropic bending and unbending behavior of azobenzene liquid-crystalline gels by light exposure," *Adv. Mater.*, vol. 15, no. 3, pp. 201–204, 2003.

[156] H. Zeng, D. Martella, P. Wasylczyk, G. Cerretti, J.C.G. Lavocat, C.H. Ho, C. Parmeggiani, and D.S. Wiersma, "High-resolution 3d direct laser writing for liquid-crystalline elastomer microstructures," *Adv. Mater.*, vol. 26, no. 15, pp. 2319–2322, 2014.

[157] S. Palagi, A.G. Mark, S.Y. Reigh, K. Melde, T. Qiu, H. Zeng, C. Parmeggiani, D. Martella, A. Sanchez-Castillo, N. Kapernaum, F. Giesselmann, D.S Wiersma, E. Lauga, and P. Fischer,"Structured light enables biomimetic swimming and versatile locomotion of photoresponsive soft microrobots," *Nat. Mater.*, vol. 15, no. 6, pp. 647–653, 2016.

[158] H. Zeng, P. Wasylczyk, C. Parmeggiani, D. Martella, and D. S. Wiersma, "Free-form Light Actuators - Fabrication and Control of Actuation in Microscopic Scale.," *J. Vis. Exp.*, no. 111, pp. 1–8, 2016.

[159] I. Roppolo, A. Chiappone, A. Angelini, S. Stassi, F. Frascella, C.F.Pirri, C. Ricciardi, and E. Descrovi, "3D printable light-responsive polymers," *Mater. Horiz.*, vol. 4, no. 3, pp. 396–401, 2017.

[160] S. Wu, Q. Zhang, and C. Bubeck, "Solvent effects on structure, morphology, and photophysical properties of an Azo chromophore-functionalized polydiacetylene," *Macromolecules*, vol. 43, no. 14, pp. 6142–6151, 2010.

[161] X. Yao, R. Peng, and J. Ding, "Cell-material interactions revealed via material techniques of surface patterning," *Adv. Mater.*, vol. 25, no. 37, pp. 5257–5286, 2013.

[162] R. M. Duffy, Y. Sun, and A. W. Feinberg, "Understanding the Role of ECM Protein Composition and Geometric Micropatterning for Engineering Human Skeletal Muscle," *Ann. Biomed. Eng.*, vol. 44, no. 6, pp. 2076–2089, 2016.

[163] A. M. Pizzo, "Extracellular matrix (ECM) microstructural composition regulates local cell-ECM biomechanics and fundamental fibroblast behavior: a multidimensional perspective," *J. Appl. Physiol.*, vol. 98, no. 5, pp. 1909–1921, 2005.

[164] Y. Kuboki, Q. Jin, M. Kikuchi, J. Mamood, and H. Takita, "Geometry of Artificial ECM: Sizes of Pores Controlling Phenotype Expression in BMP-Induced Osteogenesis and Chondrogenesis," *Connect. Tissue Res.*, vol. 43, no. 2–3, pp. 529–534, 2002.

[165] L. Cassereau, Y. A. Miroshnikova, G. Ou, J. Lakins, and V. M. Weaver, "A 3D tension bioreactor platform to study the interplay between ECM stiffness and tumor phenotype," *J. Biotechnol.*, vol. 193, pp. 66–69, 2015.

[166] S.C.B. Herath, D. Yue,S. Hui, M.C. Kim, D.A. Wang, Q. Wang, K.J. Van Vliet, H. Asada, and P.C.Y. Chen, "Quantification of magnetically induced changes in ECM local apparent stiffness," *Biophys. J.*, vol. 106, no. 1, pp. 332–341, 2014.

[167] C. J. Bettinger, R. Langer, and J. T. Borenstein, "Engineering substrate topography at the Micro- and nanoscale to control cell function," *Angew. Chemie - Int. Ed.*, vol. 48, no. 30, pp. 5406–5415, 2009.

[168] M. J. P. Biggs, R. G. Richards, and M. J. Dalby, "Nanotopographical modification: A regulator of cellular function through focal adhesions," *Nanomedicine Nanotechnology, Biol. Med.*, vol. 6, no. 5, pp. 619–633, 2010.

[169] J. Kim and R. C. Hayward, "Mimicking dynamic in vivo environments with stimuli-responsive materials for cell culture," *Trends Biotechnol.*, vol. 30, no. 8, pp. 426–439, 2012.

[170] C.Rianna, L. Rossano, R.H. Kollarigowda, F. Formiggini, S. Cavalli, M. Ventre, and P.A. Netti, "Spatio-Temporal Control of Dynamic Topographic Patterns on Azopolymers for Cell Culture Applications," *Adv. Funct. Mater.*, vol. 26, no. 42, pp. 7572–7580, 2016.

[171] M. Wu, J. Fannin, K. M. Rice, B. Wang, and E. R. Blough, "Effect of aging on cellular mechanotransduction," *Ageing Res. Rev.*, vol. 10, no. 1, pp. 1–15, 2011.

[172] P. M. Mendes, "Stimuli-responsive surfaces for bio-applications," *Chem. Soc. Rev.*, vol. 37, no. 11, p. 2512, 2008.

[173] E. K. F. Yim, E. M. Darling, K. Kulangara, F. Guilak, and K. W. Leong, "Nanotopography-induced changes in focal adhesions, cytoskeletal organization, and mechanical properties of human mesenchymal stem cells," *Biomaterials*, vol. 31, no. 6, pp. 1299–1306, 2010.

[174] M. Ventre, F. Valle, M. Bianchi, F. Biscarini, and P. A. Netti, "Cell fluidics: Producing cellular streams on micropatterned synthetic surfaces," *Langmuir*, vol. 28, no. 1, pp. 714–721, 2012.

[175] M. Ventre, F. Causa, and P. A. Netti, "Determinants of cell-material crosstalk at the interface: towards engineering of cell instructive materials," *J. R. Soc. Interface*, vol. 9, no. 74, pp. 2017–2032, 2012.

[176] T. Yeung, P.C. Georges, L.A. Flanagan, B. Marg, M. Ortiz, M. Funaki, N. Zahir, W. Ming, V. Weaver, and P.A. Janmey, "Effects of substrate stiffness on cell morphology, cytoskeletal structure, and adhesion," *Cell Motil. Cytoskeleton*, vol. 60, no. 1, pp. 24–34, 2005.

[177] C. S. Chen, "Geometric Control of Cell Life and Death," *Science,* vol. 276, no. 5317, pp. 1425–1428, 1997.

[178] M. Nikkhah, F. Edalat, S. Manoucheri, and A. Khademhosseini, "Engineering microscale topographies to control the cell-substrate interface," *Biomaterials*, vol. 33, no. 21, pp. 5230–5246, 2012.

[179] H. J. Jeon, C. G. Simon, and G. H. Kim, "A mini-review: Cell response to microscale, nanoscale, and hierarchical patterning of surface structure," *J. Biomed. Mater. Res. - Part B Appl. Biomater.*, vol. 102, no. 7, pp. 1580–1594, 2014.

[180] C. D. W. Wilkinson, M. Riehle, M. Wood, J. Gallagher, and A. S. G. Curtis, "The use of materials patterned on a nano- and micro-metric scale in cellular

engineering", *Materials Science and Engineering: C*, vol. 19, no. 1-2, pp. 263–269, 2002.

[181] S. H. Chung and J. Min, "Morphological investigations of cells that adhered to the irregular patterned polydimethylsiloxane (PDMS) surface without reagents," *Ultramicroscopy*, vol. 109, no. 8, pp. 861–867, 2009.

[182] H. Jeon, H. Hidai, D. J. Hwang, K. E. Healy, and C. P. Grigoropoulos, "The effect of micronscale anisotropic cross patterns on fibroblast migration," *Biomaterials*, vol. 31, no. 15, pp. 4286–4295, 2010.

[183] T. Steinberg, S. Schulz, J.P. Spatz, N. Grabe, E. Mussig, A. Kohl, G. Komposch, and P. Tomakidi, "Early keratinocyte differentiation on micropillar interfaces," *Nano Lett.*, vol. 7, no. 2, pp. 287–294, 2007.

[184] J. W. Haycock, "3D Cell Culture", *Humana Press, Totowa, N*, vol. 695, pp. 1–15, 2011.

[185] D. L. Holliday and V. Speirs, "Choosing the right cell line for breast cancer research.," *Breast Cancer Res.*, vol. 13, p. 215, 2011.

[186] R. Cailleau, R. Young, M. Olivé, and W. J. J. Reeves, "Breast Tumor Cell Lines From Pleural Effusions," *Jounal Natl. Cancer Inst.*, vol. 53, no. 3, pp. 661–674, 1974.

[187] Invitrogen, "Cell Culture Basics Handbook," *ThermoFisher Sci. Inc.*, pp. 1–61, 2010.

[188] A. Mateescu, Y. Wang, J. Dostalek, and U. Jonas, "Thin hydrogel films for optical biosensor applications," *Membranes*, vol. 2, no. 1, pp. 49–69, 2012.

[189] D. T. Moore, "Gradient-index optics: a review," *Appl. Opt.*, vol. 19, no. 7, pp. 1035–1038, 1980.

[190] M. Zickar, W. Noell, C. Marxer, and N. de Rooij, "MEMS compatible micro-GRIN lenses for fiber to chip coupling of light," *Opt. Express*, vol. 14, no. 10, p. 4237, 2006.